République Algérienne Démocratique et Populaire
Ministère de l'Enseignement Supérieur et de la Recherche Scientifique
Université Ibn Khaldoun de Tiaret
Faculté des Sciences Appliquées
Département de Génie Mécanique

MÉMOIRE DE FIN D'ETUDES

Pour l'obtention du Diplôme de Master

Domaine : Sciences et Technologie
Filière : Génie Mécanique
Parcours : Master
Spécialité : Énergétique

Thème

THE DIRECT NUMERICAL SIMULATION (DNS) AND LARGE EDDY SIMULATION (LES) OF FULLY DEVELOPED TURBULENT PIPE FLOW AND HEAT TRANSFER OF DILATANT FLUID THROUGH A HEATED AXIALLY ROTATING PIPE

Préparé par :

BELADJINE Nour Elhouda
AIT YAHIA Manel

Soutenu publiquement le :11 / 06 / 2023, devant le jury composé de :

M. AKERMI Nasreddine	Maître de Conférences "B" (Univ. Ibn Khaldoun)	Président
M. SAD CHEMLOUL Nordeddine	Professeur (Univ. Ibn Khaldoun)	Examinateur
M. ABED Belkacem	Maître de Conférences "A" (Univ. Ibn Khaldoun)	Examinateur
M. ABDI Mohamed	Docteur (Univ. Ibn Khaldoun)	Encadrant
M. CHAIB Khaled	Maître de Conférences "A" (Univ. Ibn Khaldoun)	Co-Encadrant

Année universitaire : 2022 - 2023


بسم الله الرحمن الرحيم

DEDICATION

We dedicate this work to ALLAH Almighty, my creator, strong pillar, and source of inspiration, wisdom, knowledge and understanding. He has been the source of my strength throughout my life.

All that has been achieved in this work, the effort, perseverance, perfection, hard work, and all that are positive about it, of course, thanks to ALLAH and thanks to my Dear Parents. So, I dedicate all this work to them, and I say thanks for listening, support, encouraging words, understanding, opinions, and everything you gave me in my journey to accomplish this best thesis.

Every step I took and succeeded in was one of my mother's prayers ; every right decision I took was one of my father's tips, my parent's strength in this life. I pray to ALLAH for health and for a lifetime, and everything great in this work is gifted to you.

My sisters my support in the world, my strength in my weakness, my happiness in my grief. I say thank you for your understanding, for listening to me and for accepting me in all my cases. All my accomplishments are dedicated to you.

Furthermore, I dedicate, to my sister's children, my joy in life, cut out of me. I pray ALLAH to save you and all the best to achieve your success.

My mate on this trail, thank you for understanding, your patience, support, and helping me at all times. Without you, it wasn't that precise and perfect.

My team, my second family, thanks for everything I have experienced with you, for your support for every kind word of you, this work is, of course, a gift to you. Pray to Allah for all preservation and success.

Nour Elhouda BELADJINE

First and foremost, all thanks and praises be to ALLAH Almighty, my creator, strong pillar, and source of inspiration. He has given me strength and encouragement throughout all the challenging moments of completing this thesis. I am truly grateful for His unconditional mercy and grace and also to his blessing.

This thesis is gifted to my Dear Parents. Thank you for your unwavering love, constant support, encouragement and prayers from the first day of my life, especially throughout my academic journey. Words can hardly describe my thanks and appreciation to you. You have inspired and motivated me during the most challenging times. Thank you for always believing in me and giving me what is necessary to achieve what I am today. I'm proud to be your daughter and truly thankful and honoured to have you as my parents. Mom and Dad, thank you very much for everything ; you are my real happiness ! May ALLAH protect you, and may success always be within my reach so that I can fill you with joy.

I also dedicate this thesis with much love to my exceptional and extraordinary sister, Hayet BOUDALIA I am very lucky to have you in my life. Thank you for your love, motivation and encouragement throughout these years. May ALLAH protect you, and may joy and success accompany you all your life.

I offer exceptional thanks to my extraordinary sister and colleague, Nour Elhouda BELADJINE for your patience, support and understanding and for always being with me.

I also offer this work to the best colleagues Lalia Abir BOUHENNI, Fatima Zohra BOUHENNI, Amina OULD MOHAMED and Belhouari BEKHTAOUI for their support, encouragement, motivation and the best moments that we spent together during all these years. May ALLAH protect you and may success accompany you.

I offer this thesis to my best team, my second family, you are my joy, my hapiness and my golden gift from ALLAH, thank you for the wonderful moments that we spent together, thank you for everything. May ALLAH protect all "ALBERT TEAM members" and may success accompany you.

Manel AIT YAHIA

ACKNOWLEDGMENTS

At the end of this work, I thank ALLAH, who gave us the strength and courage to elaborate on this thesis.

We would like to express my deepest gratitude to our advisor, Mr. Mohamed ABDI, whose sincerity and encouragement we will never forget. This thesis would not have been possible without our co-supervisor Mr. Khaled CHAIB, whose guidance from the initial research step enabled us to understand the subject. We are thankful for the extraordinary experiences he arranged for us and for providing opportunities to grow professionally ; it is an honour to learn from Mr. Slimane BENFARHET.

It isn't easy to overstate our appreciation of Mrs. Meryem OULD-ROUISS, Professor at the University GUSTAVE Eiffel in Champs sur Marne-77454- (France). This work would never have been possible without her priceless advice, motivation, and support throughout this project.

Our sincere thanks go out to Mr. Paolo ORLANDI, Professor at the Dipartimento di Ingegneria Meccanica e Aerospaziale, Università La Sapienza, Rome, Italy.

We want to express our sincere thanks to all the jury members for accepting and evaluating this work.

We want to express our sincere thanks to all the teachers of the departement of Mechanical Engineering.

Thanks to all the Laboratory "Modélisation et de Simulation à Multi-Echelles (MSME)" members for their help and for sharing their skills. We also thank all the members of the Laboratory "Laboratoire de génie électrique et des plasmas (LGEP) University of Tiaret, Algeria".

We are highly grateful to our colleagues at "THE ALBERT TEAM" for all the beautiful trips and fond memories. Thank you for your encouragement in all the moments. Your friendship makes our life

just a wonderful experience. They are the spice that made my journey less humdrum. Without their support, my progress would have been much slower.

Last but most importantly, we thank our parents today for their blessings, providing us with unfailing support and continuous encouragement throughout our years of study and through the research process and writing this thesis. There are not enough words to express how grateful we are to them for everything they have done for us. We thank our beloved families for their unceasing, unwavering love and encouragement. They have been instrumental in moulding us into who we are today. It is to them that we dedicate our thesis.

ملخص

تهدف هذه الدراسة إلى تسليط المزيد من الضوء على ظاهرة تصفيح الموائع (Ostwald de waele) من خلال تقييم قوة الطرد المركزي الناجم عن الدوامة التي ينشئها دوران جدار الأسطوانة على السلوك الريولوجي و خصائص التدفق و إنتقال الحرارة و الإحصاءات المضطربة . يهدف هذا البحث أيضا إلى التأكد من دقة و موثوقية المحاكاة الحسابية المباشرة (DNS) و محاكاة الدوامة الكبيرة (LES) للتنبؤ بالسلوك الريولوجي و نمط التدفق للموائع الشبه بلاستيكية و الممددة.
تم إجراء المحاكاة الحسابية المباشرة (DNS) لدراسة التدفق المضطرب للموائع الشبه بلاستيكية $(n = 0.75)$ و الممددة $(n = 1.2)$ عبر أسطوانة في حالة دوران حيث تم فرض عدد Reynolds في المحاكاة يساوي 5000 على مجال دوران (N) يتراوح بين $[0; 3]$. تم أيضا إجراء محاكاة الدوامة الكبيرة (LES) باستعمال النموذج الممدد لـ *Smagorinsky* لدراسة التدفق المضطرب للموائع الشبه بلاستيكية و الممددة عبر أسطوانة في حالة دوران؛ حيث تم فرض تدفق حراري ثابت و موحد على الجدار الخارجي للأسطوانة كشرط حد حراري. تم فرض أن أعداد Reynolds و Prandlt في المحاكاة هي 4500 و 1 توالیا على مجال دوران (N) يتراوح بين $[0; 3]$. تشير نتائج محاكاة الدوامة الكبيرة (LES) إلى أن قوة الطرد المركزي الناجم عن الدوامة التي ينشئها دوران جدار الأسطوانة يؤدي إلى انخفاض واضح في معدل القص كما أنه يؤدي إلى ارتفاع واضح للسرعة المحورية في المنطقة الأساسية. يزداد ظهور هذه القوة الطرد المركزي كلما زاد معدل دوران الأسطوانة.
تشير النتائج المتوقعة للمحاكاة الحسابية المباشرة (DNS) إلى إرتفاع معدل دوران الأسطوانة و ارتفاع آلية توليد و نقل الإضطرابات للسرعة المحورية. أظهرت نتائج (DNS) و (LES) أنه كلما زاد معدل دوران الأسطوانة تحسنت آلية التدفق الحراري العرضي.

الكلمات الرئيسية : المحاكاة الحسابية المباشرة (DNS) ، محاكاة الدوامة الكبيرة (LES) ، قوة الطرد المركزي .

ABSTRACT

The present study seeks to shed further light on the laminarisation phenomena of the Ostwald de Waele fluids by critically examining the effects of the centrifugal force induced by the swirl driven by the rotating pipe wall on the rheological behaviour, mean flow and thermal quantities, and turbulence statistics. The present investigation also aims to ascertain the accuracy and reliability of the laboratory code results and to evaluate the reliability of the DNS and LES approach to predict the rheological behaviour and flow pattern of pseudoplastic and dilatant fluids.

A direct numerical simulation (DNS) approach has been carried out in the first study investigation to study numerically a fully developed turbulent of the pseudoplastic $(n = 0.75)$ and the dilatant $(n = 1.2)$ fluids through an isothermal axially rotating pipe at simulation Reynolds number of 5000 and over a rotation rate range of $(0 \leq N \leq 3)$. The numeric resolution is chosen to be $(129 \times 129 \times 193)$ gridpoints in axial, radial and circumferential directions, with a domain length of $20R$ in the streamwise direction.

A large eddy simulation (LES) approach with an extended Smagorinsky model has been carried out in the second study investigation of a fully developed turbulent flow forced convection of thermally independent pseudoplastic and dilatant fluids through a heated axially rotating pipe, with a uniform heat flux (q_w) imposed on the pipe wall as a thermal boundary condition. This investigation is conducted over a rotation rate range of $(0 \leq N \leq 3)$ at a simulation Reynolds number (Re_s) of 4500 and a simulation Prandtl number (Pr_s) of 1, with a grid resolution of 65^3 gridpoints in axial, radial and circumferential directions, respectively, along a domain length of $20R$ in the axial direction.

LES results suggest that the centrifugal force induced by the swirl driven by the rotating pipe wall causes a pronounced decrease in the shear rate profile of the pseudoplastic and dilatant fluids along the pipe radius and increases the axial velocity profile in the core region. This trend

is more pronounced as the rotation rate increases, where these notes align with those of *DNS* results.

The predicted results of the *DNS* approach indicate that the increased rotation rate results in a noticeable enhancement in the generation and transport mechanism of turbulence intensities of the axial velocity fluctuation from the wall vicinity towards the core region. This increased rotation rate also enhances the transport mechanism of turbulence intensities of the radial velocity fluctuation from the axial velocity fluctuation.

The *LES* results also suggest that the swirl driven by the rotating pipe wall results in an apparent attenuation in the generation and transport mechanism of turbulence intensities of the axial velocity fluctuation from the wall vicinity towards the core region, resulting in a pronounced attenuation in the turbulent kinetic energy further away from the pipe wall with the wall distance.

The predicted results of the *DNS* and *LES* approaches suggest that the increased rotation rate induces a pronounced enhancement in the transport mechanism of turbulence intensities of the radial velocity fluctuation from the axial velocity fluctuation resulting in the radial heat flux for dilatant fluid.

Keywords : Direct Numerical Simulation, Large Eddy Simulation, extended Smagorinsky, fully developed, centrifugal forces, pseudoplastic, dilatant, forced convection.

RESUME

La présente étude vise à mieux comprendre le phénomène de laminarisation des fluides d'Ostwald de Waele en examinant de manière critique les effets de la force centrifuge induite par le tourbillon entraîné par la paroi rotative du cylindre chauffé sur le comportement rhéologique, les quantités moyennes de l'écoulement et les quantités thermiques, ainsi que sur les statistiques turbulentes. La présente étude vise également à vérifier la précision et la fiabilité des résultats du code maison et à évaluer la fiabilité des approches DNS et LES pour prédire le comportement rhéologique et le modèle d'écoulement du fluide rhéofluidifiant et rhéoépaississant.

Une simulation numérique directe (DNS) a été mise en œuvre dans la première étude afin d'étudier numériquement l'écoulement turbulent pleinement développé du fluide rhéofluidifiant $(n = 0.75)$ et rhéoépaississant $(n = 1.2)$ à travers un cylindre en rotation axiale. Le nombre de Reynolds de la simulation a été supposé être 5000 sur une plage de taux de rotation $(0 \leq N \leq 3)$. La résolution numérique a été choisie pour être de $(129 \times 129 \times 193)$ points de grille dans les directions axiale, radiale et circonférentielle.

Une simulation des grandes échelles (LES) avec un modèle de Smagorinsky étendu a été réalisée dans la deuxième étude d'un écoulement turbulent pleinement développé d'une convection forcée du fluide rhéofluidifiant $(n = 0.75)$ et rhéoépaississant $(n = 1.25)$ thermiquement indépendants à travers un cylindre chauffé en rotation axiale avec un flux de chaleur uniforme (q_w) a été imposé sur la paroi comme condition limite thermique. Cette étude est menée sur une plage de taux de rotation $(0 \leq N \leq 3)$ à un nombre de Reynolds de simulation (Re_s) de 4500 et un nombre de Prandtl de simulation (Pr_s) de 1. Les calculs ont été basés sur un schéma de différences finies, avec une résolution numérique de 65^3 points de grille dans les directions axiale, radiale et circonférentielle, respectivement.

Les résultats de LES suggèrent que la force centrifuge induite par le tourbillon entraîné par la

paroi rotative du cylindre provoque une diminution prononcée du profil du taux de cisaillement du fluide rhéofluidifiant et rhéoépaississant le long du rayon du cylindre et augmente le profil de la vitesse axiale dans la région centrale.

Les résultats prédits de la DNS indiquent que l'augmentation du taux de rotation entraîne une amélioration notable du mécanisme de génération et de transport des intensités de turbulence de la fluctuation de la vitesse axiale plus loin de la paroi du cylindre vers la région centrale. Cette augmentation du taux de rotation renforce également le mécanisme de transport des intensités de turbulence de la fluctuation de la vitesse radiale à partir de la fluctuation de la vitesse axiale.

Les résultats LES suggèrent également que le tourbillon entraîné par la paroi rotative du cylindre entraîne une diminution apparente du mécanisme de génération et de transport des intensités de turbulence de la fluctuation de la vitesse axiale de la proximité de la paroi vers la région centrale, ce qui entraîne une diminution prononcée de l'énergie cinétique turbulente plus loin de la paroi du cylindre vers la région centrale.

Les résultats prédits par les approches DNS et LES suggèrent que l'augmentation du taux de rotation induit une amélioration prononcée du mécanisme de transport des intensités de turbulence de la fluctuation de la vitesse radiale à partir de la fluctuation de la vitesse axiale, ce qui entraîne un flux de chaleur radial pour le fluide rhéoépaississant.

Mots clés :Simulation Numérique Directe, Simulation Des Grandes Echelles, Smagorinsky étendu, pleinement développé, forces centrifuge, rhéofluidifiant, rhéoépaississant, convection forcée.

CONTENTS

FIGURES LIST

TABLES LIST

NOMENCLATURE

SYMBOLS

a	Yasuda Constant	
C_d	Dynamic model coefficient	
C_s	Smagorinsky constant	
C_p	Specific heat	$\left[J.\ kg^{-1}.K^{-1}\right]$
D	Pipe diameter	$[m]$
$F(U_i^{'})$	Flatness coefficient $F\left(U_i^{'}\right) = \left\langle U_i^{'4}\right\rangle / \left\langle U_i^{'2}\right\rangle^{2}$	
h	Heat transfer coefficient	$[W/m^2.K\ ]$
G	Elasticity modulus	
K	Consistence	$[Pa.s^n]$
k	Turbulent kinetic energy	$[j]$
L	Domain length	$[m]$
N	Rotation rate $N = \Omega R/U_b$	
n	Flow behaviour index	
R	Pipe radius	$[m]$
r, θ, z	Radial, circumferential and axial directions	
$S\left(U_i^{'}\right)$	Skewness coefficient $S\left(U_i^{'}\right) = \left\langle U_i^{'3}\right\rangle / \left\langle U_i^{'2}\right\rangle^{3/2}$	
S_{ij}	Strain tensor $S_{ij} = \frac{1}{2}\left(\frac{du_i}{\partial x_j} + \frac{du_j}{\partial x_i}\right)$	
t	Time	$[s]$

T	Fluid temperature	$[K]$
T_{ref}	Reference temperature $T_\tau = \phi_p / \rho C_p U_b$	
T_τ	Friction temperature $T_\tau = \phi_p / \rho C_p U_\tau$	
T_{ij}	Sub-grid tensor of the second filter	
U_b	Mean axial velocity	$[m.s^{-1}]$
U, V, W	Axial, radial and circumferential velocity	$[m.s^{-1}]$
U^+	Mean axial velocity in wall units	
U_τ	Friction coefficient $(\tau_W / \rho\ )^{1/2}$	
U_i	Generic notation for the dimensionless velocity components	
U_{CL}	Axial velocity at the centre of the laminar analytical solution $U_{CL} = (3n+1)\, U_b / n+1$	

GREEK SYMBOLS

α	Molecular diffusivity $\alpha = k / \rho C_P$	$[m^2.s^{-1}]$
α_t	Turbulent diffusivity	$[m^2.s^{-1}]$
Δ	First filter size $\Delta = [r \Delta r \Delta\theta \Delta z]^{1/3}$	
$\tilde{\Delta}$	Second filter size $\Delta = [r \Delta r\, (2\Delta\theta)\, (2\Delta z)]^{1/3}$	
$\Delta\theta$	Size of the sub-grid in the circumferential direction	
Δr	Size of the sub-grid in the radial direction	
Δz	Size of the sub-grid in the axial direction	
ϕ_W	Flux density imposed on the wall	$[W.m^{-2}]$
$\dot{\gamma}$	Shear rate $\dot{\gamma} = (2 S_{ij} S_{ij})^{1/2}$	
$\dot{\gamma}_{d.W}$	Dimensionless shear rate at the wall $\dot{\gamma}_{d.W} = \dot{\gamma}_W R / U_{CL}$	
η	Apparent viscosity of the fluid $\eta = K \dot{\gamma}^{n-1}$	
η_W	Apparent viscosity of the fluid at the wall	
$\eta_{d.W}$	Apparent viscosity of Dimensionless fluid $\eta_{d.W} = \eta_W / \rho U_{CL} R$	
η_c	Casson viscosity	$\left[kg\ m^{-1}\ s^{-1}\right]$
λ	Characteristic viscous relaxation time	$[s]$
μ_∞	Infinite shear rate viscosity	$\left[kg\ m^{-1}\ s^{-1}\right]$

μ_0	Zero shear viscosity	$\left[kg\ m^{-1}\ s^{-1}\right]$
ν_t	Turbulent viscosity	$\left[kg\ m^{-1}\ s^{-1}\right]$
Θ	Dimensionless temperature $\Theta = (T_w - T(\theta, r, z, t))/T_{ref}$	
Ω	Rotational velocity	$[s^{-1}]$
ρ	Density	$[Kg.m^{-3}]$
τ_W	Wall shear stress $\tau_W = (D/4\ )\,\partial p/\partial z$	$[Pa]$
τ_0	Yield stress	$[Pa]$
τ_{ij}	Sub-grid tensor for the first filter	

DIMENSIONLESS NUMBERS

Re_{MR}	Metzner and Reed Reynolds number $Re_{MR} = 8\rho {U_b}^{2-n}/K\,(6 + 2/n\ )^{\ n}$
Re_s	Simulation Reynolds number $Re_s = \rho {U_{CL}}^{2-n} R^n/K$
Re_g	Generalised Reynolds number $Re_g = \rho U_b D/\eta_W$
Re_{cr}	Critical Reynolds number $Re_{cr} = 2100\left((4n+2)\,(5n+3)/3(3n+1)^2\ \right)$
f	Friction factor $f = 2\tau_W/\left(\rho {U_b}^2\right)$
Pr_s	Simulation Prandtl number $\mathrm{Pr}_s = K/\alpha\rho R^{n-1} {U_{CL}}^{1-n}$
Pr	Prandtl number $\mathrm{Pr} = \mu C_p/k = \nu/\alpha$
Pr_{MR}	Metzner and Reed Prandtl number $\mathrm{Pr}_{MR} = K((3n + 1/4n\ )\,(8U_b/D\ ))^{n-1} C_p/k$
Pr_t	Turbulent Prandtl number $\mathrm{Pr}_t = \nu_t/\alpha_t$
St	Stanton number $St = h/U_b\rho C_p$
Y^+	Wall distance $Y^+ = yU_\tau/\nu$
Nu	Nusselt number $Nu = hD/k$
Pe	Peclet number $Pe = DU_b/\alpha = Re\,\mathrm{Pr}$
Pe_s	Simulation Peclet number $Pe_s = U_{cL}R/\alpha$
Pe_{MR}	Metzner and Reed Peclet number $Pe_{MR} = Re_{MR}\mathrm{Pr}_{MR} = U_{CL}R/\alpha$
P_n	Pearson number $P_n = bT_{ref}$

EXHIBITORS

$\langle(.)\rangle$ Mean statistic

$(.)'$ Fluctuation

$(.)^+$ Normalised by U_τ,T_τ

$\overline{(.)}$ Filtered

INDICES

r, θ, z Radial, circumferential and axial directions

C Centre

L Laminar

W, P Wall

d Dimensionless

g Generalised

cr Critical

ABREVIATIONS

DNS Direct Numerical Simulation

LES Large Eddy Simulation

SGS Sub-grid scale

RMS Root mean square

CFL Current Friedrichs and Lewy state

GENERAL INTRODUCTION

GENERAL INTRODUCTION

Industrial Problematic

Much more often in nature, many fluids exhibit complex non-Newtonian behaviour and show a non-uniform viscosity. Practically, in industry, non-Newtonian fluids play a very significant role ; a wide variety of them are used in numerous applications such as the production of cement, food, paper and paint, as well as in the petroleum, pharmaceutical, and polymer molten, plastics even in mechanical and engineering fields (heat exchangers, combustion chambers, nuclear reactors, and turbomachines).

Over the past few decades, a considerable amount of research has been interested in the turbulent forced convection of non-Newtonian fluids through axial pipes due to the vital practical interest in the various industrial fields of these fluids, such as paper making, petroleum drilling, refining, combustion chambers, food processing, pharmaceutical and polymer processing industries.

Recently, the trend of applying the scale resolving simulation (DNS and LES) has been focused on the turbulent flows of non-Newtonian fluids in the absence of the experimental data of non-Newtonian ones. DNS and LES simulations have become very useful and powerful tools in computational techniques. Applying the two approaches to study non-Newtonian fluid turbulent flows focuses on describing the rheological, hydrodynamic, and thermal behaviour.

Purpose

The current investigation aims to shed further light on the laminarisation phenomenon of the Ostwald de Waele fluids by examining the effects of the centrifugal force induced by the swirl driven by the rotating pipe wall on rheological, hydrodynamic and thermal quantities, turbulence statistics (RMS).

Scientific Problematic

The first part of the current study concerns direct numerical simulation (DNS) of a fully developed turbulent flow of pseudoplastic $(n = 0.75)$ and dilatant $(n = 1.2)$ fluids through a rotating cylindrical pipe over a rotation rate range of $(0 \leq N \leq 3)$ at simulation Reynolds numbers of 5000. The computations procedures were performed using the finite difference scheme, second-order accurate in space and time with a numerical resolution of $(129 \times 129 \times 193)$ gridpoints in axial, radial and circumferential directions, respectively, with a domain length of $20R$ in the streamwise direction.

The second part of the present study focuses on the numerical investigation of a fully developed turbulent flow forced convection of non-thermo-dependent pseudoplastic $(n = 0.75)$ and dilatant $(n = 1.25)$ fluids through a heated axially rotating cylindrical pipe using the large eddy simulation (LES) approach with an extended Smagorinsky model. The simulation Reynolds number (Re_s) and the simulation Prandtl number (Pr_s) of this investigation are assumed to be 4500 and 1, respectively, at various rotation rates $(0 \leq N \leq 3)$. The computations procedures are based on a finite difference scheme, second-order accurate in space and time, with a numeric resolution of 65^3 gridpoints in axial, radial and circumferential directions, respectively, with a domain length of $20R$ in the axial direction. Uniform heat flux (q_w) is imposed on the wall as a thermal boundary condition.

Thesis Structure

The present thesis is structured in five chapters and is organised as follows :

CHAPTER 1 presents the classification of the fluids based on the different rheological models and the constitutive equations of each type of fluid.

CHAPTER 2 presents the literature of the previous research focused on experimental and numerical investigations, direct numerical simulation (DNS), and large eddy simulation (LES) of the fully developed turbulent flow of Newtonian and non-Newtonian fluids through an axially stationary or rotating pipe.

CHAPTER 3 sheds further light on the turbulence phenomena, characteristics of turbulence, and turbulence structure in addition to the well-known Kolmogorov theory. Moreover, section 2 presents the two extremely powerful numerical approaches (DNS) and (LES) and the sub-grid models of LES. Section 3 provides the LES approach's sub-grid scales (SGS). The spatial and temporal resolution requirements, the boundary and initial conditions, in addition to the rheological properties of the non-Newtonian fluids.

CHAPTER 4 focuses on the numerical investigation of a fully developed turbulent flow of pseudoplastic $(n = 0.75)$ and dilatant $(n = 1.2)$ fluids through an isothermal axially rotating pipe using the DNS approach.

CHAPTER 5 presents the flow governing equations and the mathematical formulations of the forced convection problem. This chapter devotes the LES of the forced convection turbulent flow of the thermally independent pseudoplastic $(n = 0.75)$ and dilatant $(n = 1.25)$ fluids through a uniform heated axially rotating pipe over a rotation rate range of $(0 \leq N \leq 3)$.

Finally, the Conclusions are drawn from the findings of the research work and recommendations for future work are made.

CHAPTER I

RHEOLOGICAL BEHAVIOUR

RHEOLOGICAL BEHAVIOUR I

What is Rheology ?

Rheology was first seen as a science in its own right not before the beginning of the 20th century. However, scientists and practical users have long been interested in the behaviour of liquids and solids, although some of their methods have not always been very scientific. Rheology is the science of deformation and flow. It is a branch of physics and physical chemistry since the most important variables come from the field of mechanics : forces, deflections and velocities [1]. The term rheology was invented in 1920 by Professor Eugene Bingham at Lafayette College in Indiana USA. A colleague, Martin Reiner, a professor in Classical Languages and History, inspired him. Bingham, a professor of Chemistry, studied new materials with strange flow behaviour, mainly paints [2]. The term "rheology" originates from the Greek "rhein", meaning "to flow". Thus, rheology is literally "flow science". However, rheological experiments reveal information about liquids' flow behaviour and solids' deformation behaviour. The connection here is that a large deformation produced by shear forces causes many materials to flow [1].

I.1 Continuum hypothesis

The matter may take three aggregate forms or phases : solid, liquid, and gaseous. A body of solid matter has a definite volume and form, dependent on the temperature and the forces the body is subjected to. A body of liquid matter, called a liquid, has a definite volume but not a definite form. A liquid in a container is formed by the container but does not necessarily fill it. A body of gaseous matter, gas, fills any container it is poured into.

- In the liquid phase, the molecular forces are too weak to bind the molecules to definite equilibrium positions in space. Still, the forces will keep the molecules from departing too far from each other. This explains why volume changes are relatively small for a liquid.

- In the gaseous phase, the distances between the molecules have become so large that intermolecular forces play a minor role. The molecules move about each other with high velocities and interact through elastic impacts. The molecules will disperse throughout the vessel containing the gas. The pressure against the vessel walls is a consequence of the molecular effects.

- In the solid phase, there is no longer a clear distinction between molecules and atoms. In the equilibrium state, the atoms vibrate about fixed positions in space. The solid phase is realised in either of two ways : In the amorphous state, the molecules are not arranged in any definite pattern. In the crystalline state, the molecules are arranged in rows and planes within certain subspaces called crystals [2].

I.2 Definition of fluids

A common property of liquids and gases is that they, at rest, only can transmit a pressure normal to solid or liquid surfaces bounding the liquid or gas. Tangential forces on such surfaces will first occur when there is relative motion between the liquid or gas and the solid or liquid surface. Such forces are experienced as frictional forces on the surface of bodies moving through air or water. When it studies the flow in a river, it sees that the flow velocity is most significant in the middle of the river and is reduced to zero at the riverbank. Tangential forces explain the phenomenon of shear stresses between the water layers that try to slow down the flow. The volume of an element of flowing liquid is nearly constant. This means a fluid's density, mass per unit volume, is almost constant. Fluids are, therefore, usually considered to be incompressible. The compressibility of a liquid changes in volume and density comes into play when convection and acoustic phenomena are considered [2].

All kinds of shear behaviour, which can be described rheologically scientifically, can be viewed as being between two extremes : the flow of ideally viscous liquids on the one hand and the deformation of ideally elastic solids on the other. The behaviour of all real materials is based on the combination of a viscous and an elastic portion ; therefore, it is called viscoelastic. For example, wall paper paste is a viscoelastic liquid, and a gum eraser is a viscoelastic solid [1].

Liquids		Solids	
(ideal-) viscous	Viscoelastic	Viscoelastic	(ideal-) elastic
Flow behaviour	Flow behaviour	Deformation Behaviour	Deformation Behaviour
Newton's law	Maxwell's law	Kelvin/Voigt's	Hooke's law
Flow/Viscosity curves		Creep tests, relaxation tests, oscillatory tests	

Table I.1 – Overview of different kinds of rheological behaviour [1].

I.3 Shear stress and viscosity

Isaac Newton gave attention to fluids, and in the "Principia" published in 1687 there appears the following hypothesis associated with the steady simple shearing flow shown in Figure I.1, The resistance which arises from the lack of slipperiness of the parts of the liquid, other things being equal, is proportional to the velocity with which the liquid parts are separated from one another [3].

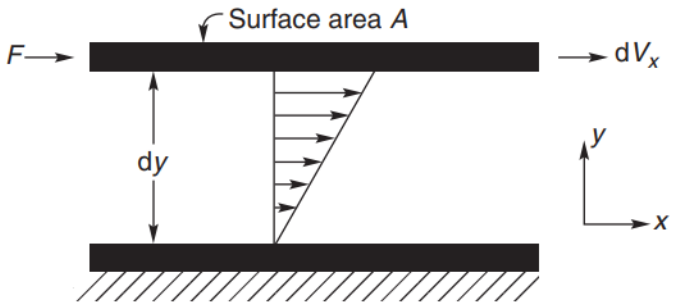

Figure I.1 – Schematic representation of the unidirectional shearing flow [4].

For the simple shear illustrated in Figure I.1, a "shear stress" σ results in "flow". In the case of a Newtonian fluid, the flow persists as long as the stress is applied. In contrast, for a Hookean solid, shear stress σ applied to the surface $(y = d)$ results in an instantaneous deformation as shown in Figure I.2. Once the deformed state is reached there is no further movement, but the deformed state persists as long as the stress is applied. The angle γ is called the "strain" and the relevant 'constitutive equation' is $\sigma = G\gamma$ where G is referred to as the "rigidity modulus" . This lack of slipperiness is what it now calls "viscosity". It is synonymous with "internal friction" and is a measure of "resistance to flow". The force per unit area required to produce the motion is F/A and is denoted by σ and is proportional to the "velocity gradient" or "shear rate" U/d. The constant of proportionality is called the coefficient of viscosity [3].

$$\sigma = \mu U/d \tag{I.1}$$

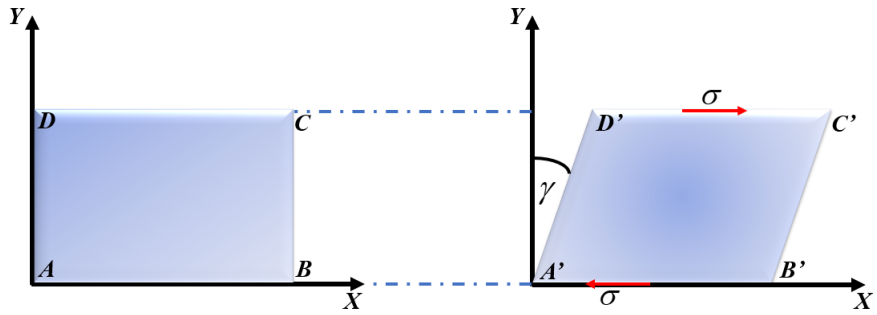

Figure I.2 – The result of applying a shear stress σ to a block of Hookean solid.

Viscosity (μ) is just one of several rheological properties that can be used for material characterisation in engineering applications. To define viscosity, consider an element of fluid sandwiched between two parallel plates of area (A) separated by a gap (L) subjected to a steady-shear force (F), on its upper face [5].

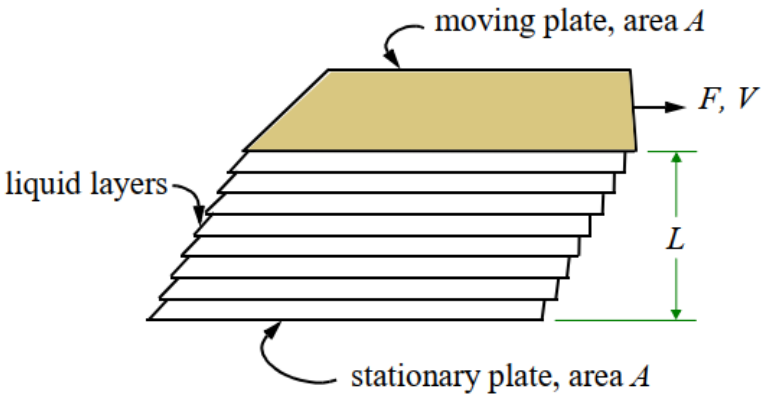

Figure I.3 – Fluid under steady-shear, the steady shear force will cause the upper plate to move with a velocity, V, relative to the lower plate [5].

$$\tau = \frac{F}{A} \tag{I.2}$$

and flows with a shear rate :

$$\dot{\gamma} = \frac{V}{L} \tag{I.3}$$

Dividing the shear stress by the shear rate gives a measure of the resistance of the fluid to flow, that is, its viscosity, defined as [5] :

$$\mu = \frac{\tau}{\dot{\gamma}} \tag{I.4}$$

I.4 Classification of fluids

The fluids classify in two different ways ; either according to their response to the externally applied pressure or according to the effects produced under the action of shear stress. The first scheme of classification leads to the so-called "compressible" and "incompressible" fluids, depending upon whether or not an element of fluid's volume depends on its pressure. While compressibility influences the flow characteristics of gases, liquids can normally be regarded as incompressible, and their response to shearing is of greater importance. The flow characteristics of single phase liquids, solutions, and pseudo-homogeneous mixtures such as (slurries, emulsions,gas–liquid dispersions), which may be treated as a continuum if they are stable in the absence of turbulent eddies, are considered depending upon their response to externally imposed shearing action [4].

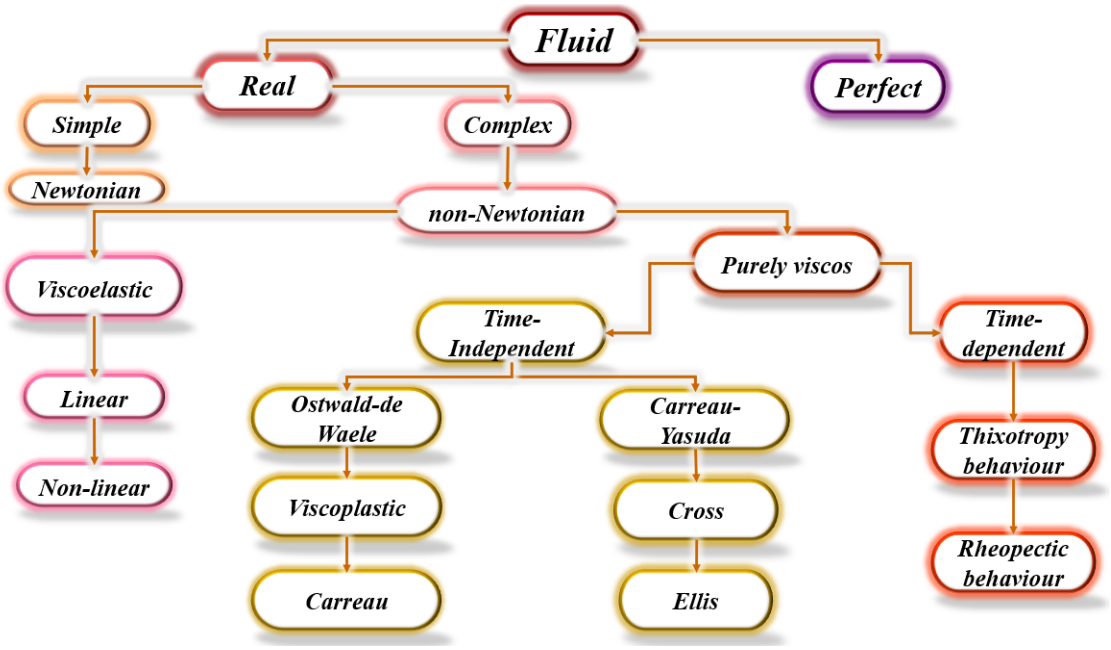

Figure I.4 – Classification of fluids.

I.4.1 Newtonian fluids

Newtonian fluids are defined to be those fluids exhibiting a direct proportionality between stress τ and strain rate $\dot{\gamma}$ in laminar flow, that is :

$$\tau = \mu\dot{\gamma} \tag{I.5}$$

The viscosity μ is independent of the strain rate, it might be affected by other physical parameters, like temperature and pressure, for a given fluid system. Newtonian fluid's stress versus strain rate graph will be a straight line through the origin. In more precise technical terms, Newtonian fluids are characterised by the assumption that the extra stress tensor, which

is part of the total stress tensor that represents the shear and extensional stresses caused by the flow excluding hydrostatic pressure, is a linear isotropic function of the components of the velocity gradient, and therefore exhibits a linear relationship between stress and the rate of strain. In tensor form, which takes into account both shear and extension flow components, this linear relationship is expressed by Equation I.5 where τ is the extra stress tensor and $\dot{\gamma}$ is the rate of strain tensor which describes the rate at which neigh-boring particles move with respect to each other independent of superposed rigid rotations. Newtonian fluids are generally featured by having shear and time-independent viscosity, zero normal stress differences in simple shear flow, and simple proportionality between the viscosities in different types of deformation [6].

I.4.2 Non-Newtonian fluids

Fluids that show a departure from Newtonian behaviour are termed as non-Newtonian fluids. When a material's flow behaviour follows the basic law of viscosity proposed by Isaac Newton, it is said to depict Newtonian behaviour. The constitutive equation for Newtonian fluids, which show constant viscosity without any yield stress and/or elastic component, is given as :

$$\tau = \mu\dot{\gamma} \tag{I.6}$$

Where τ is the shear stress, $\dot{\gamma}$ is the shear rate, and the constant μ is the Newtonian viscosity. In general, for determining velocity distributions and stresses, incompressible Newtonian fluids at constant temperature can be characterised by two material constants, namely, the shear viscosity μ and the density ρ. Once these quantities are measured, the velocity distribution and the stresses in the fluid, in principle, can be found for any flow situation. In other words, different isothermal experiments on a Newtonian fluid would yield a single constant material property : its viscosity where milli-Pascals seconds $(mPa.S)$. Some examples of commonly known Newtonian fluids are : water $(\mu \approx 1mPa.\text{S})$, coffee cream $(\mu \approx 10mPa.\text{S})$, olive oil $(\mu \approx 10^2mPa.\text{S})$ and honey $(\mu \approx 10^4mPa.\text{S})$.

Non-Newtonian fluids can depict elastic, viscous, or viscoelastic behaviour and exhibit one of the following features :

- Time-independent fluids are those for which the strain rate at a given point solely depends upon the instantaneous stress.
- Viscoelastic fluids are those that show partial elastic recovery upon the removal of deforming stress. Such materials possess properties of both viscous fluids and elastic solids.
- Time-dependent fluids are those for which the strain rate is a function of both the ma-

gnitude and the duration of stress and possibly the time lapse between consecutive stress applications [7].

I.4.2.1 Ostwald de Waele

The Ostwald de Waele, or power-law model, is one of the simplest time-independent fluid models as it contains only two parameters. The relation gives the model :

$$\mu = K\dot{\gamma}^{n-1} \tag{I.7}$$

Where μ is the viscosity, K is the consistency factor, $\dot{\gamma}$ shear rate, and (n) is the flow behaviour index [6].

Shear-thinning or pseudoplastic fluids

This is behaviour in which an infinitesimal shear stress will initiate flow (that is, the flow curve passes through the origin) and for which the rate of increase in shear stress with shear rate decreases with increasing shear rate as is shown in Figure I.5. This behaviour is sometimes incorrectly termed thixotropy because the equilibrium flow curve of a thixotropic material is often shear-thinning. However, unlike shear-thinning behaviour, thixotropy is time-dependent [5].

Shear-thickening or dilatant fluid

This is behaviour in which an infinitesimal shear stress will initiate flow (that is, the flow curve passes through the origin) and for which the increase in shear stress with shear rate increases with increasing shear rate. This is shown in Figure I.5 [5].

I.4.2.2 Viscoplastic behaviour

This type of fluid behaviour is characterised by the existence of a yield stress (τ_0) which must be exceeded before the fluid will deform or flow. Conversely, such a material will deform elastically (or flow a masse like a rigid body) when the externally applied stress is smaller than the yield stress. Once the magnitude of the external stress has exceeded the yield stress value, the flow curve may be linear or non-linear but will not pass through the origin Figure I.6 [4].

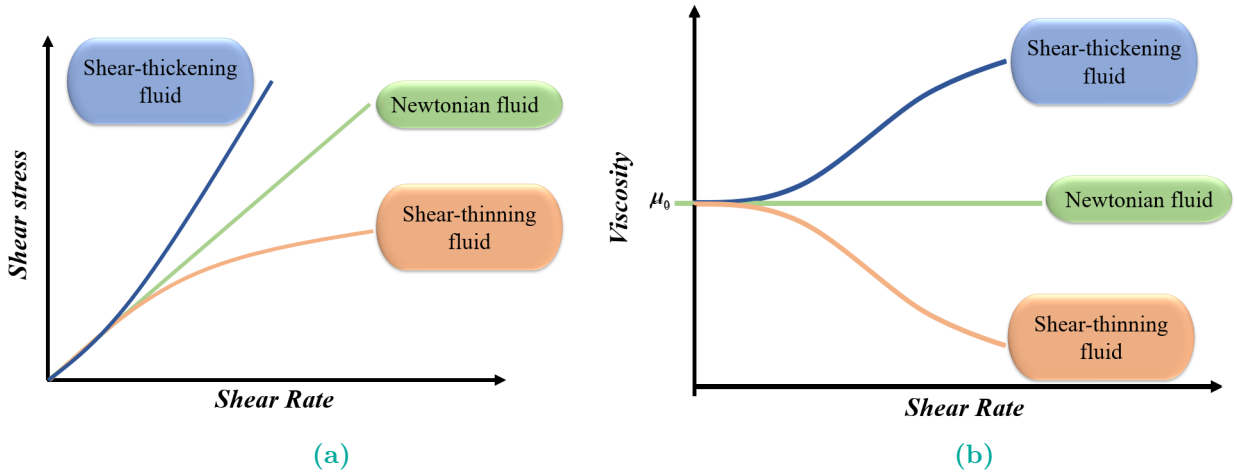

Figure I.5 – Flow curve for fluids exhibiting shear-thickening and shear-thinning behaviour.

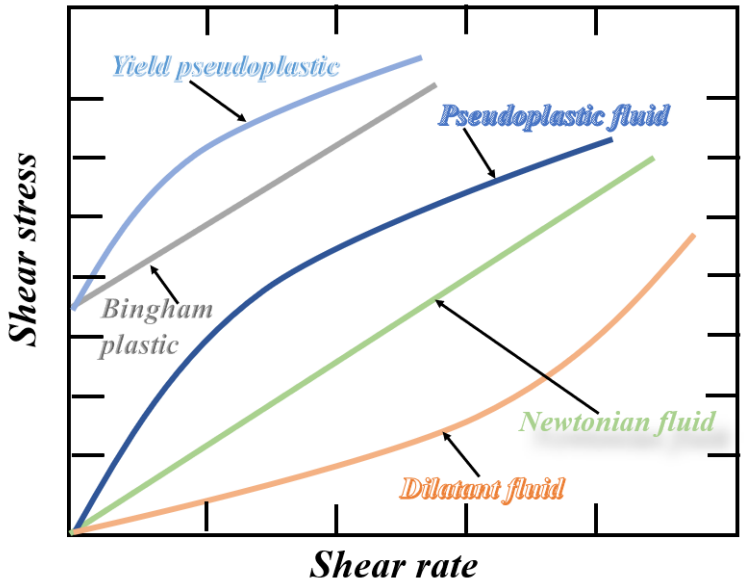

Figure I.6 – Viscoplastic fluid.

Bingham fluid

The Bingham fluid model is characterised by yield stress τ_y which, if exceeded, makes the material flow like a viscous Newtonian fluid or else behave like a solid at all values below critical stress. Hence, the equations for this fluid are as follows :

$$\begin{aligned} \tau &= \tau_0 + \mu'(\dot{\gamma}) \qquad \text{for } |\tau| > |\tau_0| \\ \dot{\gamma} &= 0 \qquad\qquad\quad \text{for } |\tau| < |\tau_0| \end{aligned} \tag{I.8}$$

Here, μ_P is called plastic viscosity [7].

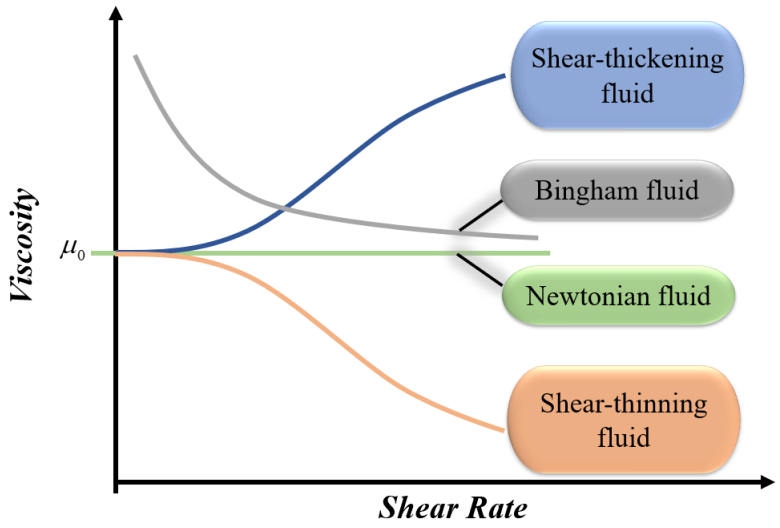

Figure I.7 – Viscosity and time-independent flow behaviour.

Herschel-Bulkley model

This fluid model was developed by Herschel and Bulkley (1926) specifically for describing pseudoplastic fluids with yield stress and is given as follows :

$$\begin{aligned} \tau &= \tau_0 + \mu'(\dot{\gamma})^n \quad \text{for } |\tau| > |\tau_0| \\ \dot{\gamma} &= 0 \quad \text{for } |\tau| < |\tau_0| \end{aligned} \tag{I.9}$$

It can be seen that when yield stress is absent, this model is akin to the Ostwald de Waele power-law model and when $(n = 1)$, represents the Bingham plastic model [7].

Casson model

Many foodstuffs and biological materials, especially blood, are well described by these two constant models :

$$(|\tau_{yx}|)^{1/2} = \left(\left|{\tau_0}^C\right|\right)^{1/2} + \left(\mu_C \left|\dot{\gamma}_{yx}\right|\right)^{1/2} \text{for } |\tau_{yx}| > \left|{\tau_0}^C\right| \tag{I.10}$$

$$\dot{\gamma} = 0 \qquad \text{for } |\tau_{yx}| > \left|{\tau_0}^C\right| \tag{I.11}$$

This model has often been used for describing the steady shear stress shear rate behaviour of blood, yoghurt, molten chocolate, etc. The flow behaviour of some particulate suspensions also closely approximates to this type of behaviour [4].

I.4.2.3 Carreau model

This four parameter rheological model can describe shear-thinning fluids with no yield stress. It is generally praised for its compliance with experiments. The distinctive feature of this model is the presence of low and high-shear plateaux. The relation gives the Carreau fluid :

$$\mu = \mu_\infty + \frac{\mu_0 - \mu_\infty}{\left[1 + (\dot{\gamma}\, t_c)^2\right]^{\frac{1-n}{2}}} \tag{I.12}$$

Where μ is the fluid viscosity, μ_∞ is the viscosity at the infinite shear rate, μ_0 is the viscosity at zero shear rate, $\dot{\gamma}$. is the shear rate, t_c is a characteristic time and n is the flow behaviour index. A generic graph demonstrating the bulk rheology is shown in Figure I.9 [6].

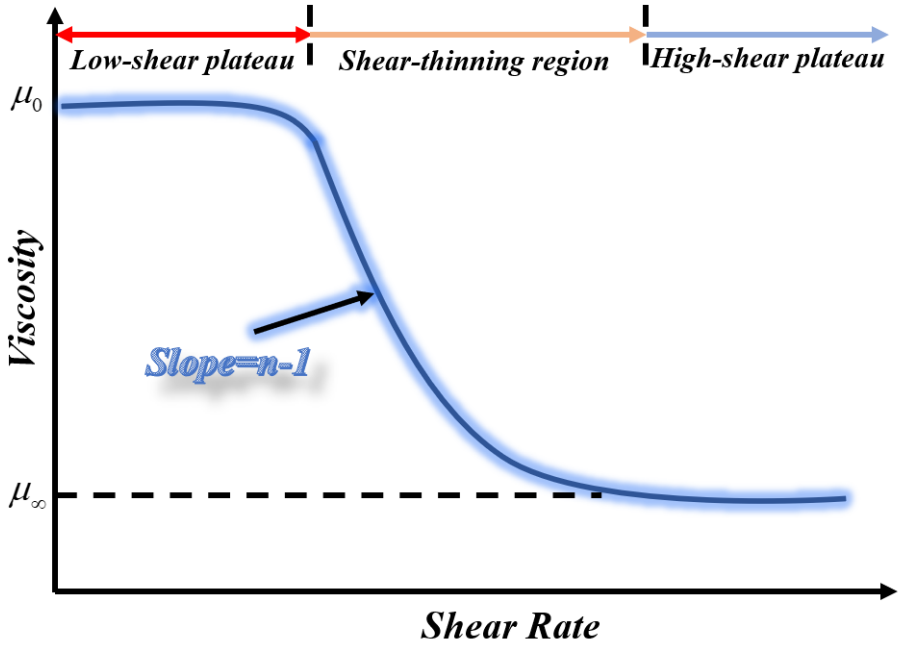

Figure I.8 – The bulk rheology of a Carreau fluid on logarithmic scales for finite shear rates ($\dot{\gamma} > 0$).

I.4.2.4 Carreau-Yasuda model

The Carreau-Yasuda Model is another empirical equation used to fit non-Newtonian data (Bird et al., 1987), also "describing pseudoplastic flow with asymptotic viscosities at zero and infinite shear rates, and with no yield stress" (Hackley and Ferraris, 2001). This model is well suited for fluids that are beginning to shear thin, and can be used to describe emulsions, biopolymer solutions, protein solutions, and polymeric solutions. [8]

$$\mu(\dot{\gamma}) = \left[1 + (\lambda\dot{\gamma})^a\right]^{\frac{n-1}{a}}(\mu_0 - \mu_\infty) + \mu_\infty \tag{I.13}$$

I.4.2.5 Cross model

Another parameter model which has gained wide acceptance is due to Cross (1965) which, in simple shear, is written as :

$$\frac{\mu - \mu_\infty}{\mu_0 - \mu_\infty} = \frac{1}{1 + k(\dot{\gamma_{yx}})^n} \tag{I.14}$$

In EquationI.14, $(n < 1)$ and k are two fitting parameters whereas μ_0 and μ_∞ are the limiting values of the apparent viscosity at low and high shear rates, respectively. This model reduces to the Newtonian fluid behaviour as $k \to 0$. Similarly, when $\mu << \mu_0$ and, it reduces to the familiar power-law model. Though initially Cross (1965) suggested that a constant value of $n = 2/3$ was adequate to approximate the viscosity data for many systems, it is now thought that treating the index (n) as an adjustable parameter offers a considerable improvement over the use of the constant value of (n) [4].

I.4.2.6 Ellis model

This is a three-parameter model that describes time-independent shear-thinning non-yield-stress fluids. It is used as a substitute for the power-law model and is appreciably better than the power-law in matching experimental measurements. Its distinctive feature is the low-shear Newtonian plateau without a high-shear plateau. According to this model, the fluid viscosity μ is given by :

$$\mu = \frac{\mu_0}{1 + \left(\frac{\tau}{\tau_{1/2}}\right)^{\alpha - 1}} \tag{I.15}$$

Where μ_0 is the low-shear viscosity, τ is the shear stress, $\tau_{1/2}$ is the shear stress at which $\mu = \mu_0/2$ and α is an indicial parameter related to the power-law index by $\alpha = 1/n$. A generic graph demonstrating the bulk rheology, that is viscosity versus shear rate on logarithmic scales, is shown in Figure I.9 [6].

I.4.2.7 Thixotropy behaviour

In the case of materials showing thixotropic behaviour, the shear rate is a function of the magnitude and duration of shear and possibly of the time lapse between consecutive applications of shear stress. These materials exhibit a reversible decrease in shear stress with time at a constant rate of shear and fixed temperature. The shear stress, of course, approaches some limiting value [7].

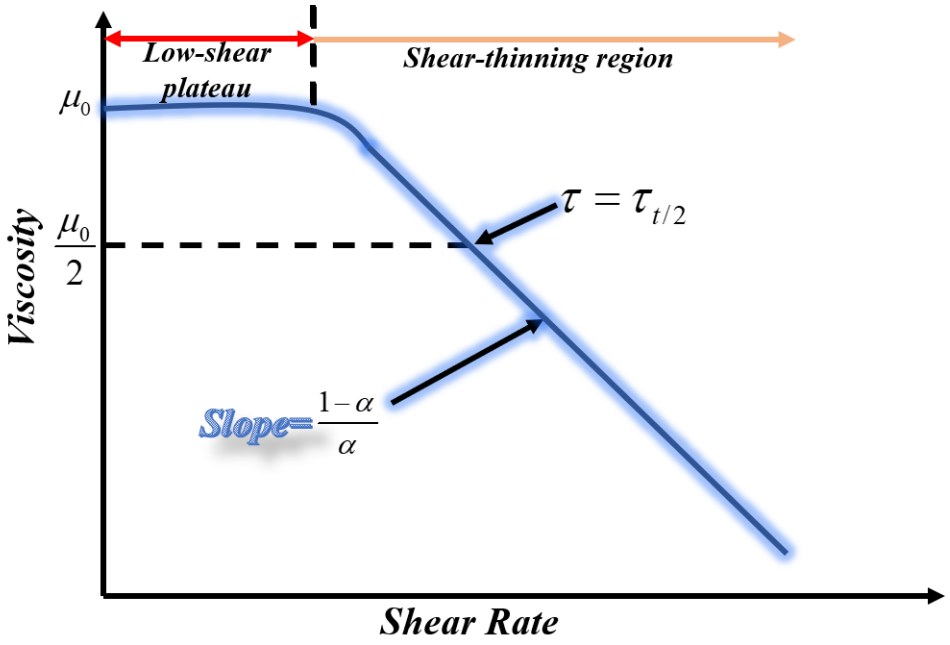

Figure I.9 – The bulk rheology of an Ellis fluid on logarithmic scales for finite shear rate ($\dot{\gamma} > 0$).

I.4.2.8 Rheopectic behaviour

Materials showing rheopectic behaviour exhibit a reversible increase in shear stress with time at a constant rate of shear and fixed temperature. At any given shear rate, the shear stress increases to approach an asymptotic maximum value [7].

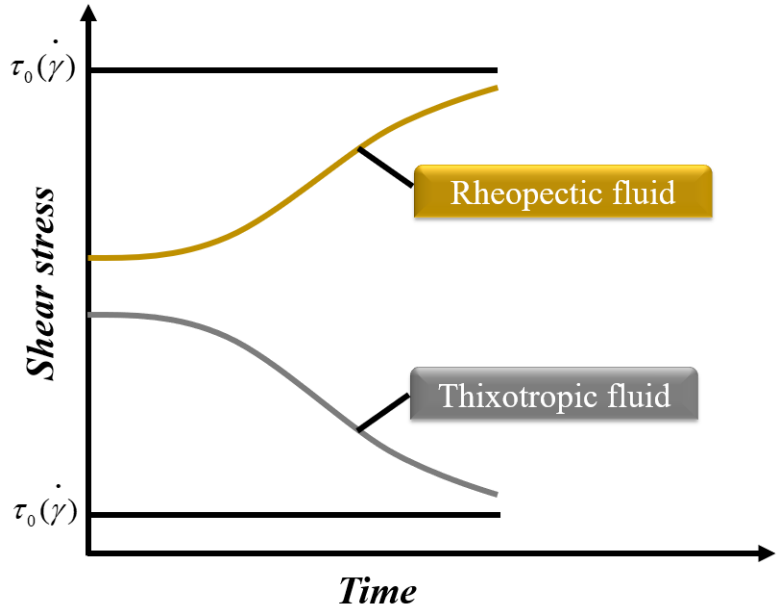

Figure I.10 – Thixotropic and rheopectic : variation of the apparent viscosity in function of time at a fixed shear rate.

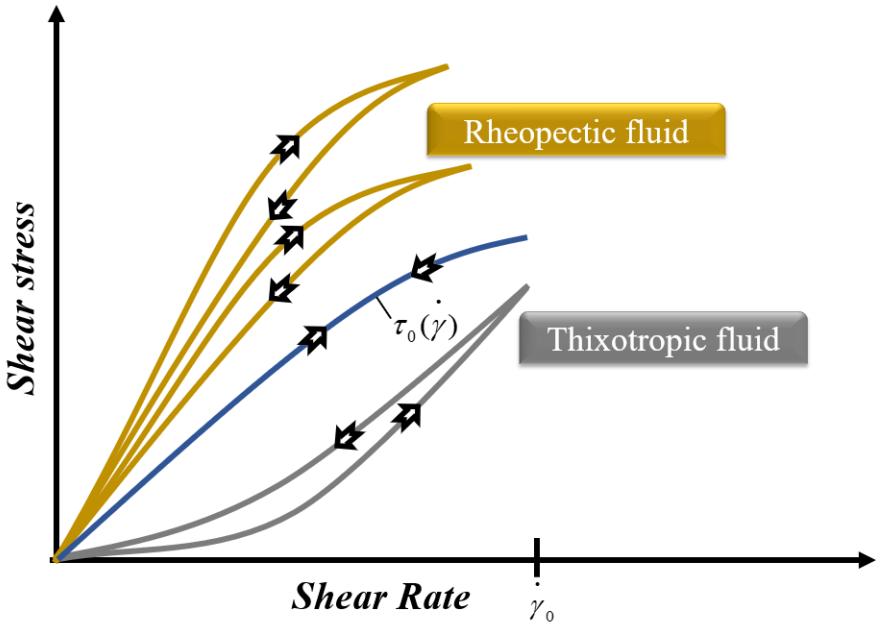

Figure I.11 – Thixotropic and rheopectic behaviour.

I.4.2.9 Viscoelastic fluids

Polymeric fluids often show strong viscoelastic effects. These include shear-thinning, extension-thickening, normal stresses, and time-dependent rheology. No theory is yet available to describe the observed viscoelastic phenomena in various flows adequately. Nonetheless, many differential and integral constitutive models have been proposed in the literature to describe the viscoelastic flow. What is common to all these is the presence of at least one characteristic time parameter to account for the fluid memory, that is the stress at present depends upon the strain or rate of strain for all past times, but with a fading memory. Viscoelasticity is divided into two major fields : linear and non-linear.

Maxwell model

This is the first known attempt to obtain a viscoelastic constitutive equation. This simple linear model, with only one elastic parameter, combines the ideas of fluids' viscosity and the solids' elasticity to arrive at an equation for viscoelastic materials. Maxwell proposed that fluids with both viscosity and elasticity can be described, in modern notation, by the relation :

$$\tau + \lambda_1 \frac{\partial \tau}{\partial t} = \mu_0 \dot{\gamma} \tag{I.16}$$

where τ is the extra stress tensor, λ_1 is the fluid relaxation time, t is time, μ_0 is the low shear viscosity and $\dot{\gamma}$ is the rate of the strain tensor [6].

Jeffreys model

This is a linear model proposed as an extension to the Maxwell model by including a time derivative of the strain rate, that is :

$$\tau + \lambda_1 \frac{\partial \tau}{\partial t} = \mu_0 \left(\dot{\gamma} + \lambda_2 \frac{\partial \dot{\gamma}}{\partial t} \right) \tag{I.17}$$

Where λ_2 is the retardation time that accounts for the corrections of this model and can be seen as a measure of the time the material needs to respond to deformation. The Jeffreys model has three constants : a viscous parameter μ_0, and two elastic parameters, λ_1 and λ_2. The model reduces to the linear Maxwell when $\lambda_2 = 0$, and to the Newtonian when $\lambda_1 = \lambda_2 = 0$. As observed by several authors, the Jeffreys model is one of the most suitable linear models to compare with the experiment [6].

Upper Convected Maxwell (UCM) Model

The Upper Convected Maxwell (UCM) is the simplest non-linear viscoelastic model and is one of the most popular models in numerical modelling and simulation of viscoelastic flow. Like its linear counterpart, it is a simple combination of the Newton's law for viscous fluids and the derivative of Hook's law for elastic solids. Because of its simplicity does not fit the rich variety of viscoelastic effects which can be observed in complex rheological materials.

However, it is largely used as the basis for other more sophisticated viscoelastic models. Like the linear Maxwell, it represents purely elastic fluids with shear-independent viscosity, Boger fluids. UCM also predicts an elongation viscosity three times the shear viscosity, like Newtonian, which is unrealistic for most viscoelastic fluids. The UCM model is obtained by replacing the partial time derivative in the differential form of the linear Maxwell with the upper convected time derivative, that is

$$\tau + \lambda_1 \overset{\nabla}{\tau} = \mu_0 \dot{\gamma} \tag{I.18}$$

where τ is the extra stress tensor, λ_1 is the relaxation time, μ_0 is the low-shear viscosity, $\dot{\gamma}$ is the rate of the strain tensor, and $\overset{\nabla}{\tau}$ is the upper convected time derivative of the stress tensor. This time derivative is given by [6].

$$\overset{\nabla}{\tau} = \frac{\partial \tau}{\partial t} + v \,.\nabla \tau - (\nabla v)^T.\tau - \tau.\nabla v \tag{I.19}$$

Oldroyd-B Model

The Oldroyd model is a simple form of the more elaborate and rarely used Oldroyd-B constant model which also contains the upper convected, the lower convected, and the corotational Maxwell equations as special cases. Oldroyd-B is the second simplest non-linear viscoelastic model and is apparently the most popular in viscoelastic flow modelling and simulation. It is the non-linear equivalent of the linear Jeffreys model, as it takes account of frame invariance in the non-linear regime.

Oldroyd-B model can be obtained by replacing the partial time derivatives in the differential form of the Jeffreys model with the upper convected time derivatives

$$\tau + \lambda_1 \overset{\nabla}{\tau} = \mu_0 \left(\dot{\gamma} + \lambda_2 \overset{\nabla}{\dot{\gamma}} \right) \tag{I.20}$$

Where $\overset{\nabla}{\dot{\gamma}}$ is the upper convected time derivative of the rate of strain tensor given by :

$$\overset{\nabla}{\dot{\gamma}} = \frac{\partial \dot{\gamma}}{\partial t} + v.\nabla\dot{\gamma} - (\nabla v)^T.\dot{\gamma} - \dot{\gamma}.\nabla v \tag{I.21}$$

Oldroyd-B model reduces to the UCM when $\lambda_2 = 0$, and to Newtonian when $\lambda_1 = \lambda_2 = 0$. Despite the simplicity of the Oldroyd-B model, it shows good qualitative agreement with experiments, especially for dilute solutions of macromolecules and Boger fluids. The model can describe two main features of viscoelasticity : normal stress difference and stress relaxation. It predicts a constant viscosity and first normal stress difference with zero second normal stress difference. Moreover, the Oldroyd-B, like the UCM model, predicts an elongation viscosity that is three times the shear viscosity, as it is the case in Newtonian fluids. It also predicts an infinite extensional viscosity at a finite extensional rate, which is physically unrealistic [6].

Model	Constitutive Equation	Viscosity	Rheological Parameters
Newtonian	$\tau = \mu\dot{\gamma}$	$\mu = \mu_N$	μ_N $(Pa\ s)$
Ostwald de Waele	$\tau = K\dot{\gamma}^n$	$\mu = K\dot{\gamma}^{n-1}$	K $(Pa\ s^n)$ n dimensionless
Bingham Plastic	$\tau = \tau_{yB} + \mu_B\dot{\gamma}$	$\mu = \frac{\tau_{yB}}{\dot{\gamma}} + \mu_B$	τ_{yB} (Pa) μ_B $(Pa\ s)$
Herschel-Bulkley	$\tau = \tau_{yHB} + K\dot{\gamma}^n$	$\mu = \frac{\tau_{yHB}}{\dot{\gamma}} + K\dot{\gamma}^{n-1}$	τ_{yHB} (Pa) K $(Pa\ s^n)$ n dimensionless
Casson	$\sqrt{\tau} = \sqrt{\tau_{yC}} + \sqrt{\mu_C\dot{\gamma}}$	$\mu = \frac{\left[\sqrt{\tau_{yC}} + \sqrt{\mu_C\dot{\gamma}}\right]^2}{\dot{\gamma}}$	τ_{yC} (Pa) μ_C $(Pa\ s)$
Vocadlo	$\tau = ({\tau_{yV}}^{1/n} + K\dot{\gamma})^n$	$\mu = \frac{({\tau_{yV}}^{1/n} + K\dot{\gamma})^n}{\dot{\gamma}}$	τ_{yV} (Pa) K $(Pa\ s^n)$ n dimensionless
Prandtl-Eyring	$\tau = a\sinh^{-1}(b\dot{\gamma})$	$\mu = \frac{\left[a\sinh^{-1}(b\dot{\gamma})\right]}{\dot{\gamma}}$	a (Pa) b (s)
Powell-Eyring	$\tau = c\dot{\gamma} + a\sinh^{-1}(b\dot{\gamma})$	$\mu = c + \frac{\left[a\sinh^{-1}(b\dot{\gamma})\right]}{\dot{\gamma}}$	a (Pa) b (s) c $(Pa\ s)$
Cross	$\tau = \left\{\mu_\infty + \frac{\mu_0-\mu_\infty}{1+a\dot{\gamma}^m}\right\}\dot{\gamma}$	$\mu = \mu_\infty + \frac{\mu_0-\mu_\infty}{1+a\dot{\gamma}^m}$	μ_0 $(Pa\ s)$ μ_∞ $(Pa\ s)$ a (S^m) m dimensionless
Sisko	$\tau = \left\{\mu_\infty + K\dot{\gamma}^{n-1}\right\}\dot{\gamma}$	$\mu = \mu_\infty + K\dot{\gamma}^{n-1}$	μ_∞ $(Pa\ s)$ K $(Pa\ s^n)$ n dimensionless
Carreau	$\tau = \left\{\mu_\infty + \frac{\mu_0-\mu_\infty}{\left[1+(a\dot{\gamma})^2\right]^{m/2}}\right\}\dot{\gamma}$	$\mu = \mu_\infty + \frac{\mu_0-\mu_\infty}{\left[1+(a\dot{\gamma})^2\right]^{m/2}}$	μ_0 $(Pa\ s)$ μ_∞ $(Pa\ s)$ a (S) m dimensionless
Van Wazer	$\tau = \left\{\mu_\infty + \frac{\mu_0-\mu_\infty}{1+a\dot{\gamma}+b\dot{\gamma}^m}\right\}\dot{\gamma}$	$\mu = \mu_\infty + \frac{\mu_0-\mu_\infty}{1+a\dot{\gamma}+b\dot{\gamma}^m}$	μ_0 $(Pa\ s)$ μ_∞ $(Pa\ s)$ a (S) b (S^m) m dimensionless
Williamson	$\tau = \left\{\mu_\infty + \frac{\mu_0-\mu_\infty}{1+a\tau}\right\}\dot{\gamma}$	$\mu = \mu_\infty + \frac{\mu_0-\mu_\infty}{1+a\tau}$	μ_0 $(Pa\ s)$ μ_∞ $(Pa\ s)$ a (Pa^{-1})
Reiner-Philippoff	$\tau = \left\{\mu_\infty + \frac{\mu_0-\mu_\infty}{1+a\tau^2}\right\}\dot{\gamma}$	$\mu = \mu_\infty + \frac{\mu_0-\mu_\infty}{1+a\tau^2}$	μ_0 $(Pa\ s)$ μ_∞ $(Pa\ s)$ a (Pa^{-2})
Meter	$\tau = \left\{\mu_\infty + \frac{\mu_0-\mu_\infty}{1+a\tau^m}\right\}\dot{\gamma}$	$\mu = \mu_\infty + \frac{\mu_0-\mu_\infty}{1+a\tau^m}$	μ_0 $(Pa\ s)$ μ_∞ $(Pa\ s)$ a (Pa^{-m}) m dimensionless
Ellis	$\tau = \left\{\frac{\mu_0}{1+a\tau^{m-1}}\right\}\dot{\gamma}$	$\mu = \frac{\mu_0}{1+a\tau^{m-1}}$	μ_0 $(Pa\ s)$ a (Pa^{1-m}) m dimensionless

Table I.2 – Flow curve models [5].

Fluid type	Definition	Typical examples
Pseudoplastic	Fluids that depict a decrease in viscosity with increasing shear rate and hence often referred to as shear-thinning fluids.	Blood Filled polymer systems Polymer melts Printing inks
Dilatant	Fluids that depict an increase in viscosity with increasing shear rate and hence often referred to as shear-thickening fluids.	Aqueous suspension of titanium dioxide Gum solutions Wet sand
Bingham plastics	Fluids that do not flow unless the stress applied exceeds a certain minimum value referred to as the yield stress and then show linear shear stress versus shear rate relationship.	Certain asphalts and bitumen Jellies Sewage sludges Thickened hydrocarbon greases Tomato ketchup Toothpaste
Pseudoplastic with a yield stress	Fluids that have non-linear shear stress versus shear rate relationship in addition to the presence of yield stress.	Heavy crude oils with high wax content Filled polymer systems
Thixotropic	Fluids that exhibit a the reversible decrease in shear stress with time at a constant rate of shear and fixed temperature. The shear stress, of course, approaches some limiting value.	Coal-water slurries Crude oils Drilling muds Filled polymer systems Mayonnaise Salad dressing Yoghurt
Rheopectic	Fluids exhibit a reversible increase in shear stress with time at a constant rate of shear and fixed temperature. At any given shear rate, the shear stress increases to approach an asymptotic maximum value.	Some clay suspensions
Viscoelastic	Fluids that possess the added feature of elasticity apart from viscosity. These fluids exhibit process properties which lie in-between those of viscous liquids and elastic solids	Filled polymer systems Polymer melts Polymer solutions

Table I.3 – Various types of non-Newtonian fluids [7].

CHAPTER II

PREVIOUS WORK

PREVIOUS WORK

II

The turbulence state of a fluid is one of the most challenging problems in fluid dynamics due to its importance in mechanical and engineering fields. It is often encountered in engineering applications such as heat exchangers, gas-cooled nuclear reactors and gas turbines, drilling hydraulics, sewage transport, nuclear reactors, and applications involving relatively high heat transfer rates.

One of the fundamental problems of fluid mechanics is the incompressible turbulent flow through smooth straight pipes; circular tubes are one of the most common flow passage geometries in fluid flow mechanics. The turbulent flow of Newtonian fluids through a stationary cylindrical tube is a critical challenge and significant concern in the mechanical and engineering industries that has previously attracted much attention. A range of engineering applications, including flow in turbo engines, heat exchangers, combustion chambers, nuclear reactors, etc., include turbulent flow in pipes. The fully developed turbulent flow in the straight pipe of Newtonian fluids has been extensively studied in the literature. The literature inspection reveals that many researchers reported acclaimed analytical, experimental, direct numerical simulation (DNS), and large eddy simulation (LES) data for describing flow patterns, hydrodynamic behaviour, turbulent features, mean and turbulence statistics, and instantaneous quantities, among them [9], [10], [11], [12].

Orlandi and Fatica (1997) [9] applied the direct numerical simulation in a turbulent pipe flow with and without rotation, at low Reynolds numbers. The simulation is performed by a finite difference scheme, second-order accurate in space and in time. A non-uniform grid in the radial direction yields accurate solutions with a reasonable number of gridpoints, which was $(128 \times 96 \times 257)$ in a pipe of length $L_z = 15R$ to analyse the results. With $L_z = 15R$ and with 257 points in direction (z) and the rotation rate $N = 2$. The numerical method was tested in

the non rotating case by comparing the results with the validated simulations by EUW. For the rotating case, the check of the numeric was performed only at $N = 2$, and the check must be done not only on the resolution but also on the length of the computational domain in the streamwise direction. If the pipe was too short, it could affect the long helical structures near the wall and at the centre of the pipe. From these simulations, it also understood that there is a strong interaction between numerical and sub-grid dissipation. Further details ; when the pipe rotates, a degree of drag reduction was achieved in the numerical simulations just as in the experiments. Through the visualisation of the vorticity field, the drag reduction has been related to the modification of the vortical structures near the wall. In contrast, a comparison between the vorticity in the non-rotating and in the high rotation case has shown a spiral motion leading to the transport of streamwise vorticity far from the wall.

A subject with significant industrial impact, heat transfer in Newtonian fluids is of practical importance in many industrial applications. A considerable amount of research in the past decades has addressed thermally developing turbulent forced convection of Newtonian fluids through smooth straight pipes, among them [12].

Piller (2005) [12] presented a direct numerical simulations (DNS) investigation of fully developed turbulent pipe flow and heat transfer at Reynolds number $Re_m = 5300$ based on bulk velocity and pipe diameter, and the friction Reynolds number, based on the pipe diameter, is $Re^* = 360$; the Prandtl number of the fluid is 0.71. This data provides detailed information on the mean properties and turbulence statistics up to fourth order, the budget and the wave number spectra of the temperature fluctuations, for three different wall boundary conditions. To investigate the differences between fully developed turbulent heat transfer in an axisymmetric pipe and plane channel geometry, the present DNS results are compared to those obtained from channel flow simulations. The differences between channel and pipe flow results are modest and reveal that the temperature fluctuations in the pipe are slightly more intense. The results show that the mean temperature profile does not conform to the accepted law of the wall. Then, the boundary conditions affect the turbulence statistics both in the near-wall and core regions ; this observation complements previous studies concerning different flow and heat transfer configurations.

Swirl flow is not only crucial for a wide range of real world mechanical and engineering applications, but it also has a significant theoretical interest. The flow through rotating pipes is of great practical interest because of the various industrial applications. Several computa-

tional and experimental experiments have been carried out in recent years to understand the laminarisation phenomenon better and examine the impact of the rotating pipe wall on the mean characteristics and turbulence statistics. In addition to the turbulence statistics, such as the root mean square of fluctuating velocities, Reynolds shear stresses, and the higher order statistics, emphasis has been placed on how the swirl caused by a rotating pipe wall affects the friction coefficient and velocity distribution. It is shown that the turbulent and hydrodynamic properties are influenced by the interaction between turbulence and the centrifugal force caused by the swirl. A body force that stabilises or destabilises the turbulence may also be inferred from the swirl produced by a rotating pipe wall's impact on the flow field and the practical significance of turbulent flows.

The turbulent flow of Newtonian fluids through an isothermal axially rotating pipe is a problem of considerable significance. It has received much attention because of its various industrial applications. Much literature has investigated the turbulent flow characteristics through an isothermal pipe rotating around the axis. The effects of the swirl driven by a rotating pipe wall on flow characteristics and turbulent features for Newtonian fluids have been studied either experimentally or numerically by [13], [14], [15], [16], [17], [18], [19], [20], [21], [22], [23], [24], [25], [26], [27], [28], [29], [30], [31].

Murakami and Kikuyama (1980) [13] conducted one of the first significant investigations to assess the effects of the centrifugal force induced by the rotating pipe wall on the flow pattern and hydraulic losses. To this end, Murakami and Kikuyama (1980) [13] studied the turbulent flow of Newtonian fluid through an axially smooth rotating pipe for different rotation rates and Reynolds numbers by measuring the pressure and the velocity profile distributions along the radial direction. As the rotation rate increases, the rotating pipe wall causes a significant deformation of the mean streamwise velocity profile distribution along the pipe radius. The increased rotating pipe wall results in a noticeable enhancement of the axial velocity towards the core region, where the axial velocity profile approaches a laminar shape progressively. This trend is more apparent as the pipe is rotated, called the laminarisation phenomenon.

To shed further light on the laminarisation phenomenon, Nishibori and Kikuyama (1987) [14] experimentally investigated the turbulent flow of the Newtonian fluid inside an axially rotating pipe using the laser Doppler velocimeter (LDV) and flow visualisation techniques. Their results show that the centrifugal force caused stabilisation of the rotating boundary layer due to the rotating velocity component, resulting in a laminarisation flow. This phenomenon was more

observed in the inlet region, where a non-rotating inner core exists in the pipe section. When the rotation rate was increased to a specific value, a laminarisation phenomenon was observed in the rotating layer in the inlet region near the entrance. Interestingly, when laminarisation occurs in the rotating layer near the pipe wall, the axial velocity profile becomes flat near the pipe axis, similar to that observed in the laminar inlet flow developing in a stationary pipe. Thus, the flow pattern inside the boundary layer near the pipe wall can be estimated using the shape factor based on the axial velocity profile. Moreover, under the same rotation rate conditions, the laminarisation of flow in the inlet region is promoted as the axial Reynolds number is decreased.

Eggels et al. (1994) [16] carried out one of the most significant experimental and numerical analyses and discussions of turbulent pipe flow. The experimental one was based on HWA, PIV and LDA techniques, while the numerical investigation employed direct numerical simulation (DNS). The numerical study was performed over a pipe length of $5D$ in the axial direction. The spatial resolution is $(96 \times 128 \times 256)$ gridpoints in the radial, tangential, and axial directions, respectively, at a Reynolds number of 5300; these predicted results compared reasonably with the measured results. In addition to the first study, Eggels (1994) performed several simulations for turbulent flow inside stationary and axially rotating pipes with a computation length of $5D$, employing the Large Eddy Simulation (LES) with the Smagorinsky model at a Reynolds number of 40000 and for rotation rates (N) of 0 and 0.71. Their findings suggest that the centrifugal force induced by the rotating pipe wall results in a pronounced attenuation of the normal wall and axial velocity fluctuation along the radial coordinates according to the Taylor-Proudman theorem because a rotating flow tends to become $2D$ in its plane of rotation. In other words, the radial and axial velocity fluctuations exhibit an apparent suppression as the rotating pipe rotates. Moreover, the increased rotating pipe wall induces a marked enhancement of the mean axial velocity profile in the core pipe region due to the reduction of the total shear stress and a change in the shear stress profile. In addition, the attenuation of the shear stress also leads to a reduction of the friction factor.

Yang (2000) [18] sought to reveal the effects of the centrifugal force induced by the rotating pipe wall on the flow patterns and the turbulence characteristics; LES with dynamic and Smagorinsky sub-grid models were employed to investigate numerically the fully developed turbulent flow of Newtonian fluid through an axially rotating pipe. This study was performed with a spatial resolution of $(192 \times 64 \times 128)$ gridpoints in the axial, radial, and azimuthal directions, respectively, over a computation domain length of $4D$ in the streamwise direction,

at a Reynolds number of 20000 and rotation rates of $0, 0.5$, and 1. The most relevant predicted results show that the stabilising effect of the centrifugal force induced by a rotating pipe wall results in a noticeable reduction of the turbulence intensity ; this trend is more pronounced as the pipe wall rotates. According to Eggels (1994), Yang (2000) [18] argued that the suppression of radial fluctuations leads to the Taylor-Proudman theorem, which states that in the suppression of turbulent fluctuations perpendicular to the plane of rotation, the rotating flow tends to become two-dimensional in its rotation plane.

For different Reynolds numbers and rotation rates, Ould-Rouiss and Feiz [19] conducted Direct Numerical Simulations and Large Eddy Simulations of fully developed turbulent pipe flow in an axially rotating pipe. The DNS has been performed with rotation rates ranging from 0 to 18 at two Reynolds values, $Re = 4900$ and $Re = 7400$. The dynamic model has been used to simulate large eddies up to a Reynolds number of 20600. The friction coefficient, Reynolds shear stresses, mean and fluctuating velocity components, higher-order statistics, and other statistical turbulence values are all collected and examined. This research aimed to look at how the rotation number and Reynolds number affect turbulent flow properties. The governing equations are discretised in cylindrical coordinates on a staggered mesh. A finite difference method that is second-order accurate in both space and time is used to conduct numerical integration. Time is advanced using a fractional step technique. Their findings demonstrate that the stabilising influence of the centrifugal force causes the axial velocity profile to progressively converge into a laminar form as the rotation rate increases. As a result, the friction factor goes down. The root mean square is significantly affected by the wall's rotation, and these effects are stronger for the streamwise RMS velocity. The rotation increases the two other stresses, radial and tangential Reynolds stress and tangential and axial Reynolds stress while decreasing the radial and axial Reynolds stress component. It is clear how the Reynolds number affects the radial and axial Reynolds stress distributions as well as the RMS of the axial velocity.

The convective heat transfer in swirling flows is often encountered in chemical and mechanical mixing and separation devices, electrical and turbo-machinery, combustion chambers, pollution control devices, swirl nozzles, rocketry, and fusion reactors. In these flow fields, the heat transport phenomena in connection with the flow are substantially influenced by the centrifugal force induced by the swirl. In other words, heat and momentum transport phenomena are suppressed or promoted by the centrifugal force associated with the swirl. The utilisation of heat transfer with the turbulent swirling flow has often appeared in many mechanical and chemical engineering fields ; inlet part of fluid machinery, enhancement of mixing and chemical reaction in the

combustion chamber, etc.

A modified mixing length theory was used by Reich and Beer (1989) [20] to perform fully developed, turbulent and laminar free and forced convection flows of Newtonian fluids through axially stationary and rotating pipes. They conducted extensive analytical and experimental research on the flow and thermal patterns. The fluid temperature along the pipe radius, the friction factor, and the axial and azimuthal velocity distribution were all examined and critically discussed by Reich and Beer (1989) [21] in order to reveal the effects of the rotation rate on the hydrodynamic and thermal characteristics in such a situation. According to Reich and Beer's (1989) [21] theoretical and experimental observations, free convection disappears as the rotating Reynolds number rises. It is also shown that the laminar flow changes to turbulent flow as a result of the spinning pipe wall's destabilising influence. However, Reich and Beer's (1989) [21] results demonstrate that the spinning pipe wall significantly reduces the flow resistance and heat transmission due to turbulent radial suppression brought on by the radially increasing centrifugal forces. Furthermore, there is a clear flow laminarisation seen in both the projected and actual velocity and temperature profiles.

Satake and Kunugi (2002) [28] applied a direct numerical simulation for fully developed turbulent flow and heat transfer in axially rotating flow. In this study, the Reynolds and Prandtl numbers of the working fluid were assumed to be respectively 5283 and 0.7, with several grid-points in axial, radial, and tangential directions, respectively ; and the rotating ratios of a wall The ratio of velocity to bulk velocity was set to be 0.5, 1, 2, and 3. The turbulent quantities were obtained, such as the mean flow, temperature fluctuations, turbulent stresses and pressure distribution, and turbulent statistics. The results show that the turbulent drag decreases with the rotating ratio increase ; the reason for this drag reduction can be considered as the additional rotational production terms that appear in the azimuthal turbulence component. Then, the contributions of convection and production terms to the radial scalar flux budget and the balance with temperature pressure gradient terms are significant. For accuracy, the dissipation and viscous diffusion terms are negligible at a higher rotating ratio.

Redjem et al. (2007) [29] treated direct numerical simulations of heat transfer in a fully developed turbulent pipe flow with isoflux condition imposed at the wall for a Reynolds number based on pipe radius $Re = 5500$. Another interesting is establishing databases of various turbulence statistics of turbulent transport phenomena at different Prandtl numbers (Pr is less than

or equal to 1). These databases help evaluate and develop turbulence models, especially for describing heat transfer in turbulent pipe flow with Pr being less than or equal to 1. They are based on the Prandtl number effects on turbulent heat transfer in pipe flow. They analysed the different statistical turbulence quantities, including the mean and fluctuating temperatures, the heat transfer coefficients, and the turbulent heat fluxes. Also, the scaling of mean temperature profiles is investigated to derive the correct logarithmic law for various Prandtl. The results are summarised ; the RMS of temperature fluctuations and turbulent heat fluxes are found to increase when increasing the Prandtl number. The radial distributions of higher order statistics (skewness and flatness) confirm the intermittent behaviour in the close vicinity of the wall ; this intermittent behaviour is more pronounced with an increase in the Prandtl number.

In-depth research on the numerical analysis of both hydrodynamic and thermal characteristics was conducted by Ould-Rouiss et al. in 2010 [30]. The DNS and LES techniques of the fully developed forced convection heat transfer for airflow through a heated axially rotating pipe are the focus of this work. In fact, the pipe wall was given a thermal boundary condition of uniform heat flow, and the Reynolds number was set at 5500 for the range of rotation rates $(0 \leq N \leq 7)$. Additionally, the LES spatial resolution was based on a mesh of $(39 \times 129 \times 129)$ gridpoints in the radial, tangential, and axial directions, while the DNS spatial resolution was based on a mesh of $(129 \times 129 \times 257)$ gridpoints. The rise in temperature variations toward the core of the pipe as rotates is shown to have a clear tendency to increase the turbulence intensity of temperature fluctuations in the core flow zone. Additionally, as the spinning pipe diameter rises, the centrifugal force caused by the revolving pipe wall causes a noticeable decrease in the axial turbulent heat flow and an increase in the azimuthal heat flux. On the other hand, the flow and the scalar transport seem to be almost independent of the revolving pipe wall with a larger rotation rate $(N > 3)$.

Bousbai et al. (2013) [31] investigated the turbulent heat transfer characteristics for water flow in the rotating pipe under iso-flux conditions, using the LES technique for different rotation rates $(0 < N < 14)$ and a Reynolds number $Re = 5500$. The computational length in the axial direction $L = 20R$ with grid resolution this study is to examine the effect of rotation on turbulent heat transfer to complement existing literature and the effectiveness of the LES method for predicting turbulent heat transfer for water flow in a rotating pipe. They have confirmed that the streamwise turbulent heat flux is significantly reduced when N increases, whereas the azimuthal turbulent heat flux is damped near the wall for a low rotation rate. It's

reduced with increasing N for $(N > 3)$. Therefore, the deviation of temperature profile from log-law is more pronounced in water flow than in airflow. Then the fluctuating temperature and turbulent heat fluxes in water flow seem to be more affected by the rotation ratio than those in airflow. The pipe rotation diminishes the thickness of conductive and dynamic sub-layers. The effect of the rotation ratio on the peak's position of fluctuating velocities,turbulent heat fluxes, temperatures and shear stresses has also been analysed.

Materials exhibiting shear-thinning non-Newtonian behaviour include slurries, pastes, suspended solids in liquids, and emulsions. Shear-thinning materials are frequently encountered in industries dealing with composite materials, rubber, pharmaceuticals, biological fluids, plastics, petroleum, soap and detergents, cement, food products, paper pulp, paint, light and heavy chemicals, oil field operations, fermentation processes, plastic rocket propellants, electro-rheological fluids, ore processing, printing, and radioactive waste. The characterisation of the turbulent flow of non-Newtonian fluids inside the circular pipe is of practical importance due to the wide range of industrial applications of these fluids. There is only a relatively limited amount of research specifically on them due to their distinctive viscosity characteristics, which vary from those of Newtonian fluids.

The fully developed turbulent flow of non-Newtonian fluids through a smooth axially stationary pipe is a problem of considerable significance and has received much attention in the past ; the literature contains several well-documented experimental and numerical investigations. These studies have given special consideration to describing this kind of fluid's rheological and hydrodynamic behaviour by revealing the effects of various rheological parameters on flow patterns and the turbulence features in such problems [32], [33], [34], [35], [36], [37], [38], [39], [40], [41], [42], [43], [44], [45], [46], [47], [48], [49], [50], [51], [52], [53], [54], [55].

Theoretical and experimental studies of the turbulent flow of non-Newtonian fluid through axial pipes were performed by Metzner and co-workers during the $(1955 - 1959)$ [32], [33], [34]. Moreover, their work seeks to understand the rheological and hydrodynamic behaviour and flow of non-Newtonian fluids. The authors have proposed extensive theoretical and experimental studies for all three flow regions, laminar, transition, and turbulent of Ostwald de Waele fluids in pipes. Their studies show the relation ships between the generalised Reynolds number and the friction factor. Both Dodge and Metzner (1959) [34] provide a developed expression for the pressure drop, the mean flow rate allowing the prediction of non-Newtonian fluid velocity profiles, and a correlation for the friction factors as a function of the Reynolds number. Other

measurements were performed in the channel and pipe flow.

Pinho and Whitelaw (1990) [35] carried out an experimental study for non-Newtonian fluids, power-law (shear-thinning) fluids in a cylindrical pipe. This investigation means measuring the axial velocity and the three normal stresses with four different concentrations chosen of a polymer (Sodium Carboxymethyl Cellulose) in an aqueous solution and with water in a range of Reynolds numbers from 240 to 111000. The shear-thinning fluids show a marked delay in the transition from the laminar to the turbulent regime. In addition, the decrease in flow index also results in an obvious reduction in the friction factor at higher Reynolds numbers.

Malin (1997) [36] emphasises this numerical investigation of Bingham, Ostwald de Waele, and Herschel-Bulkley fluids to improve the predictions for the non-Newtonian behaviour fluids. Malin (1997) [36] performed a fully developed laminar and turbulent flow of Ostwald de Waele fluid in smooth circular tubes. Malin (1997) [36] used a modified $k-Q$ model (a low Reynolds number $k-Q$ model extended to power-law fluids) to calculate the frictional resistance and the velocity profile for fully developed laminar and turbulent flows in smooth-walled tubes. The presented results agreed with experimental data for the turbulent friction and the mean velocity profiles at various generalised Reynolds numbers and different values of the power-law index.

Direct numerical simulation of turbulent pipe flow of non-Newtonian fluids was carried out by Rudman et al. (2004) [37] using the Fourier spectral element-Fourier method at a moderate Metzner-Reed Reynolds number ($Re_{MR} \simeq 3000$ and 4000). Results for a power-law (shear-thinning) rheology agree well with experimentally determined logarithmic layer correlations and with other previously published experimental work. The aim of this investigation is the prediction of the effects of behaviour index on rheological parameters in addition to the influence of the Reynolds number of non-Newtonian fluids. Their investigation reports the results obtained numerically from shear-thinning fluids with behaviour index (n) of 0.5, 0.69, and 0.75. In addition, to the Herschel-Bulkley model through a pipe has a range of domain lengths from $4\pi D$ to $8\pi D$ with different generalised Reynolds numbers. A similar DNS study at a higher Meztner-Reed Reynolds number ($Re_{MR} = 7500$) was also carried out by Rudman and Blackburn (2012). The emerged results show that in the log-region, the velocity profile agree well with the experimental data done by Rudman et al. (2004) [37] mentioned that their friction factors predicted by the simulations are $(10-15\%)$ higher than the Dodge and Metzner correlations obtained from experiment and presented in [34].This is most likely related to the imperfect fit of the experimental fluids with power-law rheology. However, the simulation results show the

reduction in friction factor is due to the higher core viscosities that reduce the strength of the near-wall eddies, and hence momentum transfer from the core to the wall. Moreover, the results obtained also suggest that as the power-law index (n) is decreased, and the deviation from Newtonian rheology increases, the value of (Re_g) at which transition occurs will also increase.

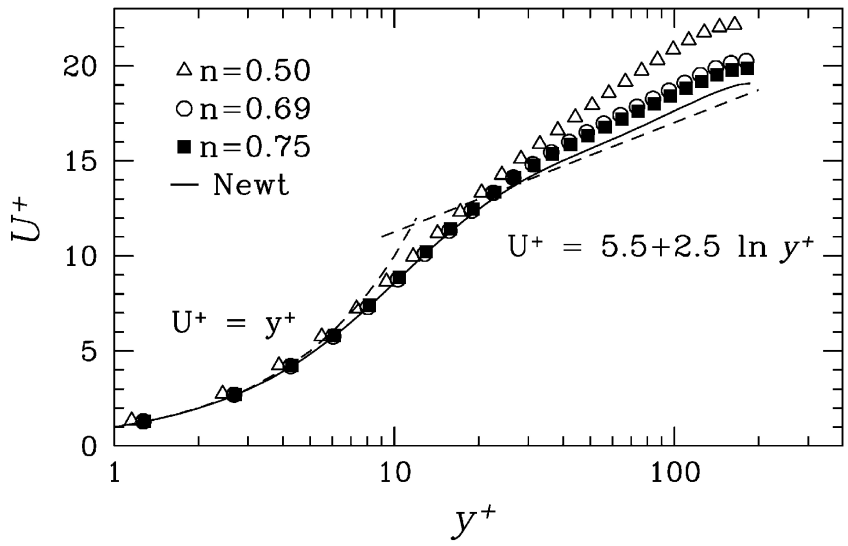

Figure II.1 – Mean axial velocity profiles for the turbulent flow of three different power-law fluids at $Re_g \approx 5500$ ($n = 0.5$, 0.69, and 0.75) [37].

Rudman and Blackburn (2006) [38] reported a direct numerical simulation (DNS) of the turbulent flow of non-Newtonian fluids using the spectral element Fourier method (SEM). The method is applied to the case of turbulent pipe flow, where simulation results of a shear-thinning fluid are compared to those of a Herschel–Bulkley fluid at the same generalised Reynolds number of 7500 with a domain length of $5\pi D$. They have also studied the flow of blood using a Carreau–Yasuda rheology model and the results were compared to those of the one-equation Spalart-Allmaras $RANS$ (Reynolds Averaged Navier-Stokes) model through a rectangular channel with a length of $5\pi D$ and a height of $2\pi D$ at the generalised Reynolds number of 3214.

To develop better computer modelling methods for wall turbulence in non-Newtonian viscous fluids, Ohta and Miyashita (2014) [39] performed the LES with the Smagorinsky model as a sub-grid scale (SGS) model extended. They carried out direct numerical simulations (DNS) and large eddy simulations (LES) of fully developed turbulent flows of various non-Newtonian fluids with viscosities described by the power-law model and the Casson model. From the results obtained, they found that performing the LES with the Smagorinsky model as a sub-grid scale (SGS) model was extended according to the results of the DNS, they evaluated the reliability of the extended SGS model.

Gavrilov and Rudyak (2016) [40] focused their studies on the development of a novel Reynolds Averaged turbulence model for flows of Ostwald de Waele fluids. The fully developed turbulent pipe flows of power-law fluids were studied by Gavrilov and Rudyak (2016) [40] using direct numerical simulation at generalised Reynolds numbers of 10000 and 20000. Five different power-law indexes (n) from 0.4 to 1 were considered, and this new model used the elliptic relaxation approach to capture the near-wall turbulence anisotropy. Thus, the distributions of components of the Reynolds stress tensor, averaged viscosity, viscosity fluctuations, and measures of turbulent anisotropy are presented. Gavrilov and Rudyak (2017) [41] went back and redid the same study. Still, they focused on the energy balance by offering the distributions of the tensor components of turbulent stress, shear stress, and turbulent kinetic energy balances. The adequate results from this investigation suggest that the fluid index decreases, the turbulent transfer of momentum and velocity fluctuations between the wall and the flow core decrease, while the turbulent energy flowing to the wall increases. Furthermore, the velocity of the power-law fluid shows an increase in the radial direction, resulting in the enhancement of apparent viscosity. The turbulence anisotropy becomes more significant with the decreasing flow index (n).

As was already noted, reducing fluid index (n) leads to a significant decrease in the radial and tangential fluctuations of the velocity and a significant enhancement in the level of axial fluctuations. The growth of axial fluctuations leads to an increase in integral fluctuations and, consequently, in the kinetic energy of turbulent fluctuations.

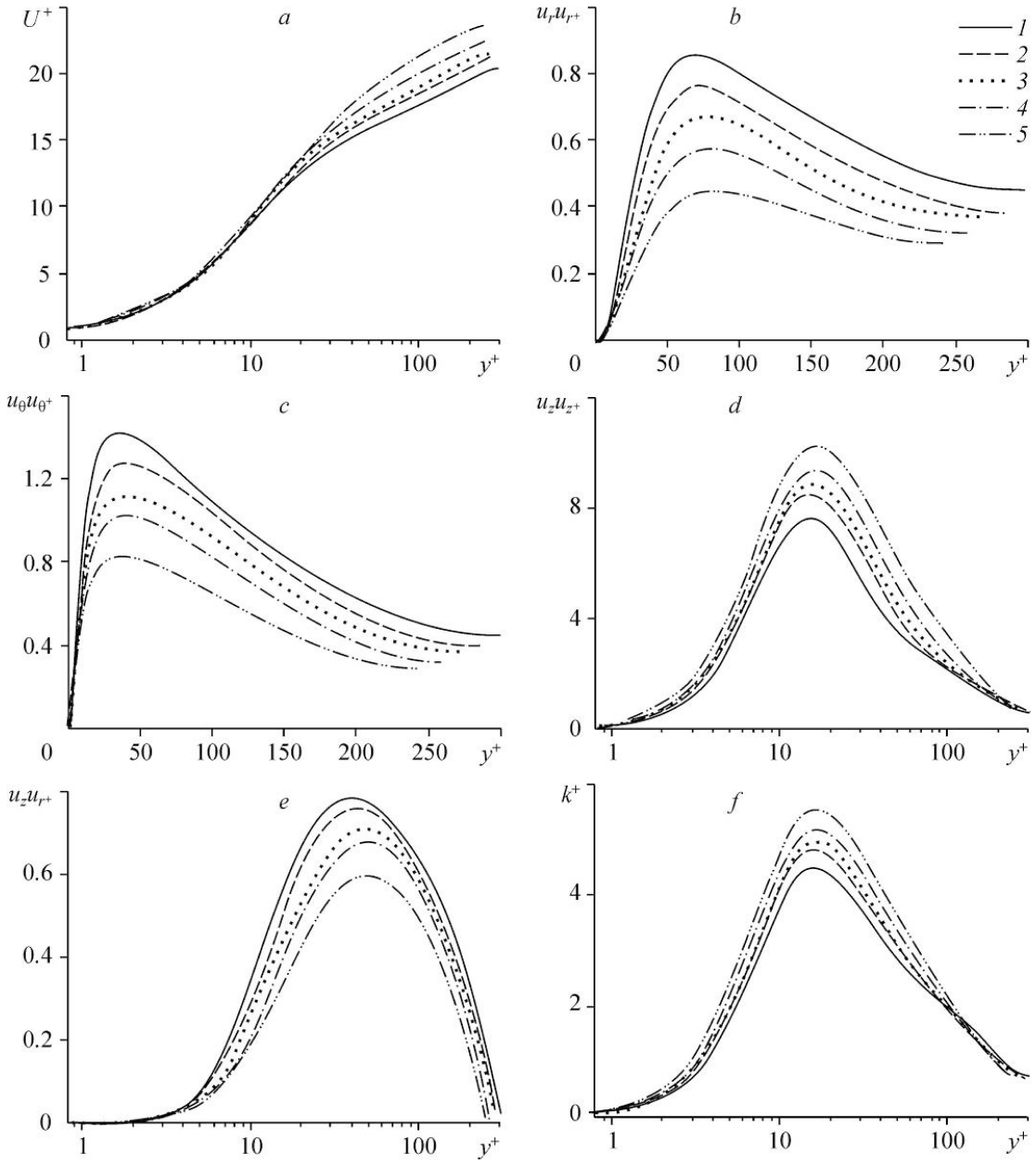

Figure II.2 – Results of Gavrilov and Rudyak (2016) [40] ; $n = 1(1), 0.8(2), 0.7(3), 0.6(4), 0.5(5)$[40]

One of the studies on the effect of yield stress using direct numerical simulation (DNS) performed by Singh et al. (2017) [42] on turbulent pipe flow for a generalised Newtonian fluid. The friction Reynolds number was fixed at 323 in a range of flow index (n) from 0.8 to 1. Here, simulations were carried out for two types of fluids, Bingham and Herschel–Bulkley, with yield stress varying between (0%) to (20%) of the mean wall shear stress and increasing in the mean axial velocity, especially in the log region resulting in a decrease of the flow index and even a reduction in the shear stress tensor. Moreover, the apparent viscosity of shear-thickening fluids is smaller than shear-thinning fluids. The viscosity increases when approaching the core region of the pipe. Thus, Ostwald de Waele fluids become more rigid.

New research and studies were carried out by Zheng et al. (2019) [43] to develop computational methods and DNS code better. According to Zheng et al. (2019) [43], the previous studies of shear-thinning fluids mainly use purpose built codes and simple geometries. However, the geometries are more complex in the practical domain, and more flexible computational methods are required. Thus, a fully developed turbulent pipe flow of shear-thinning fluids was undertaken using direct numerical simulation to validate and verify the efficiency of the Open FOAM library is assessed against a validated high-order spectral element-Fourier DNS code – Semtex. The emerging results of this investigation demonstrate that the predicted velocity and viscosity profiles are well resolved and predicted, while there is a notable difference in turbulence statistics. As it shall sees, it is important to note that the different Reynolds turbulence intensities and stress profiles peak at (16%) and (10%), corresponding to the Reynolds numbers 5000 and 7500, respectively. Ultimately, these simulation results agree with the experiment data and demonstrate that Open FOAM is a viable option for such flows that might be expected in practice.

It was clear from the above investigations that the study of the turbulent pipe flow of non-Newtonian fluid was very few using large eddy simulations (LES). Gnambode et al. (2015) [47] implemented in the laboratory code, a large eddy simulation (LES) with an extended Smagorinsky model to perform a numerical study of the turbulent behaviour of power-law fluids. This study was one of the first investigations to examine in detail the turbulent flow of shear-thinning and shear-thickening fluids through a pipe at a variable behaviour index (n) $(0.5 \leq n \leq 1.4)$, Prandtl number $(1 \leq Pr \leq 100)$ and Reynolds numbers (4000, 8000 and 12000) and their effects on the rheological and turbulence characteristics. The results show that the decrease in the flow index result a rise in axial and mean velocity profiles in the log region, due to the higher viscosity in the pipe centre. Indeed, the same remark is noted for the apparent viscosity in this region, and the importance of the increase of the flow behaviour index. On the contrary, the apparent viscosity of the power-law fluids decreases along the centre region. Moreover, the reduction in the friction factor with the flow behaviour index leads a noticeable enhancement in Reynolds number for both shear-thinning and shear-thickening fluids.

More recently, Abdi and co-workers offered extensive investigations of the turbulent flow of non-Newtonian fluids using the LES approach ; these investigations provided an important opportunity to advance the understanding of the rheological behaviour heat transfer mechanism on the non-Newtonian. Abdi and co-workers employed the LES with an extended Smagorinsky model to investigate numerically the fully developed turbulent flow of Ostwald de Waele fluid

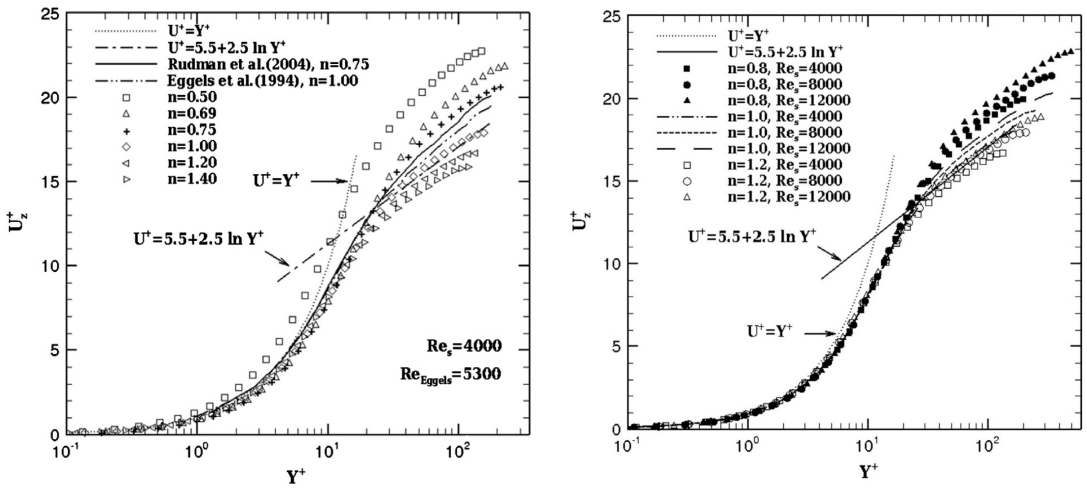

Figure II.3 – Axial velocity profiles of Gnambode et al. (2015) [47].

through a straight cylindrical pipe with a length of the domain of $20R$ in the axial direction and a numerical resolution of 65^3 gridpoints in the axial, radial, and circumferential directions. Their predicted findings results were in excellent agreement with those of experimental and DNS data available in the literature. The mathematical model was implemented in the laboratory code, and the computational procedure was based on a finite difference scheme and second-order accuracy in space and time. The time-advancement employs a fractional-step method. A third-order Runge-Kutta explicit scheme and a Crank-Nicholson implicit scheme were used to evaluate the convective and diffusive terms. Overall, these papers aimed to ascertain the accuracy and reliability of the large eddy simulation laboratory code predicted results and assess the LES approach's capability for resolving and predicting the scales motions of the turbulence. In addition, these papers evaluated the extent to which the LES with the extended Smagorinsky model can characterise the scales motions, especially in the wall vicinity.

Abdi et al. (2019) [50] provided the first extensive investigation of the heat transfer of a shear-thinning using LES with an extended Smagorinsky model. They numerically investigated the forced convection fully developed turbulent flow of the pseudoplastic $(n = 0.75)$ and Newtonian fluids through a heated axially rotating pipe over a rotation rate range $(0 \leq N \leq 3)$ at simulation Reynolds and Prandtl numbers 4000 and 1, respectively. This study aimed to shed more light on the laminarisation phenomena and examine the effects of the centrifugal force induced by the swirl driven by the rotating pipe wall on rheological behaviour, thermally characteristics, and turbulence characteristics, particularly in the vicinity of the wall. Abdi et al. (2019) [50] found that the centrifugal force induced by the rotating pipe wall significantly enhanced the mean axial velocity profile (towards the pipe centre) as the pipe rotated due to the diminution

of the apparent fluid viscosity in the core region. Moreover, the rotating pipe wall led to a noticeable reduction of the temperature profile along the radial coordinates, and this trend was more pronounced as the rotation rate increased. The predicted results also revealed that when the pipe rotated, the RMS of temperature fluctuations and axial turbulent heat flux profiles exhibited a marked reduction : they became less intense and flattened further away from the wall vicinity. This indicates that the increased rotation rate reduced the transfer mechanism of the temperature fluctuations between the flow layers. The results also showed that the Nusselt number was reduced when the rotation rate varied from 0 to 0.5, while it was enhanced with increasing (N) for $N \geq 1$.

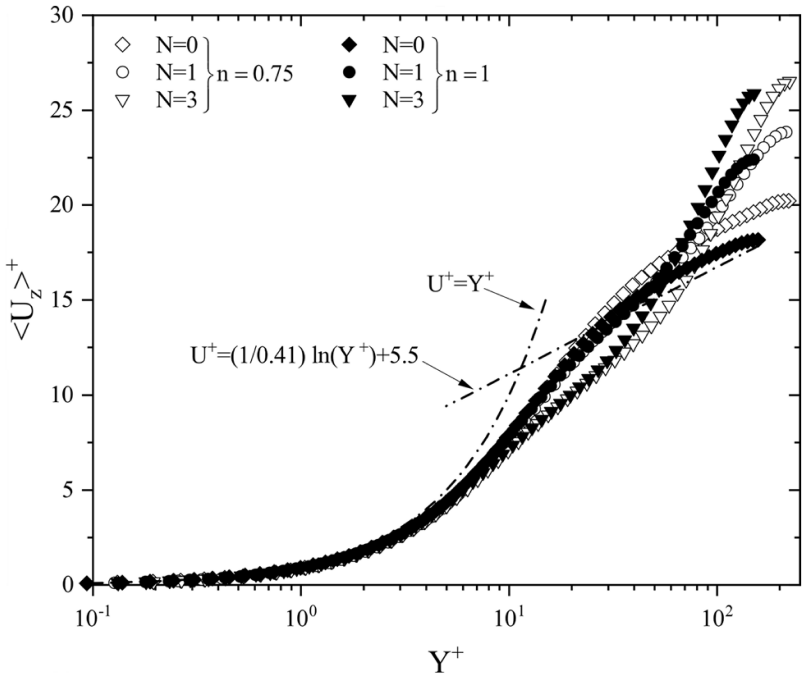

Figure II.4 – Turbulent axial velocity profile [50].

In 2022 Abdi and co-workers performed extensive investigations of pseudoplastic and dilatant fluids through a heat stationary cylindrical pipe to provide more details about the rheological and hydrodynamic behaviour in addition to the turbulence feature via analysing and discussing the effects of the flow behaviour index and Reynolds number on the mean flow, thermal quantities, and statistical turbulence quantities, especially in the vicinity of the wall.

Abdi et al. (2022) [51] and [52] performed a numerical analysis of the fully developed turbulent flow of pseudoplastic and dilatant fluids in an isothermal stationary pipe using a large eddy simulation, and a conventional dynamic model was presented in this work over a wide range of

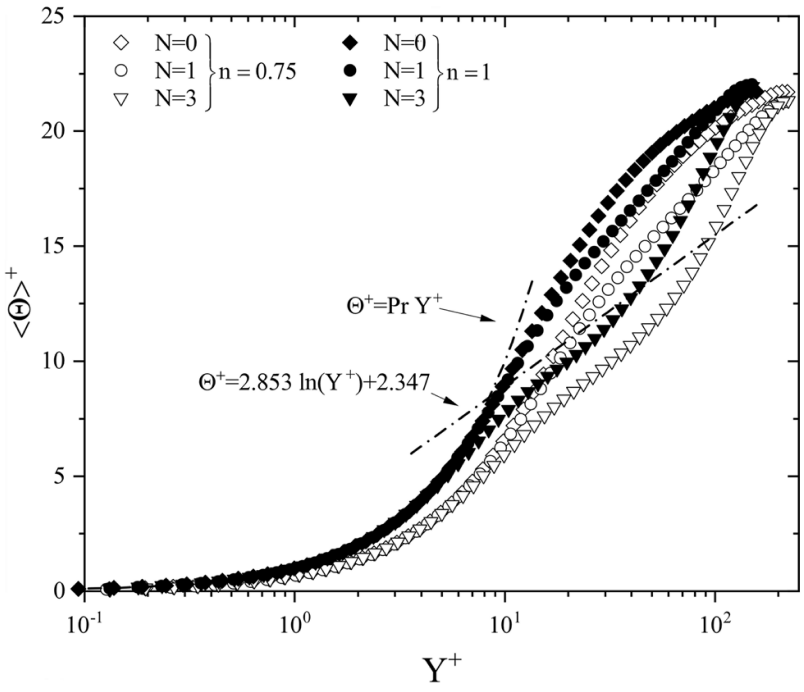

Figure II.5 – Mean temperature profile [50].

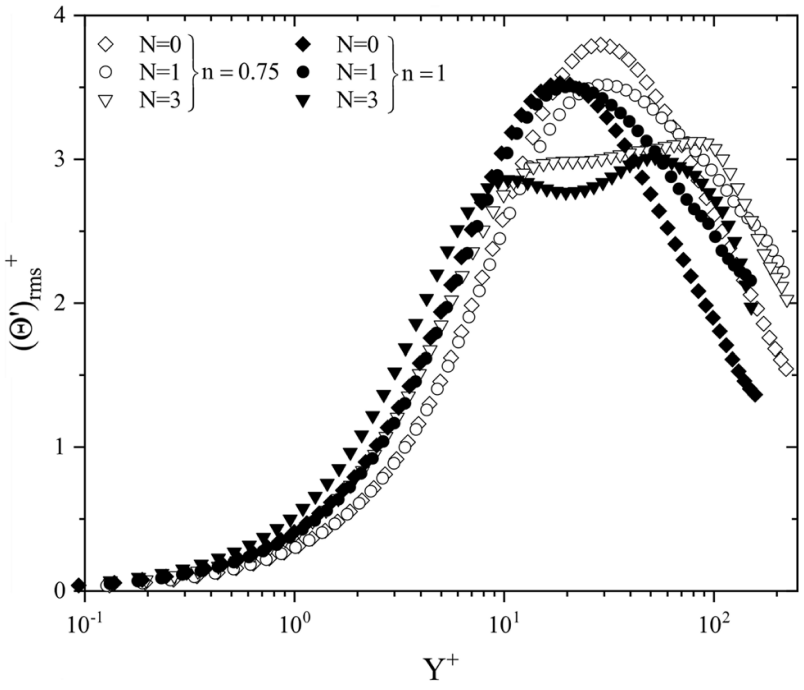

Figure II.6 – RMS of temperature fluctuations [50].

flow behaviour indexes 0.75, 0.8, 1, 1.2, 1.4, and 1.6 at a simulation Reynolds number of 12000.

Abdi et al. (2022) [53] and [54] carried out a *LES* investigation pseudoplastic and dilatant fluids for three simulations of Reynolds values ($Re_s = 4000, 8000$ and 12000). The flow behaviour indices used in this research primarily examined pseudoplastic and dilatant fluids were

0.75, 1, and 1.4, respectively.

More recently, Abdi et al. (2023) [55] employed the *LES* approach with an extended Smagorinsky model to investigate numerically the fully developed turbulent flow of pseudoplastic fluid with a flow behaviour index of 0.75 through an isothermal axially rotating cylinder at simulation Reynolds number of 4000 and over a rotation rate range of $(0 \leq N \leq 3)$. This investigation aimed to assess the influence of the centrifugal force induced by the swirl on the mean flow quantities, turbulent statistics, and instantaneous turbulence structure to describe the rheological behaviour and the turbulence features. Abdi et al. (2023) [55] found that the centrifugal force induced by the swirl flow induced a marked enhancement in the shear rate of the pseudoplastic fluid far away from the vicinity of the pipe wall, resulting in a noticeable reduction in the apparent viscosity of the shear-thinning fluid in the logarithmic region, where this trend was more prominent as the rotation rate increase.

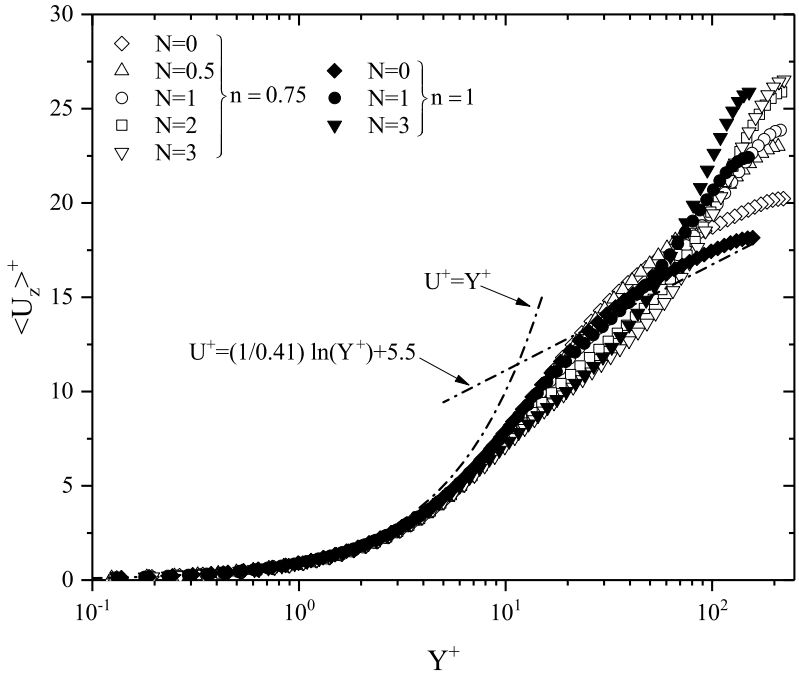

Figure II.7 – Behaviour of mean dimensionless shear rate [55].

In other words, the pseudoplastic fluid behaved like a liquid approaching the pipe centre as the pipe wall rotated. It should be noted that the variation in the apparent viscosity led to a redistribution of the axial velocity profile along the pipe radius. The decreased apparent viscosity of the pseudoplastic fluid in the logarithmic layer with an increasing rotating rate results in a gradual enhancement in the axial velocity profile far away from the pipe wall towards the core

region as the pipe wall rotated, as pointed out by Abdi et al. (2019) [50].

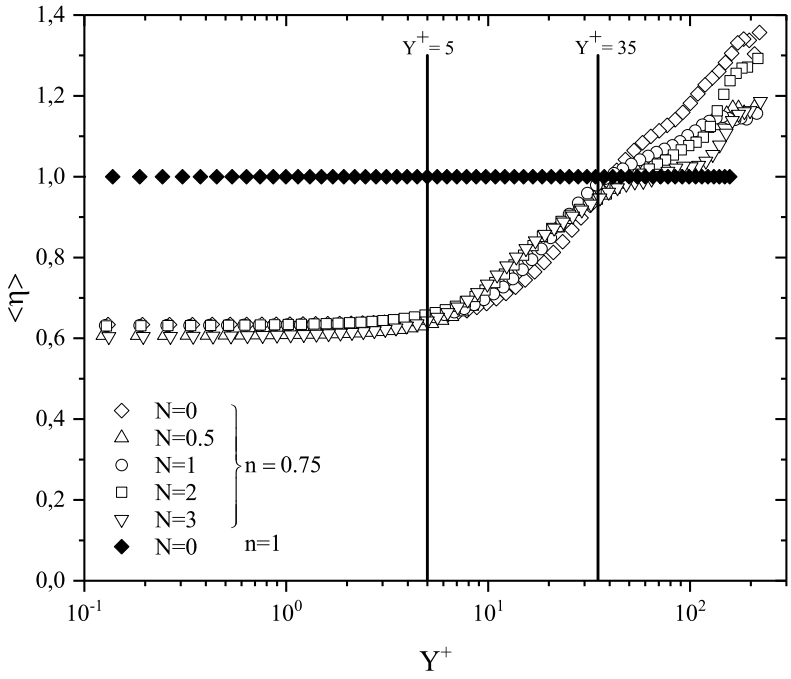

Figure II.8 – Apparent viscosity behaviour [55].

Abdi et al. (2023) [55] found that the swirl driven by the rotating pipe wall resulted in an apparent attenuation in the generation and the transport mechanism of turbulence intensities of the axial velocity fluctuation from the wall vicinity towards the core region for the pseudoplastic fluid. This reduction in the RMS of the axial velocity fluctuations led to a decrease in the kinetic energy of turbulent fluctuations and, consequently, in the turbulent Reynolds shear stress of the axial-radial velocity fluctuations as the pipe wall rotates. In turn, the turbulence intensities of the radial and tangential velocity fluctuations exhibited a pronounced enhancement when the pipe wall was rotating. This trend was more evident as the rotation rate increased. In other words, the centrifugal force induced by the swirl flow resulted in a noticeable amelioration in the transport mechanism of the energy fluctuations from the axial one to the other as the pipe wall rotated. Furthermore, the friction factor for the pseudoplastic fluid exhibited a reduction when the rotation rate varied from 0 to 0.5 and enhancement when $N \geq 1$ with an increasing rotation rate.

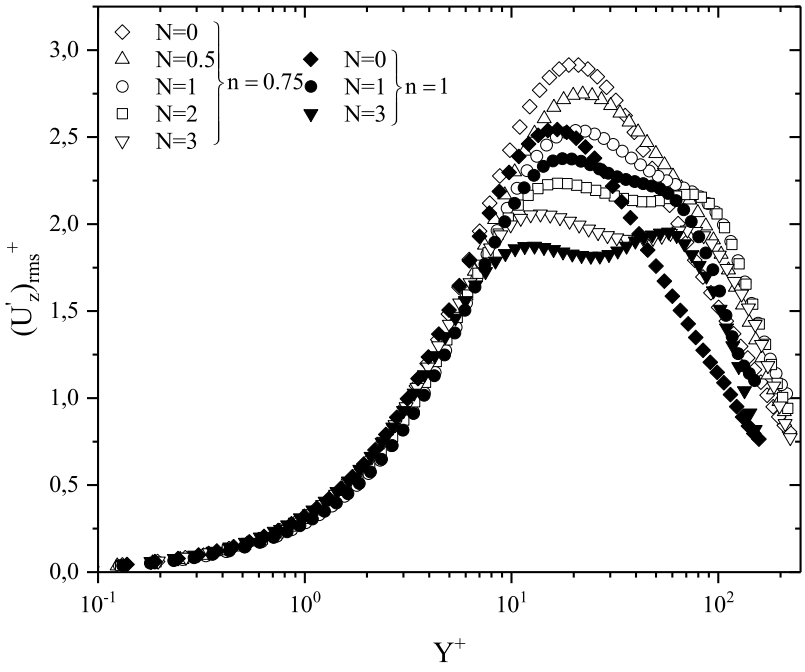

Figure II.9 – RMS of axial velocity fluctuations [55].

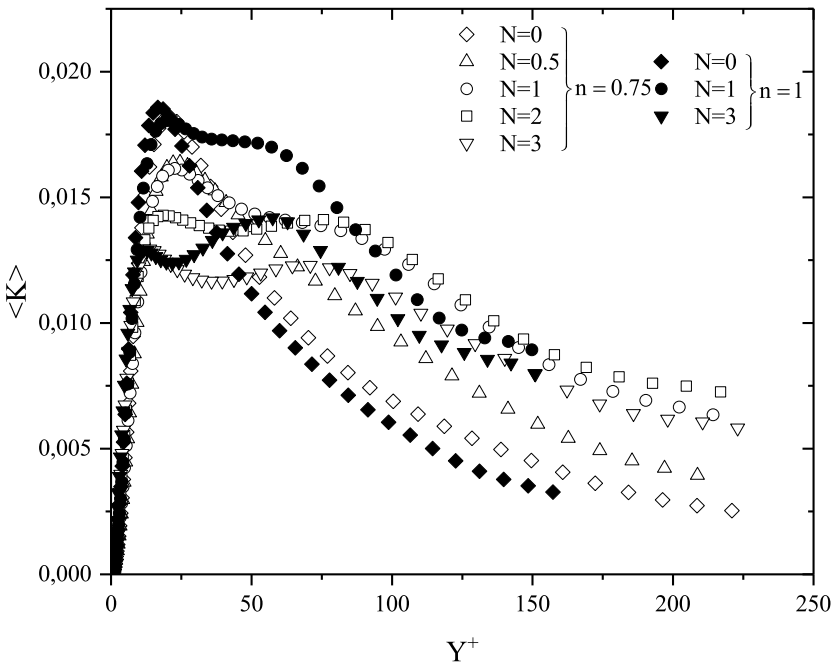

Figure II.10 – Distribution of the turbulent kinetic energy [55].

It is clear from the above literature survey done that there is very few research and investigations employing *LES* for non-Newtonian fluids despite their vital role. The convective heat transfer in swirling flows is often encountered in chemical and mechanical mixing and separation devices, electrical and turbo-machinery, combustion chambers, pollution control devices, swirl nozzles, rocketry, and fusion reactors. The flow through rotating pipes is of great practical interest because of the various industrial applications and is often encountered in various furnaces and combustors, as well as in rotating machinery. Among all these studies there is no work employing the characterisation of the turbulent flow of non-Newtonian fluids inside the circular rotating pipe, especially on shear-thickening fluid.

The current study is based on rheological, hydrodynamic behaviour and thermally developing turbulent forced convection of non-Newtonian fluid in an axially rotating pipe. This data deals with direct numerical simulation and direct numerical simulation large eddy simulation using an extended Smagorinsky model. The aim of the current research is to investigate the effects of the turbulent and hydrodynamic properties, and the effect of stabilisation or destabilisation force from the swirl produced by a rotating pipe wall.

CHAPTER III

TURBULENT FLOW AND NUMERICAL PROCEDURES

TURBULENT FLOW AND NUMERICAL MODELLING

III

Why Turbulence ?

It may seem somewhat peculiar to begin the introduction of a thesis on turbulence with the question "Why turbulence ?". A specialist on turbulence theory will be surprised by this question and wonder "Why turbulence" again ? We, at least I, know everything about it, Others, familiar with fluid dynamics in general, might be interested to know why it considers turbulence in particular and not one of the other interesting aspects of fluid dynamics. Finally, any layman on the area of fluid dynamics will return the appropriate question "What is turbulence ?" . These three questioners, with their totally different questions, have one thing in common. When reading and learning about turbulence, they all will find out that turbulence is one of the most interesting areas of fluid dynamics and that far from everything is known about it (this makes working on turbulence even more challenging) [56].

III.1 Turbulence phenomenon

III.1.1 Understanding Turbulence

Turbulent flows can be commonly observed in numerous natural and industrial cases. However, a precise definition is somewhat difficult and all that can be done is a listing of some of its characteristics [57]. The most significant characteristic of all turbulent flows is the associated irregularity or randomness. Consequently, a deterministic approach to the study of turbulence is impossible, and statistical methods have to be relied on [57]. From the point of view of industrial applications, turbulent flows are immensely important in many diverse fields. Consequently, it is important to understand the phenomenon of turbulence and correctly predict its effects. In engineering applications turbulent flows are prevalent, but less easily seen. In the processing of liquids or gases with pumps, compressors, pipe lines, etc., the flows are generally turbulent. Similarly, the flows around vehicles, airplanes, automobiles, ships, and submarines are turbulent. The mixing of fuel and air in engines, boilers, and furnaces, and the mixing of the reactants

in chemical reactors take place in turbulent flows. For engineering applications, the diffusivity of turbulence is an important factor. The diffusivity leads to rapid mixing, thereby increasing transfer rates of momentum, heat and mass through the flow domain. For example, turbulence can delay boundary layer separation on aerofoils at large angles of attack, increase heat transfer rates, provide resistance to flow in ducts, increase momentum transfer between currents, and so on [58].

Turbulence, the pseudo-random and apparently unpredictable state of a fluid, is one of the most challenging problems in fluid dynamics. Turbulent flows show a marked increase in mixing and friction ; predicting these phenomena is important in practical engineering applications. Consequently, numerous scientists have invested much effort in observing, describing, and understanding turbulent flows. One of the first attempts at quantifying turbulence was made by Reynolds, who showed that the flow regime changes from its orderly laminar state to a turbulent one when a critical parameter (Reynolds' number) is exceeded. Another important discovery was that turbulent flows incorporate a hierarchy of eddies or whirls, which range from large scales to very small in size. Energy is transferred between these scales, generally from the larger to the smaller, until the smallest scales are finally dissipated into heat by molecular viscosity. The Russian scientist Kolmogorov formulated this energy cascade theory into physical laws for the various scales present in a turbulent flow [58].

An important characteristic of turbulence is its ability to transport and mix fluid much more effectively than a comparable laminar flow. This is well demonstrated by an experiment first reported by Osborne Reynolds (1883). Dye is steadily injected into the centreline of a long pipe flowing with water. As Reynolds (1894) later established, this flow is characterised by a single non-dimensional parameter known as the Reynolds number. In general, it is defined by $Re = ul/\nu$ where u and l are characteristic velocity and length scales of the flow and is the kinematic viscosity of the fluid. For pipe flow, u and l are taken to be the area-averaged axial velocity and the pipe diameter, respectively. In Reynolds pipe-flow experiment, if Re is less than about 2300, the flow is laminar the fluid velocity does not change with time, and all streamlines are parallel to the axis of the pipe. In this (laminar) case, the dye injected on the centreline forms a long streak that increases in diameter only slightly with downstream distance. If, on the other hand, Re exceeds about 4000, then the flow is turbulent. Close to the injector, the dye streak is jiggled about by the turbulent motion ; it becomes progressively less distinct with downstream distance, and eventually mixing with the surrounding water reduces the peak dye concentration to the extent that it is no longer visible. The effectiveness

of turbulence for transporting and mixing fluids is of prime importance in many applications. When different fluid streams are brought together to mix, it is generally desirable for this mixing to take place as rapidly as possible. This is certainly the case for pollutant streams released into the atmosphere or bodies of water, and for mixing different reactants in combustion devices and chemical reactors. Turbulence is also effective at "mixing" the momentum of the fluid. Consequently, on aircraft's wings and ships hulls the wall shear stress (and hence the drag) is much larger than it would be if the flow were laminar. Similarly, compared with laminar flow, heat and mass transfer rates at solid–fluid and liquid–gas interfaces are much enhanced in turbulent flows. The major motivation for the study of turbulent flows is the combination of the three preceding observations : the vast majority of flows are turbulent ; the transport and mixing of matter, momentum, and heat in flows is of great practical importance ; and turbulence greatly enhances the rates of these processes [59].

III.1.2 Turbulence Structures

As a first step in studying turbulent flows, a distinction must be made between small scale turbulence and large scale motion. At high Reynolds numbers, there exists a separation of length-scales wherein the geometry of the flow domain strongly influences large scale motion while the small scale motion is almost entirely independent of the geometry. This range of length scales is limited at the large scale end by the overall dimensions of the flow field and at the small scale end by the diffusive action of molecular viscosity. Turbulent transport and mixing are controlled by large scale motion or large eddies, which are of a size comparable to the overall dimensions of the flow field. Consequently, the relevant length scale for the analysis of the interaction of the turbulence and the mean flow is the flow dimension. The small length scales are limited at the smallest end by the diffusive action of the molecular viscosity. These small scales become progressively smaller with increasing Reynolds numbers [60].

The starting point is the Navier–Stokes model for a Newtonian incompressible fluid with dynamic viscosity μ, in the absence of body forces :

$$\nabla . u = 0 \tag{III.1}$$

$$\rho(\frac{\partial u}{\partial t} + u.\nabla u) = -\nabla P + \mu \nabla^2 u \tag{III.2}$$

where u denotes the velocity field, ρ the density and P the pressure field.

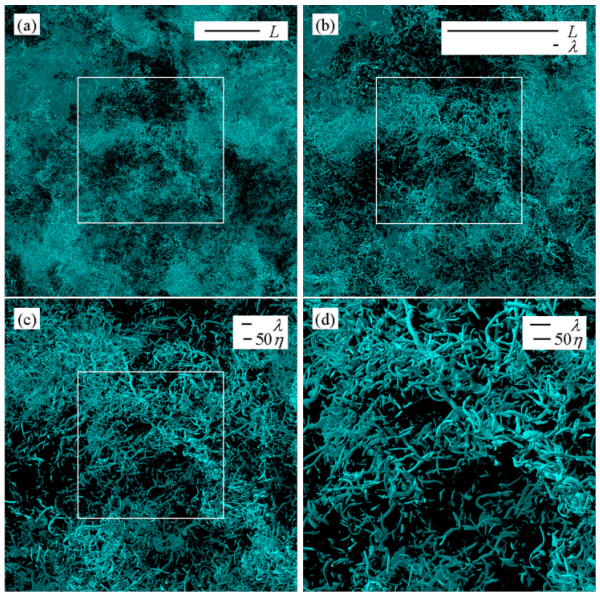

Figure III.1 – Instantaneous vorticity contours in isotropic turbulence at $Re_\lambda = 732$ (DNS in a periodic cube on a 4096^3 gridpoints) [61].

Note also that it must add initial and boundary conditions to get a well-positioned problem. The non-linear term appearing in the left-hand side (LHS) of Equation III.1 leads to most of the complex and rich phenomena of fluid mechanics. In particular, this quadratic term is the reason why fluids become turbulent. When this term gets much larger than the diffusive term, the flow becomes unstable, and large flow structures break up in smaller and smaller eddies until these are diffused into heat by viscous effects. This important process is called the Energy Cascade. Note that two-dimensional turbulence is not considered. It is now worth looking at the energy relation that occurs in turbulent flows of an incompressible fluid. By taking the product of Equation III.3 with u (by noting $u^2 = u.u$) and after some algebraic manipulations, it gets :

$$\frac{\partial(u^2/2)}{\partial t} = \underbrace{-\nabla.[(\frac{u^2}{2})u]}_{\text{(I) advection}} \quad \underbrace{-\nabla.[(\frac{P}{\rho})u]}_{\text{(II) work by pressure forcecs}} + \underbrace{\nabla.[(\frac{1}{\rho})u.\tau_v]}_{\text{(III) work by viscous stresses}} - \underbrace{2\nu S:S}_{\text{(IV)}\geq 0} \tag{III.3}$$

The LHS represents the local change of kinetic energy per unit of mass and time. The term $(I)+(II)$ may be interpreted either as the work due to the total pressure $P+\frac{1}{2}\rho u^2$ or as the change in transport of the total energy $E = \frac{P}{\rho} + \frac{1}{2}u^2$ (per unit mass) through advection by the velocity. Term (III) represents the work done per unit mass and time by the viscous shear stresses of the turbulent motion. Furthermore, this equation tells us that the last term (IV) on the RHS represents the rate of dissipation of mechanical energy per unit mass to heat :

$$\varepsilon = 2\nu S:S \tag{III.4}$$

By noting $\omega = \nabla \times u$, the vorticity field, ε can also be expressed as :

$$\varepsilon = \nu\omega^2 \tag{III.5}$$

$\Omega = \omega^2/2$ is the enstrophy.

Note that Equation III.4 and III.5 indicate firstly that turbulence produces gradients and vorticity and secondly that the rate at which energy is dissipated is particularly pronounced in regions where the instantaneous velocity gradients are large in the smallest eddies [61].

III.1.3 Characteristics of Turbulence

It regards as turbulence is therefore better to express as a list of properties and attributes that can help us to identify turbulent flows :

1. **Randomness** : Turbulent flow is unpredictable in the sense that small random perturbations during a particular period of time are amplified to that level, and after a certain period of time deterministic prediction of further development becomes impossible. This fact could seem to conflict with the fact that turbulent flow is describe in thorough detail by Navier-Stokes equations, which of course are of a deterministic character. The effect of their non-linear nature can under certain circumstances cause a situation in which perturbations of a certain type are very strongly amplified in time. Such perturbations could be related to the lack of precision of the assignment of initial conditions or related to Brownian motion of fluid particles, which is not modelled by the equations, because the fluid in this case is considered a continuum. The consequence of this situation is the unpredictable behaviour of a specific turbulent flow. Of course, in a statistical sense, the development of turbulence can be considered predictable, since it involves deterministic chaos.

2. **Diffusivity** : Mixing of transported scalar quantities occurs relatively more quickly than during molecular diffusion. This characteristic obviously has important practical consequences, and an increase in mixing of fluids characterizes turbulence. The intensity of this mixing can be several orders of magnitude greater than mixing occurring as a result of molecular diffusion. It can estimate that the coefficient of molecular diffusion of fluids is in technical applications at least two orders smaller than the typical value of the coefficient of turbulent diffusion, and in the case of planetary flows (atmospheric phenomena or ocean streams), this difference can be significantly greater typically up to 7 orders greater.

3. **Vorticity** : Turbulent flows are characterised by high local values of vorticity related to the presence of vortex structures. The field of vorticity is generally non-homogeneous and changes dynamically in time. Vortex structures tend to be referred to as coherent vortices or more generally coherent structures.

4. **Scale spectrum** : Vortex structures, which occur spontaneously in a turbulent flow field, are characterised by a wide scale of length measuring units. Their size is limited from the top by the dimensions of the shear areas in which they occurred and from the bottom by the size of vortices subject to dissipation in direct connection with the viscosity of the fluid. Thus, the size of the structure is characterised by a dense spectrum typical for fractals. Related to this is the fact that the turbulent flow field can be characterised as a dynamical system with a "very high" number of degrees of freedom.

5. **3D structure** : Vortex structures occur in the space of a turbulent flow field in random locations and with random orientation. The $3D$ structure of the vector field of velocity fluctuations originates from this situation. During certain boundary conditions, structures greater than the certain limit size can be spatially arranged ; for example, they can have a planar character. This relates, for example, to flows in thin layers, where the dimensions of the area enable the occurrence of vortices of larger scales than the thickness of the layer only with vorticity oriented across the layer and not in parallel with it.

6. **Dissipation** : Turbulence is a dissipative process, which means that the kinetic energy of the motion of a fluid is dissipated at the level of small vortices and changes to heat. Therefore, in order for turbulent flows to be conserved over the long term, it is necessary to supply energy to the system from the outside. This is done in the area of large scales ; energy is collected from the mainstream. The energy is then transferred towards smaller scales with the help of cascade transfer.

7. **non-linearity** : Turbulent flows are basically non-linear, and their occurrence is conditioned on the application of non-linearities when growth of small perturbations occurs. The development as well as the interaction of individual structures in the turbulent flow field can be described only with a non-linear mathematical model [62].

III.1.4 Isotropic and Homogeneous Turbulence

Isotropic homogeneous turbulence is perhaps the simplest turbulent flow, but is rarely encountered in real-life applications. Isotropic turbulence means that the flow is statistically invariant to the rotation of the coordinate system, while homogeneity means statistical invariance to the translation of the coordinate system. For modelling applications, isotropy is important as the high Reynolds number hypothesis states that fine scale motions are unaware of the nature of the mean flow and large scale turbulence, thus the fine scale structure in any kind of turbulent flow is similar to what is found in isotropic turbulence. In parallel shear flows, such as channel flow, the main source of anisotropy is shear stress. Near the walls, the Reynolds stresses, i.e. the velocity fluctuations, exhibit large anisotropy due to the presence of the wall.

A plane channel flow is homogeneous in streamwise and spanwise directions, in terms of statistics, the flow field has a one-dimensional solution. However, when obstacles such as roughness elements are introduced, the flow becomes inhomogeneous in the streamwise direction. Thus, statistical means depend on streamwise location, and the solution becomes two-dimensional [63].

III.1.5 Kelvin-Helmholtz instability

This is the simplest illustrated case of shear flow, in relation to which loss of stability can occur. Nonetheless, this type of instability very often occurs in practice, such as during the surrounding of wings, during tearing away of the boundary layer or in a layered atmosphere. It often occurs at the boundary of two fluids with different physical properties. The situation is illustrated schematically in Figure III.2. In the stream near the boundary of the occurring perturbation of pressure, overpressure $(+)$ and sub-pressure $(-)$, a deformation of the boundary occurs in the form of periodic vortex structures [62].

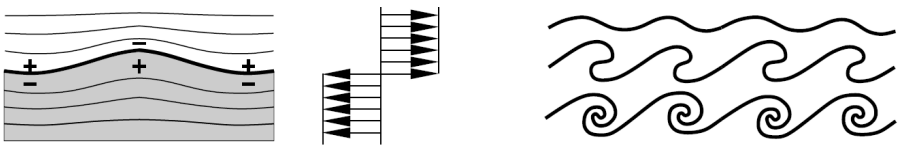

Figure III.2 – Scheme of Kelvin-Helmholtz instability origin [62].

Mathematically, the stability of this free shear layer can be solved in a manner similar to the case of the boundary layer. It can consider the initial velocity profile $u_0(x_2) = \tanh(x_2)$. Then the Orr-Sommerfeld equation can be applied, which leads to a stability diagram, which is schematically shown in Figure III.3. According to this diagram, the free shear layer is unstable

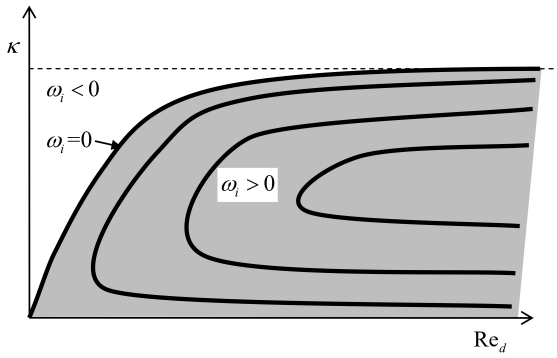

Figure III.3 – Stability diagram for a free shear layer [62].

for the random Reynolds number value $\mathrm{Re}_d = u_\infty \cdot d/v$ (d is the transverse dimension of the shear area). For growing Re_d the interval of unstable wave numbers k is increased until for sufficiently high Reynolds numbers it reaches its maximum asymptotic values.

The rate of the growth of perturbations ω_i in this case drops with the dropping Re_d. Unlike in the case of a boundary layer, in this case the upper branch of the neutral curve continues to rise. The friction in the free shear layer acts against the loss of stability, and due to perturbations with large wave numbers (small interruptions), the flow is stable. The actual experimentally obtained view of the free shear layer under the conditions of Kelvin-Helmholtz instability is shown in Figure III.4 [62].

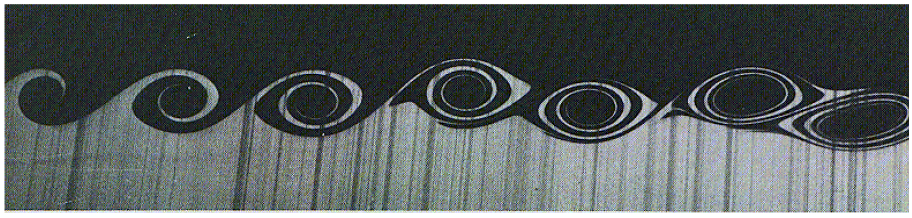

Figure III.4 – Kelvin-Helmholtz instability [62].

III.1.6 Energy Spectrum and Kolmogorov Cascade

The first concept in Richardson's view of the energy cascade is that the turbulence can be considered to be composed of eddies of different sizes. Eddies of size ℓ have a characteristic velocity $u(\ell)$ and time scale $\tau(\ell) \equiv \ell/u(\ell)$. An "eddy" eludes precise definition, but it is conceived to be a turbulent motion, localised within a region of size, that is at least moderately coherent over this region. The region occupied by a large eddy can also contain smaller eddies. The eddies in the largest size range are characterised by the length-scale ℓ_0 which is comparable to the flow scale L, and their characteristic velocity $u_0 \equiv u(\ell_0)$ is on the order of the r.m.s. $u' \equiv (\frac{2}{3}k)^{1/2}$ turbulence intensity which is comparable to U. The Reynolds number of these

eddies $Re_0 \equiv u_0 \ell_0 / \nu$ is therefore large (i.e., comparable to R_e), so the direct effects of viscosity are negligibly small [59].

Richardson's notion is that the large eddies are unstable and break up, transferring their energy to somewhat smaller eddies. These smaller eddies undergo a similar break-up process, and transfer their energy to yet smaller eddies. This energy cascade in which energy is transferred to successively smaller and smaller eddies continues until the Reynolds number $R_e(\ell) \equiv u(\ell)\,\ell/\nu$ is sufficiently small that the eddy motion is stable, and molecular viscosity is effective in dissipating the kinetic energy. Richardson (1922) succinctly summarised the matter thus :

. Big whorls have little whorls,

. Which feed on their velocity,

. And little whorls have lesser whorls,

. And so on to viscosity (in the molecular sense) [59].

Let us look more closely now at the flow of energy in developed isotropic flow. From an energy point of view, the flow of fluid represents an open system. Energy is carried into the system from the mainstream, and through the mechanism of loss of stability, large vortex structures are created. Their specific form can be attributed to the boundary conditions of the particular case. These vortices characterised by the scale and the corresponding wave number stand at the top of the energy cascade and represent the energy area of the wave numbers [62].

This is followed by the transfer of energy from large scales towards lower speeds ε inside the inertial sub-range. This is an energy cascade during which quick growth of the isotropy of the topology of vortex structures occurs. The mechanism for the transfer of energy is the stretching of vortices, as has already been stated. The process ends in the area of dissipation on the Kolmogorov scale. A diagram of the entire process is shown in Figure III.5. According to the original Kolmogorov theory, vortices at all levels of the cascade evenly fill the entire space.

However, situations can occur when boundary conditions disable the motion of fluid in one direction, and then the motion must be two-dimensional in particular scales. This involves, for example, motion in thin layers of fluid, and the case of the earth's atmosphere also resembles this situation. Flow under these conditions may be spatial only for certain scales, which are smaller than the thickness of the layer. The structures of larger scales can occur only in directions without limiting effects, and their vorticity is oriented in the direction of the smallest dimension

the thickness of the layer. The stretching of these vortices and generation of vorticity cannot occur, and the value of vorticity in these scales is conserved [62].

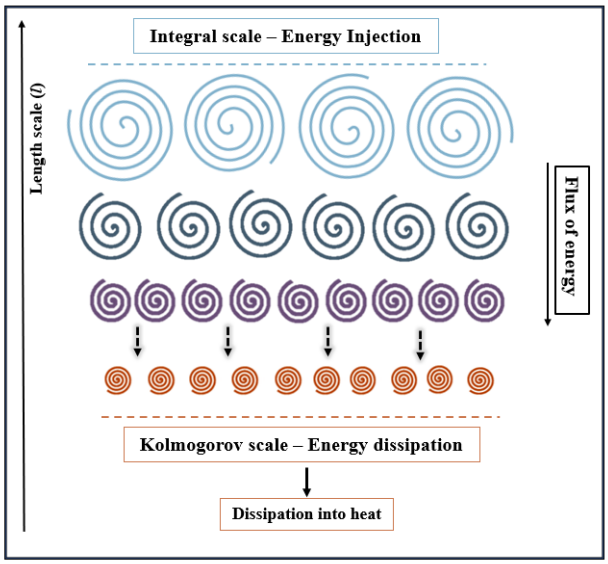

Figure III.5 – Energy Cascade.

The Kolmogorov theory

Several fundamental questions remain unanswered. What is the size of the smallest eddies that are responsible for dissipating the energy ?

As ℓ decreases, do the characteristic velocity and time-scales $u(\ell)$ and $\tau(\ell)$ increase, decrease, or remain the same ? (The assumed decrease of the Reynolds number $u(\ell)\ \ell\ /\nu$ with ℓ is not sufficient to determine these trends.)

These questions and more are answered by Kolmogorov's theory, which is stated in the form of three hypotheses. A consequence of the theory that Kolmogorov used to motivate the hypotheses is that both the velocity and time scales $u(\ell)$ and $\tau(\ell)$ decrease as ℓ decreases. The first hypothesis concerns the isotropy of small scale motions. In general, the large eddies are anisotropic and are affected by the boundary conditions of the flow. Kolmogorov argued that the directional biases of the large scales are lost in the chaotic scale-reduction process, by which energy is transferred to successively smaller and smaller eddies [59].

In 1941 Kolmogorov published a fundamental article that gives a mathematical apparatus to Richardson's idea of an energy cascade. Kolmogorov theory is based on three hypotheses : a hypothesis of local isotropy and the first and second similarity hypotheses. [62].

The hypothesis of local isotropy relates to small scale vortices. The largest vortices have approximately the dimension of shear area L , and the topology of these vortices is anisotropic, which can be attributed to specific boundary conditions (often very regular). The mean size of energy vortices is somewhat smaller, and it will refer to it as ℓ_0. The more or less chaotic process of the transfer of energy towards small scales is leading to a gradual increase in the isotropy of smaller scales. This is the basis for the Kolmogorov hypothesis of local isotropy : During sufficiently high Reynolds numbers, the motions of small scales $\ell << \ell_0$ are statistically isotropic [62].

The scale ℓ_{EI} is the boundary between small isotropic vortices and large non-isotropic vortices. For a better idea, let us consider $\ell_{EI} \approx 1/6\ \ell_0$. In the area of occurrence of small isotropic vortices $\ell_0 < \ell_{EI}$ two mechanisms of energy transfer dominate : transfers from large scales to small scales and viscous dissipation. The parameters that manage these processes are the rate of energy transfer from large scales to small $\Im_{EI}$ and kinematic viscosity ν. In a settled state, the rate of dissipation ε is in balance with the rate of production : $\varepsilon = \Im_{EI}$. It is apparent from this that the universal statistical state of small scales is determined by viscosity ν and the rate of the transfer of energy from the area of large scales $\Im_{EI}$.
This outcome formulates **Kolmogorov first similarity hypothesis**, which says that in a turbulent flow with a sufficiently high Reynolds number, the statistics of motions of small scales $(\ell < \ell_{EI})$ have a universal formulation and depend only on scale ℓ , viscosity ν and dissipation rate ε [62].

It is apparent from this that the energy spectrum $E(\kappa)$ has a universal formulation and depends only on ν and ε. If it uses these quantities for expressing the energy spectrum, then from the direct dimension analysis it is apparent that this dependency must have the formulation :

$$E(k) = (\varepsilon\nu^5)^{1/4}\varphi(k\eta) \tag{III.6}$$

Where $\varphi(k\eta)$ is the Kolmogorov spectrum function. However, for the purposes of the dimension analysis, it can also use ε and κ, and then it gets :

$$E(k) = \varepsilon^{2/3}k^{-5/3}\psi(k\eta) \tag{III.7}$$

Where $\psi(k\eta)$ is the compensated Kolmogorov spectrum function [62].

The area of scales $\ell < \ell_{EI}$ is usually referred to as the universal equilibrium range. In this area, the scales $\ell < u(\ell)$ are small in comparison with ℓ_0/u_0, and small vortices can quickly adapt in order to conserve dynamic equilibrium with the rate of energy transfer $\Im_{EI}$, which is determined by large vortices $u(\ell)$ is the typical value of fluctuations in velocity for perturbation of scales ℓ and u_0 and then for ℓ_0 [62].

From the dimensional analysis, it is possible to specify clearly (except the non-dimensional constant) the values of the resulting Kolmogorov scales. The relevant quantities are only the rate of dissipation $\varepsilon\,[m^2/s^3]$ and kinematic viscosity $\nu\,[m^2/s]$, length, velocity and time based Kolmogorov scale $\eta[m], u_\eta[m/s]$ and $\tau_\eta[s]$ and then it can define the following relationships [62] :

$$\eta \equiv (\nu^3/\varepsilon)^{1/4} \tag{III.8}$$

$$u_\eta \equiv (\varepsilon\nu)^{1/4} \tag{III.9}$$

$$\tau_\eta \equiv (\nu/\varepsilon)^{1/2} \tag{III.10}$$

Two identities are apparent from these definitions. First the Reynolds number based on Kolmogorov parameters is a unit figure : $\eta u_\eta/\nu = 1$. This fact is in accordance with the claim that the cascade transfer continues in the direction towards continuously smaller scales until the Reynolds number is so small that it enables dissipative processes. Also, from the relationships Equation III.8 and Equation III.10 it can express the rate of dissipation [62].

$$\varepsilon = \frac{\nu^3}{\eta^4} = \frac{{u_\eta}^4}{\nu} = \frac{\nu}{{\tau^2}_\eta} \tag{III.11}$$

From which specific characteristics for the velocity gradient of dissipating vortices are apparent :

$$(u_\eta/\eta) = 1/\tau_\eta \tag{III.12}$$

It can also introduce non-dimensional coordinates and non-dimensional speeds with the use of corresponding Kolmogorov scales, in which the following applies for non-dimensional coordinate y and velocity w :

$$y = x/\eta,\ \mathrm{w{=}u/u_\eta} \tag{III.13}$$

In the area of small scales, according to the hypothesis above all turbulent flow fields are statistically similar, and following the transformation with the help of Kolmogorov scales, they

are then identical in a statistical sense.

If it considers that $\varepsilon \sim {u_0}^3/\ell_0$ then it can express the relationship of the sizes of the smallest and largest scales in the particular turbulent flow

$$\frac{\eta}{\ell_0} \sim \mathrm{Re}^{-3/4}, \quad \frac{u_\eta}{u_0} \sim \mathrm{Re}^{-1/4}, \quad \frac{\tau_\eta}{\tau_0} \sim \mathrm{Re}^{-1/2} \tag{III.14}$$

Kolmogorov second similarity hypothesis states that in every turbulent flow during a very high Reynolds number approaching infinity, the motions of turbulent scales ℓ are such that $\ell \gg \ell \gg \eta$ applies, there is a universal formulation, and it is dependent only on the rate of dissipation ε and not on viscosity.

If it introduces the scale ℓ_{DI} (its size is approximately 60η) it is such that Kolmogorov second hypothesis applies in the extent $\ell_{DI} > \ell > \ell_{DI}$. Such defined scale divides the area of universal equilibrium into two sub-ranges : the inertial sub-range, where $\ell_{DI} > \ell > \ell_{DI}$ and the dissipation range, where $\ell_{DI} > \ell$. The dissipation range is the only range where there is a significant effect of viscosity, and only Kolmogorov first detailed hypothesis applies for it [62].

The last area remains, which is the area of the largest vortices and which is usually referred to as the energy containing range. The division into individual areas is labelled on Figure III.6, where the axis of scales is logarithmic [62].

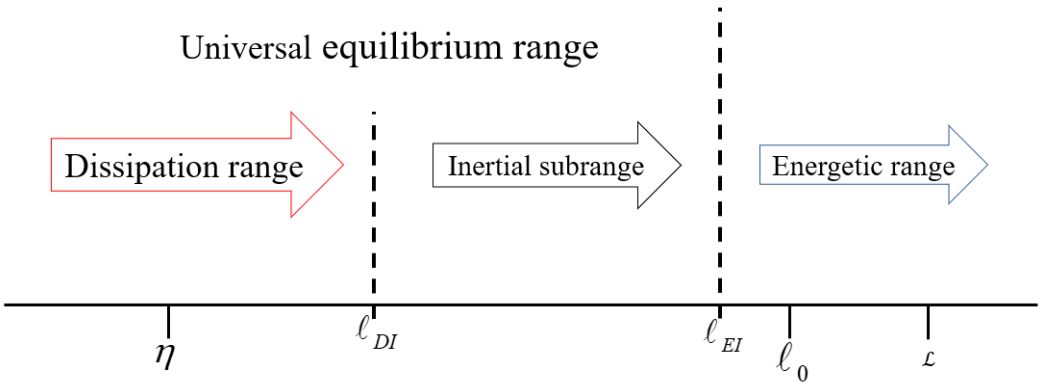

Figure III.6 – Scales of turbulence ranges after Kolmogorov.

In the inertial sub-range, the effect of the viscosity is insignificant, and the coefficient $k\eta \ll 1$ is insignificantly small. Therefore, in the inertial area, the compensated, Kolmogorov spectrum is defined Equation III.7 approximately by constant $\psi(k\eta) = C$, and the relationship can express the energy spectrum :

$$E(k) = C\varepsilon^{2/3}k^{-5/3} \tag{III.15}$$

Where κ is the wave number and C is the universal constant ($\approx$ 1.5) [62].

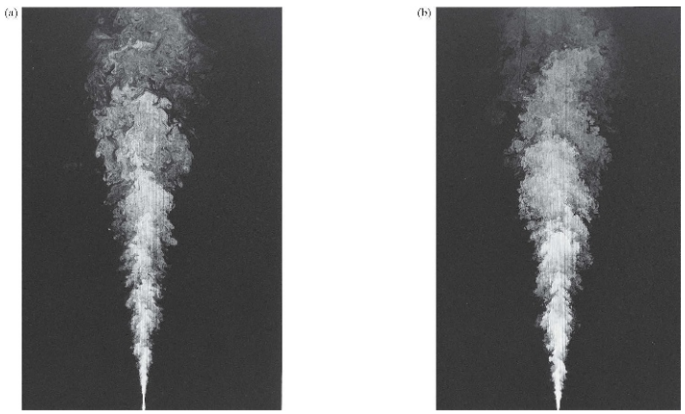

Figure III.7 – Planar images of concentration in a turbulent jet : (a) $Re = 5000$ and (b) $Re = 20000$. From Dahm and Dimotakis (1990) [59].

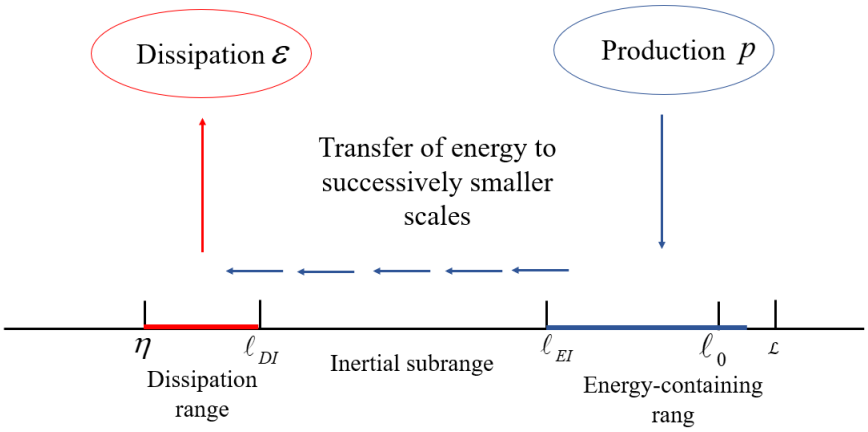

Figure III.8 – A schematic diagram of the energy cascade at very high Reynolds number.

III.2 Turbulence Modelling

The study of turbulent flows can be divided into three main categories : analytical theory, physical experiments and numerical simulations. The analytical approach to turbulence has faltered against the complexity of the problem that is stochastic and strongly non-linear in nature and is consequently of limited use as a general tool. Experimental fluid dynamic research has always been of great significance. It still remains the benchmark for the validation of new models and for the foreseeable future will continue to be of fundamental importance in the field. Also, the advent of new measuring techniques that allow single and multi-point sampling of flow characteristics, such as Laser-Doppler velocimeters and multiple wire anemometers, have

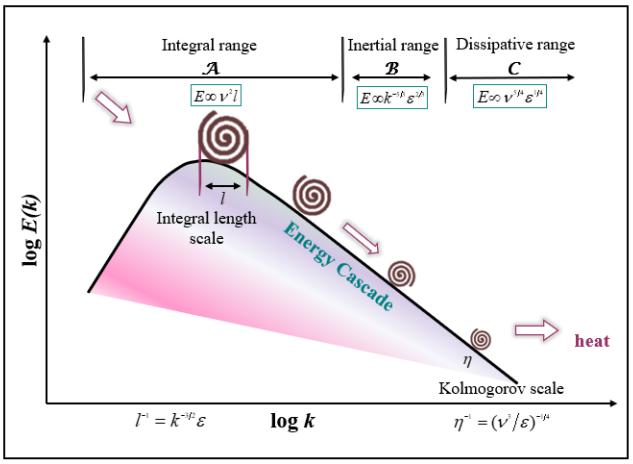

Figure III.9 – Schematic Representation of Turbulence Energy Spectrum.

significantly increased the utility and range of experimental measurements [58].

From the theory of dynamical systems, it is known that many connected systems can be modelled with a system of partial and differential equations, which must then be resolved numerically. Such dynamical systems theoretically have a never ending number of degrees of freedom, and for their resolution initial conditions are required that are characterised by a never ending number of conditions located in the particular space. The dynamic behaviour of spatially connected systems can be variable both in space and in time, as a result of which both regular and chaotic structures can occur [62]. Let us call turbulence numerical modelling any numerical approach allowing us to predict the evolution of instantaneous or mean quantities associated with turbulence and that can be applied to shear flows [64].

III.2.1 Scale Resolving Simulation (SRS)

III.2.1.1 Direct numerical simulations (DNS)

In 1922, the meteorologist Richardson proposed numerical schemes to solve the equations of fluid mechanics applied to the atmosphere in a deterministic fashion. This marked the beginning of direct numerical simulations of turbulence, which are deterministic time advancing numerical solutions of fluid mechanics equations with a proper set of initial and boundary conditions.

This is possible provided the two following conditions are fulfilled :

- The numerical schemes are accurate enough.
- All the scales of motion, from the largest to the smallest, are captured.

There is some evidence that small scale turbulence is not far from isotropy even if large scales are not, and thus λ may be evaluated even for anisotropic flows : Jimenez stresses that $R_\lambda \approx 3000$ in the boundary layer of a commercial aircraft, 10^4 in the atmospheric boundary layer, and higher values are present in astrophysics. It finds that this entails, respectively, using more than 10^{15} and 10^{18} points in computer simulations for the two cases. At present, to avoid excessive computing times on even the biggest machines, one has to restrict calculations to about (2×10^7) gridpoints, which are many orders of magnitude shy of these estimates. Even with the unprecedented improvement of scientific computers, it may take several decades (if it ever becomes possible) before DNS permits us to capture situations at Reynolds numbers comparable to those encountered in natural conditions. This demonstrates the immense interest in LES techniques [64].

Once discretised, the Navier-Stokes equations are integrated in time. Doing so without further approximations is called Direct Numerical Simulation (DNS). DNS is the most accurate and reliable fluid dynamics simulation tool available. However, to obtain an accurate solution using DNS requires that the mesh or cell size captures all relevant scales of motion in the problem. If the flow to be simulated is turbulent, then the mesh or cell size must be within one order of magnitude from the Kolmogorov length scale, the smallest length scale at which turbulence exists. Dominated by viscosity, these small scales are largely responsible for the dissipation of turbulent motion into heat. Capturing Kolmogorov scales implies solving the Navier-Stokes equations on many cells or a very fine mesh. The computational work required may take a prohibitively large amount of time even on the best available super computer [65].

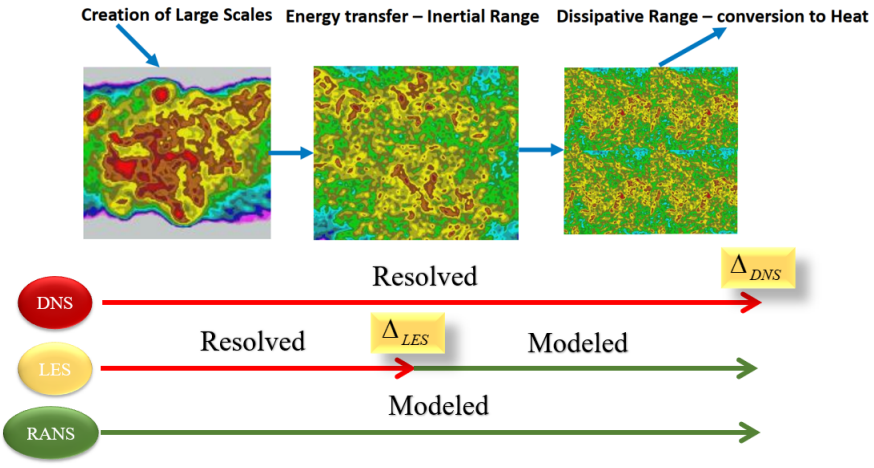

Figure III.10 – Dissipation of kinetic energy.

III.2.1.2 Large eddy simulation (LES)

Large eddy simulation (LES) of turbulent flows are extremely powerful techniques consisting in the elimination of scales smaller than some scale Δx by a proper low-pass filtering to enable suitable evolution equations for the large scales to be written. The latter maintains an intense spatio-temporal variability. Large eddy simulation (LES) poses a very difficult theoretical problem of sub-grid scale modelling, that is, how to account for small scale dynamics in large scale motion equations. LES is an invaluable tool for deciphering the vortical structure of turbulence since it allows us to capture the formation and ulterior evolution of coherent vortices and structures deterministically. It also permits the prediction of numerous statistics associated with turbulence and induced mixing. LES applies to extremely general turbulent flows (isotropic, free-shear, wall-bounded, separated, rotating, stratified, compressible, chemically reacting, multiphase, magnetohydrodynamic, ect). LES has contributed to a blooming industrial development in the aerodynamics of cars, trains, and planes, propulsion,turbo-machinery, thermal hydraulics, acoustics, and combustion . An important application lies in the possibility of simulating systems that allow turbulence control, which will be a major source of energy savings in the future. LES also has many applications in meteorology at various scales (small scales in the turbulent boundary layer, mesoscales, and synoptic planetary scales). Use of LES will soon enable us to predict the transport and mixing of pollution. LES is used in the ocean for understanding mixing due to vertical convection and stratification and also for understanding horizontal mesoscale eddies. LES should be very useful for understanding the generation of Earth's magnetic field in the turbulent outer mantle and as a tool for studying planetary and stellar dynamics. It is clear that the study of large eddy simulations of turbulence has become a discipline by itself [64].

The history of LES began in the $1960s$ with the introduction of the famous Smagorinsky's eddy viscosity proposed in 1963. Smagorinsky, a meteorologist like Richardson, did work in the famous mathematical modelling group founded by Von Neuman. In fact, Smagorinsky wanted to represent the effects on a quasi-two-dimensional, large scale atmospheric or oceanic flow of three-dimensional sub-grid scale turbulence following a Kolmogorov direct cascade. It is interesting to remark that Smagorinsky's model was a total failure as far as atmospheric and oceanic dynamics are concerned because it overly dissipates the large scales. Therefore, large scale atmospheric or oceanic numerical modelers turned toward hyper-viscous sub-grid models. Nonetheless, Smagorinsky's model was extensively used by people interested in industrial applications (and also small or mesoscale meteorology), which shows that the research outcome

may be as unpredictable as turbulence. One should mention the important contribution of Lilly, another meteorologist and Smagorinsky's collaborator, who calculated the value of the Smagorinsky constant in terms of the Kolmogorov constant in three-dimensional isotropic developed turbulence. In fact, in 1962 Lilly published a *LES* of buoyant convection in the atmosphere using Smagorinsky's model. The first application of the latter to engineering flows was the pioneering study of a plane channel done by Deardorff, another meteorologist, who with his collaborators started at the same time an impressive series of works on large eddy simulations of the planetary boundary layer [64].

In *LES*, the large energy carrying length scales of turbulence are resolved completely and the small structures are modelled. The separation of these large and small scales is performed by applying a low-pass filter to the Navier-Stokes equations and the effect of the small scale turbulence on the resolved scales is modelled using a sub-grid scale (*SGS*) model. The *SGS* model commonly employs information from the smallest resolved scales as the basis for modelling the stresses of the unresolved scales. Consequently, it is imperative that the resolved length scales are captured accurately by the numerical scheme. This, in turn, requires that the numerical error of the scheme is sufficiently small and hence, high-order numerical schemes are necessary. The *SGS* model is an integral component of the *LES* calculations and is therefore an influential factor in the accuracy of the predictions. In contrast to expectations, in some cases, the classical (standard) Smagorinsky model performs better than the dynamic Smagorinsky model. Therefore, it is evident that there is a need of experimental and numerical work to assess the performance of *LES* and the underlying *SGS* models in complex engineering flows. The advances in construction of *SGS* models for *LES* of a range of engineering flows encompass improvements not only in numerical solution but also in the process representations for accurate system definition [60].

III.2.1.2.a Sub-grid Scale Modelling

Smagorinsky Model

LES can be divided into three distinguished categories or approaches in the context of sub-grid scale (*SGS*) modelling : the eddy-viscosity model, similarity model and mixed model, where the last one is a combination of the former two models. The main goal in all these three approaches is to provide and implement an effective model to account for the majority of unresolved scales in the turbulent flow. Eddy-viscosity models are more popular than other available models in the *LES*. This model is based on the Boussinesq assumption in bridging the turbulent and molecular transports through a so-called turbulent or eddy-viscosity, an artificial

viscosity. Considering this fact, the *SGS* stress tensor can be defined as :

$$\tau_{ij} = -2\nu_t \bar{S}_{ij} + \frac{1}{3}\tau_{kk}\delta_{ij} \tag{III.16}$$

where ν represents the sub-grid scale eddy viscosity :

$$\bar{S}_{ij} = \frac{1}{2}\left(\frac{\partial \bar{u}_i}{\partial \bar{x}_j} + \frac{\partial \bar{u}_j}{\partial \bar{x}_i}\right) \tag{III.17}$$

The first *SGS* model or *LES* was proposed by Smagorinsky [66] based on the idea that the energy produced in resolved scales is equal to the energy dissipation on unresolved/small scales. The mechanism is such that the large eddies carrying the major fraction of turbulent energy transfer this energy to smaller scales. There is no doubt that physically, the viscous action is associated with the energy dissipation process. Since in an *LES* formulation the larger scales are resolved, it appears that the turbulent *SGS* stresses are smaller than their counterpart in *RANS*. The point is how much burden could be put on the *SGS* modelling that determines the key success to the *LES*. This aspect should be taken into account regardless of the energy transfer.

In the Smagorinsky model the turbulent eddy-viscosity is related to the grid filter width and strain rate :

$$\nu_t = \left(C_s \bar{\Delta}\right)^2 \left|\bar{S}\right| \tag{III.18}$$

where the velocity scale is proportional to the modulus of the filtered strain rate tensor :

$$\left|\bar{S}\right| = \sqrt{2\bar{S}_{ij}\bar{S}_{ij}} \tag{III.19}$$

C_s , is the Smagorinsky constant. The filter width Δ can be computed as the size of mesh spacing in the x, y and z directions :

$$\bar{\Delta} = (\Delta_x \Delta_y \Delta_z)^{\frac{1}{3}} \tag{III.20}$$

The Smagorinsky constant can be varied from one flow case to another flow case and also depends on the Reynolds number of the flow. Several studies reported that C_s , can take different values $(0.05 < C_s < 0.5)$.

In order to obtain the correct behaviour close to the walls, a Van Driest type damping function is introduced near the solid boundaries that account for the reduction of small fluctuations at those locations. This damping function is defined as : $\left(1 - \exp\left(\frac{-z^+}{25}\right)\right)$

where z^+ is the dimensionless distance from the wall. Thus, the full eddy viscosity term in the Smagorinsky model takes the form :

$$\nu_t = \left[C_s\bar{\Delta}\left(1 - \exp\left(\frac{-z^+}{25}\right)\right)\right]^2 \left|\bar{S}\right| \tag{III.21}$$

The Smagorinsky model is a popular *SGS* model due to its simplicity, robustness and its ability to reproduce the global energy flux from the re- solved to small scales. However, it suffers from a few shortcomings, firstly because of the Smagorinsky constant in the viscosity term, requiring a priori information on the flow topology (which varies for different flow problems). This issue can create excessive dissipation in certain types of flow. Another issue is that it needs an ad-hoc wall damping near the solid walls to correct the near-wall behaviour of the model [67].

Smagorinsky-Lilly Model

The Smagorinsky-Lilly model is the simplest and probably the most widely used model. Originally, this model was derived for meteorological purposes by Smagorinsky (1963) and soon applied in academic and industrial flows. In this model, the *SGS* viscosity is defined as [66] :

$$v_t = (C_s\Delta)^2 \left|\bar{S}\right| \tag{III.22}$$

Where C_s is the Smagorinsky constant, Δ is the filter width and $\left|\bar{S}\right|$ is the magnitude of resolved scale strain rate tensor defined as :

$$\left|\bar{S}\right| = \sqrt{2\bar{S}_{ij}\bar{S}_{ij}} \tag{III.23}$$

The Smagorinsky constant was derived by Lilly (1966) to be 0.18 in homogenous isotropic turbulence (HIT) for the inertial subrange. However, this value has been found to cause excessive dissipation. For most of the flows, a value of 0.1 has been found to give the best results when the grid filter is assumed to be equal to $V^{1/3}$. There are also examples where the filter width is assumed to be $2V^{1/3}$, for which case the coefficient is taken as 0.065 Kim (1983). Regardless of the filter width, this model has two major drawbacks. Laminarisation and transitional effects

are not sufficiently captured since the SGS viscosity is always positive, thus the Smagorinsky model is always dissipative. Secondly, the model coefficient needs to be reduced near the walls in order to capture the true behaviour of the flow near the wall boundaries. This is commonly accomplished by multiplying the model coefficient with a damping function proposed by van Driest (1956) :

$$C_s^d = C_s\left(1 - e^{(-y^+/A^+)^3}\right)^{1/2} \tag{III.24}$$

Here $A^+$is 25 and y^+ is the non-dimensional wall coordinate [66].

Dynamic Smagorinsky-Lilly Model

Germano et al. (1991) [44] proposed a modified version of the Smagorinsky model (SM) in which the constant C, is computed dynamically varying in time and space. Like the SM, the DSM also benefits from the Boussinesq approximation for the stress tensor term. In order to dynamically compute the eddy viscosity term, the DSM applies (along with the grid filter) an additional explicit secondary filter called the "test filter". The grid scale of this test filter is denoted by $\tilde{\Delta} = \alpha\bar{\Delta}$; the test-filter width $\tilde{\Delta}$ must be greater than the grid-filter width $\tilde{\Delta}$,i.e., $\alpha > 1$. Applying the test filter result in the Germano identity requiring :

$$L_{ij} = T_{ij} - \tau_{ij} = \widetilde{\overline{u_i}\overline{u_j}} - \widetilde{\overline{u}_i}\widetilde{\overline{u}_j} - \left(\widetilde{\overline{u_i}\overline{u_j}} - \widetilde{\overline{u_i}\overline{u_j}}\right) = \widetilde{\overline{u_i}\overline{u_j}} - \widetilde{\overline{u}_i}\widetilde{\overline{u}_j} \tag{III.25}$$

where T_{ij} is the SGS stress on the test-filter level. The stress components L_{ij} can be interpreted as the stress associated with the smallest resolved scales between the test-filter scale $(\tilde{\Delta})$ and the grid-filter scale $(\bar{\Delta})$. The stress tensor L_{ij} is called the Leonard stress and can be directly computed from the resolved scales.

If $\bar{C}_S$, is assumed not to change significantly from the grid-filter to the S test-filter scales, the error generated by using the Smagorinsky model in the Germano identity is :

$$E_{ij} = L_{ij} - \frac{\delta_{ij}}{3}L_{kk} - \bar{C}_S M_{ij} \ , \ M_{ij} = 2\bar{\Delta}^2\left(\widetilde{\left|\bar{S}\right|\bar{S}_{ij}} - \alpha^2\eta\widetilde{\left|\bar{S}\right|}\widetilde{\bar{S}_{ij}}\right) \tag{III.26}$$

with $\eta = \tilde{C}_s/\bar{C}_s$. Generally $\alpha = 2$ and the scale variance $\eta = 1$ is assumed. Following Lilly's idea, the model coefficient $\bar{C}_S$, is obtained by seeking a value for $\bar{C}_S$, which minimises the square of the error E^2. Therefore, taking $\partial E^2/\partial\bar{C}_S$, and setting it to zero gives :

$$\bar{C}_S = \frac{L_{ij}M_{ij}}{M_{ij}M_{ij}} \tag{III.27}$$

Thus, the model coefficient is a local quantity, varying in time S and space in a fairly wide range with positive and negative values. Although a negative $\bar{C}_S$, (and therefore a negative ν_T) is often interpreted as the flow of energy from the sub-grid scale eddies to the resolved eddies (referred to as "back-scatter") and regarded as a desirable attribute of the dynamic model; too large a negative ν_T causes numerical instability, which lead to divergence of the numerical solution. To avoid this, $\bar{C}_S$ is simply clipped at zero [67].

III.2.1.2.b Filter(Filtering Approach)

Large eddy Simulation (LES) is a numerical technique used for solving transient and turbulent flows. It is based on resolving the larger scales, which characterise most of the energetic structures and are problem dependent, and modelling the smaller ones, which are assumed to be universal. In this sense, LES can be regarded as a compromise between the Direct Numerical Simulation (DNS) and Reynolds Averaged Navier-Stokes $(RANS)$ approach. In DNS, all relevant turbulent scales are directly resolved, whereas they are modelled in $RANS$ approach. To perform true DNS, the spatial resolution has been estimated to be order of $\mathrm{Re}_l^{9/4}$.

This requirement is an important restriction for the high Reynolds number flows and hence engineering applications. The $RANS$ approach, on the other hand, offers significant savings of computational time with the underlying assumption that the instantaneous flow is composed of mean and fluctuating components. This assumption leads to a set of transport equations with numerous, empirical based model constants. To be considered an alternative to both $RANS$ and DNS, the Navier-Stokes equations are processed via a filtering operation, by which the larger scales are isolated from the smaller scales. There are two filtering approaches : implicit and explicit filtering. In implicit filtering, the flow equations do not explicitly contain the information on the filter shape or width. The information is contained implicitly in the sub-grid scale (SGS) model for the unfiltered stresses. Practically, the discrete grid cell acts as a filter width; the scales larger than grid cell are resolved and the scales smaller than grid cell are modelled via a SGS model. This approach is adopted in this thesis. In explicit filtering, a second explicit filter is applied to the non-linear terms to reduce truncation and aliasing errors. As explained Lund (1997), the explicit filtering operation is in general different from filtering the entire flow field which amounts a slight definition of SGS stress [68].

In LES, any flow variable, $f(x)$, can be decomposed into a resolved scale component $\bar{f}(x)$, and a sub-grid scale component :

$$f'(x), f(x) = \bar{f}(x) + f'(x) \tag{III.28}$$

The resolved scale component is filtered from the sub-grid scale component via the filter function, G, throughout the flow domain, D as :

$$\bar{f}(x) = \int_D f\left(x'\right) G\left(x, x'\right) dx' \tag{III.29}$$

The filter function must satisfy the normalisation function $\int_D G\left(x, x'\right) dx' = 1$. Filter functions have a wide variety to choose from, including Gaussian filter, Fourier cut-off filter and box filter. In this thesis, the filtering operation is performed in physical space ; therefore, the box filter is employed. For the box filter, the filtering is adopted by invoking the volume of the computational cell V as :

$$G\left(x, x'\right) = \begin{cases} 1/V \text{ x' } \in \text{ V} \\ 0 \text{ otherwise} \end{cases} \tag{III.30}$$

Substitution of Equation III.29 into Equation III.30 results in,

$$\bar{f}(x) = \frac{1}{V} \int_V f\left(x'\right) dx' \text{ x' } \in \text{ V} \tag{III.31}$$

Since the application of LES to compressible flow is a new research area and still not well developed in terms of the numeric and modelling of various extra terms that arise due to the variation of density, LES is mostly applied to incompressible flows. The governing filtered continuity and momentum equations for the incompressible Newtonian fluid takes the form :

$$\frac{\partial \bar{u}_i}{\partial x_i} = 0 \tag{III.32}$$

$$\frac{\partial \bar{u}_i}{\partial t} + \frac{\partial \left(\overline{u_i u_j}\right)}{\partial x_j} = -\frac{1}{\rho}\frac{\partial \bar{p}}{\partial x_i} + \frac{\partial}{\partial x_j}\left(\nu \frac{\partial \bar{u}_i}{\partial x_j}\right) \tag{III.33}$$

The term $\overline{u_i u_j}$ can be extracted in terms of resolved scale and sub-grid scale components as :

$$\begin{aligned} \overline{u_i u_j} &= \overline{(\bar{u}_i + u'_i)(\bar{u}_j + u'_j)} = \overline{\bar{u}_i \bar{u}_j} + \overline{\bar{u}_i u'_j} + \overline{u'_i \bar{u}_j} + \overline{u'_i u'_j} \\ &= \overline{\bar{u}_i \bar{u}_j} + \bar{u}_i \bar{u}_j - \bar{u}_i \bar{u}_j + \overline{\bar{u}_i u'_j} + \overline{u'_i \bar{u}_j} + \overline{u'_i u'_j} \\ &= \bar{u}_i \bar{u}_j + L_{ij} + C_{ij} + R_{ij} \end{aligned} \tag{III.34}$$

Where L_{ij}, C_{ij} and R_{ij} are known as the Leonard stress tensor, cross stress tensor and sub-grid scale Reynolds stress tensor, respectively.

$$
\begin{aligned}
L_{ij} &= \overline{\bar{u}_i \bar{u}_j} - \bar{u}_i \bar{u}_j \\
C_{ij} &= \overline{\bar{u}_i u'_j} + \overline{u'_i \bar{u}_j} \\
R_{ij} &= \overline{u'_i u'_j}
\end{aligned}
\tag{III.35}
$$

The Leonard stress involves only filtered scales which are known. The cross stress can be specified in terms of the filtered scales, and hence is also known. However, the sub-grid Reynolds stress remains unknown. Therefore, sub-grid modelling is required for the closure. Commonly, the three stresses are defined in terms of the sub-grid scale stress τ_{ij}^{sgs} defined as [68] :

$$\tau_{ij}^{sgs} = L_{ij} + C_{ij} + R_{ij} \tag{III.36}$$

Substituting Equation III.36 into Equation III.37, becomes :

$$\tau_{ij}^{sgs} = \overline{u_i u_j} - \bar{u}_i \bar{u}_j \tag{III.37}$$

Then, the filtered form of the Navier-Stokes equations becomes :

$$\frac{\partial \bar{u}_i}{\partial t} + \frac{\partial \left(\bar{u}_i \bar{u}_j\right)}{\partial x_j} = -\frac{1}{\rho}\frac{\partial \bar{p}}{\partial x_i} + \frac{\partial}{\partial x_j}\left(\nu \frac{\partial \bar{u}_i}{\partial x_j}\right) - \frac{\partial \tau_{ij}^{sgs}}{\partial x_j} \tag{III.38}$$

In the case of rotation, the Coriolis and centrifugal forces take place in Equation III.39 as :

$$\frac{\partial \bar{u}_i}{\partial t} + \frac{\partial \left(\bar{u}_i \bar{u}_j\right)}{\partial x_j} + \in_{ij3} 2\Omega \bar{u}_j = -\frac{1}{\rho}\frac{\partial \bar{p}}{\partial x_i} + \frac{\partial}{\partial x_j}\left(\nu \frac{\partial \bar{u}_i}{\partial x_j}\right) - \frac{\partial \tau_{ij}^{sgs}}{\partial x_j} \tag{III.39}$$

The third term on the left-hand side of Equation III.39 is the Coriolis force, represented by Levi-Civita's alternating tensor. Centrifugal force is combined with the pressure gradient term, since it is conservative type of force. The resulting pressure is referred to as the modified pressure, $\bar{p}$. The last term of Equation III.39 represents the sub-grid scale stress (SGS), which needs to be modelled. The SGS stress tensor is modelled based on the Boussinesq assumption.

$$\tau_{ij}^{sgs} - \frac{1}{3}\frac{\partial \bar{u}_i}{\partial t}\delta_{ij}\tau_{kk}^{sgs} = -2v_l \bar{S}_{ij} \tag{III.40}$$

Where δ_{ij} is the Kronecker-delta, v_l is the sub-grid scale eddy viscosity and $\bar{S}_{ij}$ is the resolved scale strain rate tensor which is given as [68] :

$$\bar{S}_{ij} \equiv \frac{1}{2}\left(\frac{\partial \bar{u}_i}{\partial x_j} + \frac{\partial \bar{u}_j}{\partial x_i}\right) \tag{III.41}$$

In DNS, the velocity field $U\,(x,\ t)$ has to be resolved on length scales down to the Kolmogorov scale η. In LES, a low-pass filtering operation is performed so that the resulting filtered velocity field $U\,(x,\ t)$ can be adequately resolved on a relatively coarse grid. Specifically, the required grid spacing h is proportional to the specified filter width Δ. In the ideal case the filter width is somewhat smaller than the size of the smallest energy containing motions. For then the grid spacing is as large as possible, subject to the condition that the energy containing motions are resolved [68].

III.2.1.3 Detached Eddy Simulation (DES)

Detached Eddy Simulation (DES) is a hybrid method which combines LES and $RANS$. As LES becomes extremely computationally expensive within the near wall region, one method used to reduce this expense is to use another formulation. DES uses the LES formulation for the majority of the domain and switches to the $RANS$ formulation near wall boundaries. The switch between the two formulations can be accomplished using turbulence length scales, distance variables or specified by the user within certain zones known as zonal DES [69].

The description DES was originally coined by Spalart et al. and refers to an approach where unsteady $RANS$ turbulence modelling and mesh spacing is used in the boundary layer, while LES is employed in the core and separated regions of the flow. In the near wall regions, the $RANS$ turbulence model, which has been calibrated in thin shear layer flows, has complete control over the solution. In the LES region, the turbulence model changes to an SGS formulation. The turbulence modelling in the LES regions thus has a comparatively small influence compared to that in the $RANS$ region, since the larger energy carrying eddies are resolved, allowing for smaller margin of error and providing more realistic core conditions for the $RANS$ portions of the flow. Thus, the streak instability cycle, the inertial layer and most of the wake region are subsumed by the $RANS$ portion of the model. In fact, the DES solution should in theory reduce to the equivalent $RANS$ result, unless the flow contains some feature that introduces large scale unsteadiness into the outer flow [58].

III.2.1.4 Wall-modelled LES (WMLES)

In order to avoid the expensive resolution of fine near-wall structures at high Reynolds numbers, wall-modelled LES employs modelling approximations over the inner region of the boundary layer and switches to LES for the outer region and beyond. Thus, near-wall resolution requirements for LES and DNS are similar. The cell count in the first few per cent of the flow

nearest the wall often accounts for the vast majority of the overall grid numbers, even when the most important physical features occur well away from the wall. Resolving this issue has led to a great deal of effort in the *LES* community [70].

The near-wall turbulence length scales increase linearly with the wall distance, resulting in smaller and smaller eddies as the wall is approached. This effect is limited by molecular viscosity, which damps out eddies inside the viscous sub-layer. As the R_e number increases, smaller and smaller eddies appear since the viscous sub-layer becomes thinner. In order to avoid the resolution of these small near-wall scales, *RANS* and *LES* models are combined such that the *RANS* model covers the very near-wall layer, and then switches over to the *LES* formulation once the grid spacing becomes sufficient to resolve the local scales. Where the *RANS* layer extends outside of the *VS*, thus avoiding the need to resolve the inner "second" row of eddies depicted in the sketch [69].

It should be noted that reductions in grid resolution similar to *WMLES* can be achieved with classical *LES* models when using *LES* wall functions. However, the generation of suitable grids for *LES* wall functions is very challenging as the grid spacing normal to the wall and the wall parallel grid resolution requirements are coupled and strongly dependent on Reynolds number (unlike *RANS* where only the wall-normal resolution must be considered). In ANSYS Fluent, the *WMLES* formulation can be selected as one of the *LES* options; in ANSYS CFX it is always activated inside the *LES* zone of the Zonal Forced LES (ZFLES) method [69].

III.2.2 Quality and Reliability of Numerical Simulation

The numerical fluid flow analysis has been a well-reviewed subject for almost a century. However, it is only in the last decade that a lot of concern about the reliability of numerical simulation has been cited. Available literature can be classified as targeting different aspects of numerical simulation. The relevant aspects for the current study are quality and reliability in CFD, formal policies on numerical uncertainty in general, and concerning *LES*, the grid resolution, accuracy limitations and error estimation. CFD techniques commonly used to predict turbulent flow properties are inherently susceptible to modelling and numerical errors. As CFD is brought into widespread use, it is important to limit these errors in solution without an excessive increase in computational cost. Therefore, a prior assessment of the quality of the particular CFD technique is necessary. CFD has now more or less become a standard tool for fluid flow investigations, however a quality assessment of the results is often unavailable,

particularly for *LES*. Quality control in CFD can be implemented with guidelines for calculation with sufficient accuracy and reporting results with sufficient information to judge the result quality. *RANS* methods are widely used in industry, chiefly because of their speed, and lower sensitivity to numerical and grid issues. Methods of assessing quality of results obtained from *RANS* simulations are well established. However, *RANS* methods can yield erroneous results for certain flow geometries. Furthermore, they do not provide an instantaneous time history of the flow, which may be required to correctly model flow features such as combustion or acoustics. *LES* can offer more accuracy in such scenarios, providing not only the full-time history of the flow, but also resolving small scale, energetic eddies [60].

III.2.2.1 DNS criteria

Three criteria have been formulated and tested, which allow for the selection of grids adequate for direct numerical simulation :

Criterion (1) requires great periodicity lengths in the horizontal directions to record the longest wave-lengths observed. The grids with short periodicity lengths exactly meet this criterion at the lowest Rayleigh number. Nevertheless, the skewed varicose instability found by starting from random initial conditions cannot develop the expected wave-length because of the wave-length restrictions by the grid. The periods of the bimodal travelling waves observed at the next higher Rayleigh number are also slightly too short. The simulations with large periodicity lengths show none of these deficiencies. Thus, for simulation in the transition range, one should use periodicity lengths about two times the expected values.

Criterion (2) requires a time resolution of the region near the wall due to the linear wall approximations introduced. The grids applied to simulations of turbulent convection use between 1 and 5 nodes within the thermal boundary layer thickness. It must be concluded from the numerical results that the calculated Nusselt number reacts sensitively to increasing the node number from 1 to 3 within. Further increases have no significant influence on the accuracy of the numerical results. Thus, for, it is sufficient to use about three nodes in the vertical direction within the thermal boundary layer thickness. If it is the purpose of a simulation to investigate statistical data of turbulence, about the same number of nodes should also be used within each of the next two thermal boundary layer thicknesses to record adequately the sharp peaks or transitions in many statistical data of turbulence in this range. For Prandtl numbers considerably below unity, one must consider the viscous sub-layer thickness instead of the thermal boundary layer thickness.

Criterion (3) in general requires very fine grids to resolve the smallest scales of turbulence, because the sub-grid scale terms have been neglected. The numerical simulations performed at the highest Rayleigh number show only small deficiencies in case of grids which are too coarse. For these coarse grids, the Nusselt number and the rms values of velocity and temperature fluctuations, which have been found to be the most sensitive results, both increase only slightly with decreasing node number. The three finest grids sufficiently resolve the smallest scales of turbulence. The "Kolmogorov criteria" of the equation and prescribe very low values for the required mean grid widths. The "isotropic grid criteria" of equation and predict larger required grid widths, which allows for more efficient simulation of comparable accuracy than the "Kolmogorov criteria" [71].

III.2.2.2 LES criteria

III.2.2.2.a Spatial Grid Resolution

In general, *LES* results are in better agreement with experimental evidence compared to *RANS* if a sufficiently fine grid is employed. However, without a prior knowledge of flow characteristics, it is difficult to ascertain the "sufficient" resolution. As claimed by Celik (2005), a good *LES* is almost a *DNS*, i.e. for correct resolution of wall layers and prediction of transition, *LES* requires an extremely fine grid. It was pointed out by Speziale that a good *LES*, as the grid resolution tends to the smallest scales, i.e. the Kolmogorov scales, tends to *DNS*. As a consequence, grid independence cannot really exist in *LES* as a grid-independent *LES* is actually a *DNS* and therefore the systematic grid convergence studies offer no great benefit. The *LES* philosophy loses its meaning if it achieves grid independence and the advantage of *LES* being more economical than *DNS* on account of resolving only the most energetic eddies, is lost. Physical phenomena, including mixing and combustion depend strongly on the intensity of turbulent fluctuations and the convection of these fluctuations, exhibited as turbulent dissipation ; the accurate prediction of turbulent statistics becomes important. This makes quality assessment measures imperative for *LES* in engineering applications [60].

In (1990), a number of attempts were made at reducing the computational requirements of *LES* for wall-bounded flows. Most of these were attempts at manipulating the grid such that all the near-wall eddies could be resolved without having a large number of gridpoints in the outer layers. In wall-bounded flows, the near-wall flow structures are extremely small when compared to the overall flow dimensions. However, these small structures play a very important part in the turbulent boundary layer dynamics and therefore need to be well resolved.

In typical mean flow computations, the large mean velocity gradients are resolved using grid stretching in the wall-normal direction. In turbulence simulations, however, a fine near-wall mesh is also required in the direction parallel to the wall. This fine resolution was normally extended into the outer layers. This was not necessary ; consequently, the attempts at lowering computation cost by modifying the grid employed were largely successful [60].

III.3 Computational domain and numerical requirements

The adequacy of the computational domain is assessed later by examining the streamwise two-point correlations which must be large enough to include the largest length scale structures, periodic boundary conditions for the velocity components were applied in streamwise and circumferential directions, whereas no-slip boundary conditions were imposed at the wall, in additional to the Neumann boundary conditions were used for the pressure. Periodic boundary conditions were imposed in the streamwise and the spanwise directions since the turbulent pipe flow is fully developed. The periodic boundary in the streamwise direction can be justified provided that the flow can be considered homogeneous in that direction and that the length of the computational domain was sufficiently large to include the largest scale of the turbulent motions in the flow. This can be checked by ensuring the streamwise two-point correlation coefficients are uncorrelated at a separation of one-half period in the homogeneous directions and this is when these correlations fall of to zero value, according to this equation [72].

$$R_a(1/2\,L_z\,) = \frac{\langle a'(r,\theta,z,t)a'(r,\theta,z+1/2\,L_z\,,t)\rangle}{\langle a'(r,\theta,z,t)a'(r,\theta,z,t)\rangle} \approx 0 \tag{III.42}$$

A domain independence study has largely carried out for the moderate Reynolds number : the main findings indicate that the adequate domain length is $L = 5D$ in the Newtonian fluid. For the shear-thinning power-law fluids, according to Singh et al. [42], the flow index affects the long helical structures near the wall and at the centre of pipe, where the range of length scales in the flow increases with decreasing flow index, where Singh et al. [42] choose $4\pi D$ as domain length for the flow index $0.6 < n < 1$, and $16D$ for $n = 0.4$. In the present study, it kept the length domain of Singh et al. [42] : was set to be $12D$ for $0.6 < n < 1$, and $16D$ for $n = 0.4$; these domain lengths are further checked for it adequacy via two-point axial correlations [72].

In order to achieve a realistic numerical simulation of a turbulent flow, the adequacy of numerical resolution in the direct numerical resolution is still one of the greatest challenges, where

the spatial and temporal resolutions must be sufficient fine to resolve the smallest length scale structures in turbulent flow. In other word, the Kolmogorov length and time scales must be resolved by the spatial and temporal network distribution : the distance between two sequential points in space and time should be proportional to the Kolmogorov scales. In this end, a number of criteria have been deduced to estimate this required numerical resolution. As mentioned above, the Grötzbach's criteria [71] are one of the large commonly used techniques for evaluating the spatial resolution, where he formulated three criteria. The first one concerns the computational domain which should be large enough to include the largest length scale structures, the second one requires that the vertical grid width distribution must be able to fully resolve the thin vortical layers in the vicinity of the wall responsible for the wall friction and for the turbulence production, which can be met by ensuring that at least three gridpoints within the viscous sub-layer. The last one requires the mean grid widths must be smaller than the smallest relevant turbulence elements. As for the temporal resolution, a more restrictive criterion must be applied to ensure that the time step is enough to resolve the smallest time scale structures in turbulent flow and to avoid numerical instabilities : This can be achieved by assuring that the imposed time step must be smaller than the Kolmogorov time scale [72].

Computations have been carried out on a finite difference scheme, second-order accurate in space and time. The numerical resolution is $(129\times129\times193)$ gridpoints in radial, circumferential, and axial directions, respectively, with a domain length of $20R$ [72].

In large eddy simulations (LES), numerical spatial resolution is always one of the biggest challenges. Indeed, the mesh imposed on the computational domain should be fine enough to capture and resolve the smallest scale structures in the turbulent flow, and limit the influence of the mesh on the accuracy of the results. A uniform distribution of gridpoints must be applied in the axial and circumferential directions (periodic directions) to use the trigonometric development elements in the pressure equation. A non-uniform distribution must be imposed in the normal direction of the wall where a refinement of the mesh near wall region is necessary for a better resolution in the zone close to the wall. In fact, in the viscous sub-layer, at least three gridpoints must be arranged so that the first grid point must be located at $(Y^+ < 1)$.

In order to ensure the precision of the spatial grid resolution, a study of the mesh independence is necessary. To this end, Gnambode et al. [73] performed this study with the LES code used in the present study for an Ostwald de Waele fluid with a flow index of 0.8 at a simulation Reynolds number of 8000, with different numbers of gridpoints in the circumferential, axial and

radial directions, presented respectively in (a), (b) and (c) in Figure III.11. They found that the grid of $(65 \times 65 \times 65)$ gridpoints in the axial, radial and circumferential directions, respectively, and admitting an adequate resolution is considered as a good compromise between the required precision and the CPU time [72].

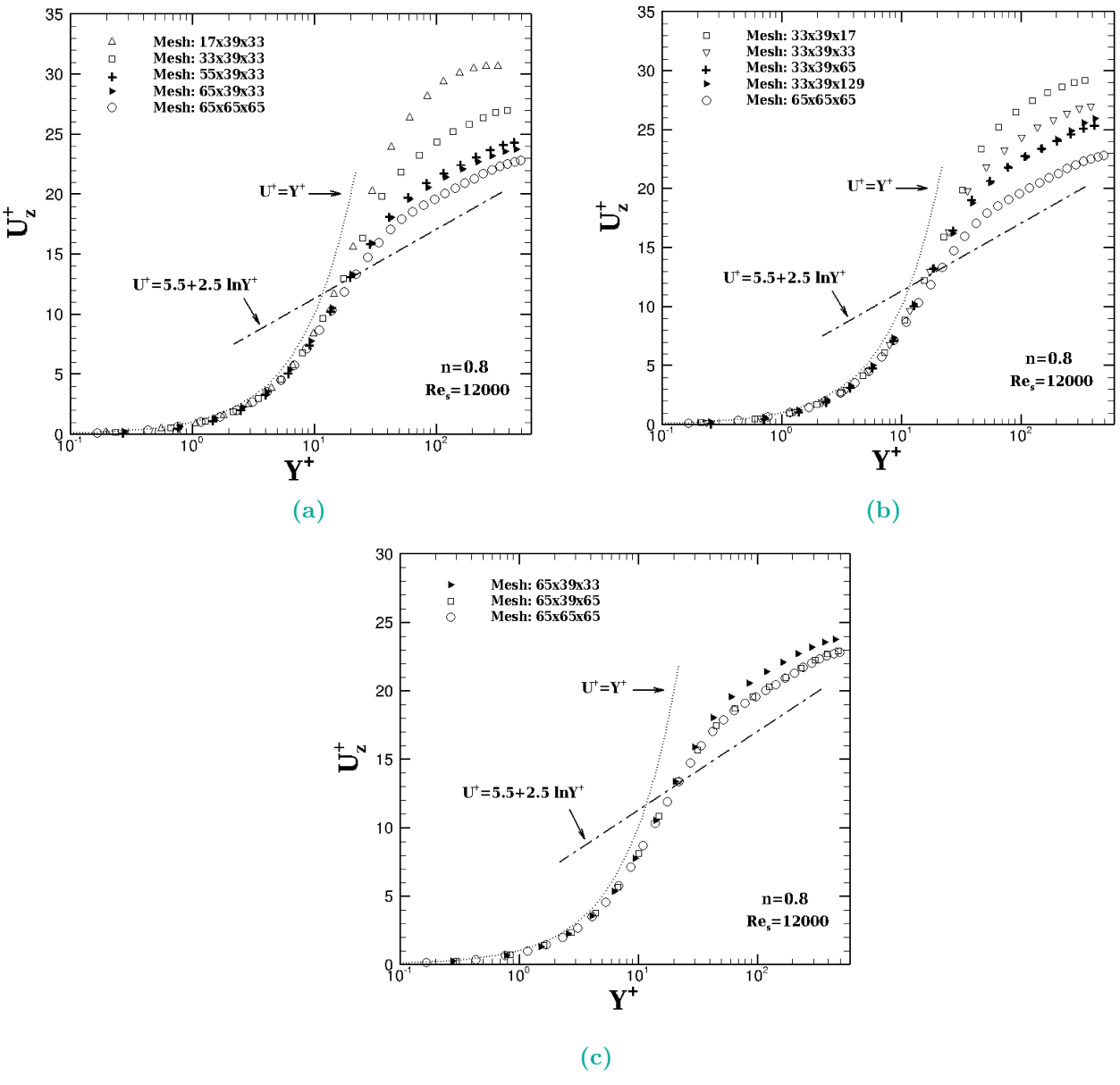

Figure III.11 – Gnambode mesh independence study [73].

Note that in their investigations, Gnambode et al. [73] used a length domain in the flow direction (axial direction) of $20R$. The primitive variables will be calculated at different points, located on the faces of the cells for the velocity components or in the centre of the cells for the scalars Figure III.12. The variables $q_\theta = rV_\theta, q_r = rV_r$ and $q_z = V_z$ (where V_θ, V_r, V_z are the velocities of the fluid in the three directions) and they are considered in order to avoid the

problem of the singularity on the axis of the driving. The positions of the variables are defined by the following spatial coordinates :

$$\bar{q}_\theta \rightarrow \left(i, j+\frac{1}{2}, k+\frac{1}{2}\right) \text{ where } (\theta_c(i), r_m(j), z_m(k)) \tag{III.43}$$

$$\bar{q}_r \rightarrow \left(i+\frac{1}{2}, j, k+\frac{1}{2}\right) \text{ where } (\theta_m(i), r_c(j), z_m(k)) \tag{III.44}$$

$$\bar{q}_\theta \rightarrow \left(i+\frac{1}{2}, j+\frac{1}{2}, k\right) \text{ where } (\theta_m(i), r_m(j), z_c(k)) \tag{III.45}$$

$$\bar{p}, \bar{\Theta} \rightarrow \left(i+\frac{1}{2}, j+\frac{1}{2}, k+\frac{1}{2}\right) \text{ where } (\theta_m(i), r_m(j), z_m(k)) \tag{III.46}$$

with :

$$\begin{aligned} &\theta_c = (i-1)\Delta\theta, i = 1....n_1 \\ &\theta_m = (i-1/2)\Delta\theta, i = 1....(n_1-1),\ \Delta\theta = \frac{2\pi}{n_1-1} \end{aligned} \tag{III.47}$$

$$\begin{aligned} &r_c = (j-1)\Delta r, j = 1....n_2 \\ &\mathrm{r}_m = (j-1/2)\Delta r, j = 1....(n_1-1),\ \Delta r = \frac{R.f(r)}{n_2-1} \end{aligned} \tag{III.48}$$

$$\begin{aligned} &z_c = (k-1)\Delta z, k = 1....n_3 \\ &\mathrm{z}_m = (k-1/2)\Delta z, k = 1....(n_3-1),\ \Delta r = \frac{L}{n_3-1} \end{aligned} \tag{III.49}$$

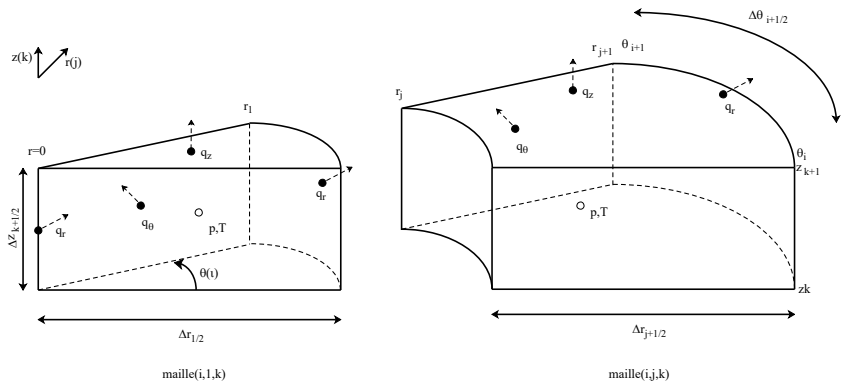

Figure III.12 – Staggered mesh [72].

Note that in the radial direction, a non-uniform grid resolution specified by a hyperbolic function has been applied in the radial (r) direction, where the gridpoints in this direction are closest together at the cylinder wall and progressively spaced away from the wall towards the centre of the cylinder Figure III.13.

The mesh refinement is given by the hyperbolic equation :

$$y_j = |r_j| \sin\left[\pi + (j-1)\theta\right] \ \text{(j=1, ..., m}_j\text{)} \tag{III.50}$$

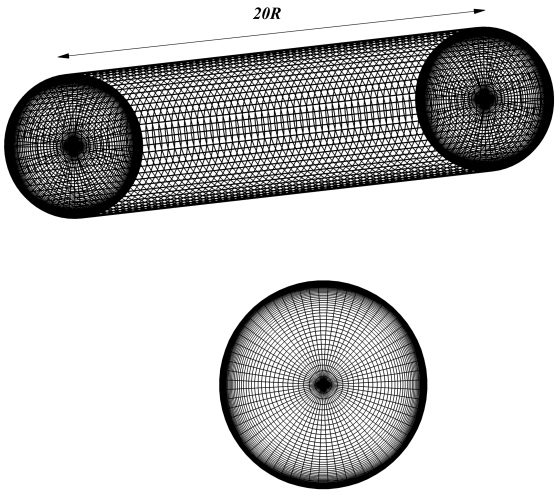

Figure III.13 – Grid Mesh [72].

$$z_j = |r_j| \cos\left[\pi + (j-1)\theta\right] \tag{III.51}$$

$$\theta = \frac{\pi}{40(m_k - 1)} \tag{III.52}$$

$$r_j = r_a \frac{\tanh(\alpha \xi_i)}{\tanh(\alpha)} \tag{III.53}$$

$$\xi_j - 1 + 2\frac{j-1}{m_j - 1} \tag{III.54}$$

$$\alpha = \frac{1}{2} \ln\left(\frac{1+b}{1-b}\right) \tag{III.55}$$

$$r_\alpha = \frac{1}{2}(r_{outer} - r_{inner}) \tag{III.56}$$

Parameter b is used to control the extent of the grid to the walls and typical values for this study are between 0.7 and 0.95. The parameters m_i, m_j, m_k are the number of vertices in the axial, radial, and tangential directions respectively. α is the adjustable parameter to determine the concentration of gridpoints in the flow region near the wall.

It should be mentioned that thanks to the hyperbolic function implemented in the radial direction, it was possible to obtain many mesh points in the viscous sub-layer $(Y^+ < 5)$ (a minimum of 26 gridpoints) where the first point near-wall grid in all simulations is located at $(Y^+ < 1)$ at the highest rotational speed $(N = 3)$. The resolution along the radial direction in wall units (Δr^+) varies from 0.0506 to 12.4 in the stationary case, while it varies from 0.0511 to 12.5 in the rotating case with the highest rotation rate $(N = 3)$ [72].

Time is rendered dimensionless using the cylinder radius (R) and the maximum laminar flow velocity, U_{CL}. The calculations were carried out at a constant CFL and not at a constant time step [72].

Gnambode (2015) [73], performed a time-step independence study of the Ostwald de Waele fluid with a flow index of 0.75 through a no rotating pipe Figure III.14. The study considers CFL of $0.04R/U_{CL}$ or $0.01R/U_{CL}$ for stabilise the solutions and avoid the divergence problem. However, the time step which varies is limited by the value $\Delta t = 0.01$ for $n = 0.75$.

The statistics are calculated by averaging in the periodic directions and over time. The final data are obtained by ensemble average over the time interval from the scaled time $t = 250$ to $t = 8000$ for the smallest rotation rate. At the highest rotation rate, statistics are sampled from scaled time $t = 250$ to $t = 10000$ [72].

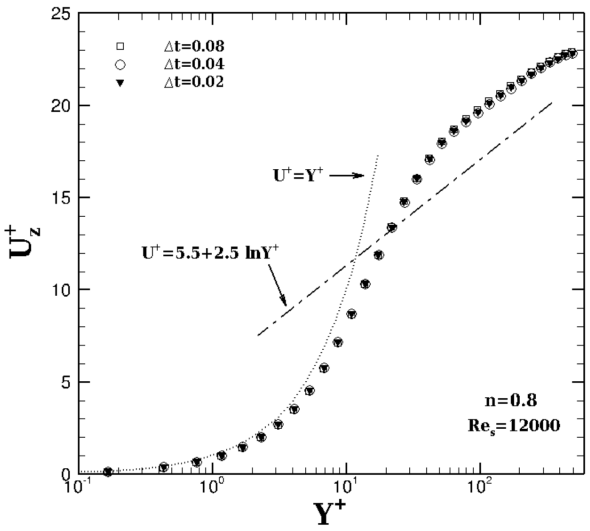

Figure III.14 – Gnambode Time Step [73].

III.3.1 Extended Smagorinsky Model

Ohta and Miyashita (2014) [39] carried out DNS and LES with an extended Smagorinsky sub-grid model of turbulent flow of non-Newtonian fluids with a viscosity described by the model of Ostwald de Waele and Casson's model. Their extended Smagorinsky model better describes turbulence in non-Newtonian viscous fluids. In order to assess the reliability of the extended SGS model used, the authors compared their results of the large eddy simulation with those of the DNS and showed that their predictions obtained using the LES agree reasonably with those of the DNS. The average velocity profiles obtained by these LES simulations with the extended Smagorinsky model rather than the LES simulation with the standard Smagorinsky

model closely matched those obtained by DNS as shown in Figure III.15.

The effects of SGS motions on resolved scales are modelled using a turbulent viscosity closure and the sub-grid stress tensor $\bar{\tau}_{ij}$ is related to the strain rate tensor $\bar{S}_{ij}$, by $\bar{\tau}_{ij} = -2v_t\bar{S}_{ij}$. In the non-Newtonian Smagorinsky model of Ohta and Miyashita (2014) [39], the turbulent viscosity is calculated by $v_t = (C_s f_s f_n \Delta)^2 \bar{S}_{ij}$, where is the calculation filter, C_s the constant of the model f_s , the van Driest wall damping function $f = \eta_w/\eta$, and f_n (which is an additional function defined as η_w/η, and η_w being the wall viscosity which is the same as the viscosity of the Newtonian fluid) is the correction function for the change in viscosity.

$$f_s = 1 - \exp\frac{-y^+}{A^+} \tag{III.57}$$

Where A^+ is the dimensionless parameter $(A^+ = 25)$

It notes that when the spatial filter is applied to the Navier-Stokes equations, in non-Newtonian viscous fluid flows (whose viscosity characteristics vary in space), additional terms (see terms $\bar{T}_{ij}$, in filtered Equation) are generated because the stress tensor is a non-linear function of the strain rate tensor. These additional terms, when using an Ostwald de Waele model, are written as Ohta and Miyashita (2014) [39].

$$\bar{T}_{ij} = \overline{\tau_{ij}\left(S_{ij}\right)} - \tau_{ij}\left(\bar{S}_{ij}\right) = 2K\left\{\overline{\left(2S_{kl}S_{lk}\right)^{\frac{n-1}{2}}S_{ij}} - \left(2\bar{S}_{kl}\bar{S}_{lk}\right)^{\frac{n-1}{2}}\bar{S}_{ij}\right\} \tag{III.58}$$

In the present study of LES, the additional terms are ignored. Indeed, Ohta and Miyashita (2014) [39] showed that these terms are much smaller than the sub-grid scale constraint (SGS).

These authors demonstrated this result by comparing stress profiles (SGS) with additional terms estimated from filtered DNS results for Ostwald Waele's fluids and Newtonian fluid. Therefore, in their study they focused on modifying the (SGS) model for the viscosity characteristics of the non-Newtonian fluid and ignored the additional terms to derive an SGS model for the non-Newtonian fluid [72].

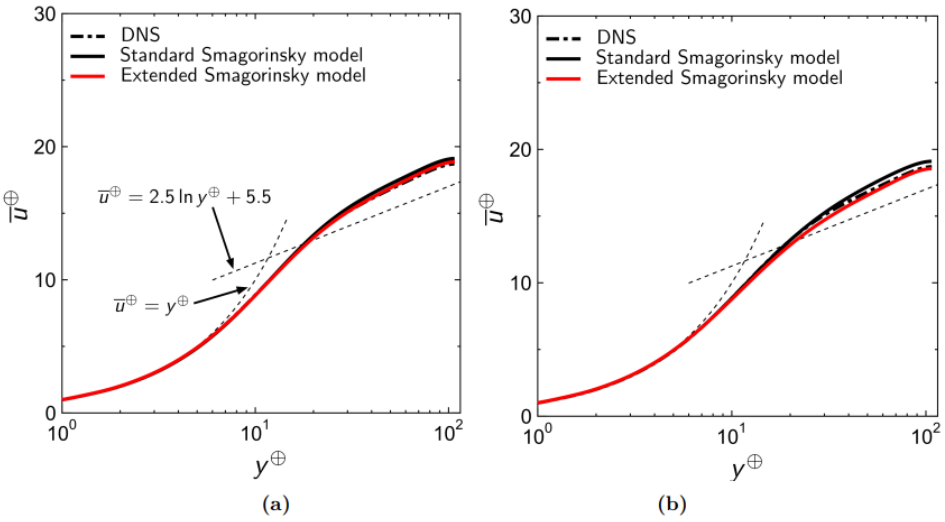

Figure III.15 – Validation de Ohta et Miyashita (2014) [39].

III.3.2 Rheological Modelling

The fluid modelled in this study is shear thinning power-law fluid, the shear stress is related to the shear rate by : $\tau = K(\dot{\gamma})^n$, where $\dot{\gamma}$ is the shear rate K is the consistency index n is the flow behaviour index. The apparent viscosity η is not constant for the power-law fluid is a function of the magnitude of the shear rate and is written in the form : $\eta = K\dot{\gamma}^{n-1}$. For $(n < 1)$, the apparent viscosity decreases with increasing shear rate and fluid is called pseudoplastic or shear-thinning. For $(n > 1)$, the apparent viscosity increases with shear rate increase and fluid is termed dilatant or shear-thickening. For $(n = 1)$, Newtonian flow behaviour is expected. Metzner and Reed (1955) [32] were the first to propose a definition of the generalised Reynolds number for the power-law fluids that based on the effective viscosity $\eta_{eff} = K(3n + 1/4n\ )^n(8U/D\ )^{n-1}$, it thus follows that the Metzner and Reed Reynolds number defined as $\mathrm{Re}_{MR} = \rho U^{2-n}D^n/8^{n-1}K(3n + 1/4n\ )^n$. Another commonly used generalised Reynolds number which reflects the flow behaviour in the vicinity of the wall region that plays an important role in transition and the development of turbulence in wall-bounded flows of fluids, which based on the apparent viscosity of the fluid at the wall $\eta_w = K(\dot{\gamma}_w)^{n-1}$. In additional, friction Reynolds based on the wall friction velocity and the mean viscosity on the wall $\mathrm{Re}_\tau = \rho u_\tau D/\eta_w$. Also, the wall units are presented in a similar manner to the Newtonian analysis, the dimensionless velocity or the power-law fluid is $U^+ = U/u_\tau$, where u_τ is the friction velocity and is defined as $u_\tau = \sqrt{\tau_w/\rho}$. Whereas the distance from the wall in wall units is also based on the viscosity of the fluid at the wall, it thus follows that $y^+ = \rho y u_\tau/\eta_w$ [72].

III.3.3 Boundary conditions and initial conditions

In the present study, it is interested in a fully developed turbulent flow of Ostwald de Waele fluid driven by a pressure gradient in the direction (z) at a simulation Reynolds number of 4000 through a cylinder in rotation around its axis. As the flow is homogeneous in the axial and circumferential directions, it is necessary to apply periodic boundary conditions in these two directions in order to use a smaller calculation domain [72].

The periodicity conditions are applied in the axial and azimuthal directions :

$$\begin{cases} \overline{q_i}(\theta, r, z) = \overline{q_i}(\theta, r, z + L_z) \\ \overline{q_i}(\theta, r, z) = \overline{q_i}(\theta + 2\pi, r, z) \end{cases} \tag{III.59}$$

Indeed, the length of the adequate computational domain must be large enough to include the largest length-scale structures in the flow, which can be checked by calculating the two-point correlation coefficients of the velocity fluctuations in the direction of flow. These coefficients must be uncorrelated with a half-period separation in the homogeneous directions and that is at this time that these correlations fall to zero according to this equation :

$$R_a(1/2L_z) = \frac{\langle a'(r, \theta, z, t) a'(r, \theta, z + 1/2L_z, t) \rangle}{\langle a'(r, \theta, z, t) a'(r, \theta, z, t) \rangle} \approx 0 \tag{III.60}$$

All current numerical calculations have been performed with a sufficient computational domain length of $20R$ in the (z) direction according to Gnambode et al. [73] with periodic boundary conditions along the axial and azimuth directions. While a boundary condition of non-slip is imposed on the pipe wall (adhesion condition). According to the assumption of the absence of slip, the fluid is supposed to adhere to the walls. The fluid velocity components cancel out at the pipe wall :

$$\begin{cases} r = 0, \dfrac{\partial \overline{q_z}}{\partial r} = \dfrac{\partial \overline{q_z}}{\partial r} = 0, \overline{q_r} \\ r = 1, \overline{q_z} = \overline{q_r} = \overline{q_\theta} = 0 \end{cases} \tag{III.61}$$

It should be noted that the velocity field was initialised according to the formulation of Orlandi and Fatica [9], which states to add a perturbation of specified zero divergence to the Poiseuille laminar profile :

$$\overrightarrow{v}(\overrightarrow{x, t = 0}) = \overrightarrow{U}_p + \Re[\varepsilon \overrightarrow{u_r}(r) e^{i\alpha z} + \varepsilon_\theta \overrightarrow{u_\theta}(r) e^{i(\alpha z + \beta\theta)}] \tag{III.62}$$

Indeed, the disturbance must verify the adhesion conditions and the periodicity imposed on the speed. Its average must be zero so that the bit rate is not modified. This condition is achieved for the chosen disturbance by taking wave numbers α and β respectively, equal to the inverse of the domain size in the periodic axial and azimuthal directions [72].

CHAPTER IV

DNS OF DILATANT FLUID

DNS OF OSTWALD DE WAELE FLUIDS

IV

ABSTRACT

The purpose of the present investigation is to ascertain and accurately the reliability and effectiveness of the DNS laboratory code to predict the flow quantities and turbulence statistics of the Ostwald de Waele fluid. This study also reveals the centrifugal force induced by the swirl driven by the rotating pipe wall on the flow pattern, rheological behaviour, and turbulence statistics. The present study investigates numerically a fully developed turbulent flow of pseudoplastic $(n = 0.75)$ and dilatant $(n = 1.2)$ fluids through an isothermal axially rotating pipe by means of the direct numerical simulation (DNS) approach at simulation Reynolds numbers of 5000 over a rotation rate range $(0 \leq N \leq 3)$. The numerical integration has been performed by the finite difference scheme, second-order accurate in space and time with a numerical resolution of $(129 \times 129 \times 193)$ gridpoints in axial, radial and circumferential directions, respectively. The governing equations have been discretised on a staggered grid using cylindrical coordinates with a computational domain length of $20R$ in the axial direction. The predicted results suggest that the decreased flow behaviour index results in an enhancement in the turbulent axial velocity in the core region. Furthermore, the radially growing centrifugal force induced by the swirl driven by the rotating pipe wall causes a supplemented force to the inertia force, which results in a noticeable reduction in the apparent fluid viscosity and a noticeable increase in the streamwise velocity of pseudoplastic and dilatant in the core region. The increased rotation rate results in a noticeable enhancement in the generation and transport mechanism of turbulence intensities of the axial velocity fluctuation from the wall vicinity towards the core region.

This increased rotation rate also enhances the transport mechanism of turbulence intensities of the radial velocity fluctuation from the axial velocity fluctuation. Moreover, the tangential turbulence intensities exhibit an apparent attenuation in the transport mechanism of turbulence intensities from the axial velocity fluctuation with increasing rotation rate for the pseudoplastic and dilatant fluids.

Keywords : DNS, centrifugal forces, fully developed, turbulence statistics, pseudoplastic, dilatant.

IV.1 Introduction

The flow through rotating pipes is of great practical interest because of the various industrial applications and is often encountered in multiple furnaces and combustors, as well as in rotating machinery. Several computational and experimental experiments have been carried out in recent years to understand the laminarisation phenomenon better and examine the impact of the rotating pipe wall on the mean characteristics and turbulence statistics.

The turbulent flow of Newtonian fluids through an isothermal axially rotating pipe is a problem of considerable significance. It has received much attention because of its various industrial applications. Much literature has investigated the turbulent flow characteristics through an isothermal pipe rotating around the axis by [13], [14], [15], [16], [17], [18], [19]. The research of Eggels et al. (1994) [16] performed one of the most important experimental and numerical analyses and discussions on turbulent pipe flow. Their findings suggest that the centrifugal force induced by the rotating pipe wall results in a pronounced attenuation of the normal wall and axial velocity fluctuation along the radial coordinates according to the Taylor-Proudman theorem because a rotating flow tends to become $2D$ in its plane of rotation. In addition, the attenuation of the shear stress also leads to a reduction of the friction factor.

In-depth research on the numerical analysis of hydrodynamic and thermal characteristics was conducted by Ould-Rouiss et al. in (2010) [30]. This work focused on the DNS and LES techniques of the fully developed forced convection heat transfer for airflow through a heated axially rotating pipe. The pipe wall was given a thermal boundary condition of uniform heat flow, and the Reynolds number was set at 5500 for the range of rotation rates $(0 \leq N \leq 7)$. The LES spatial resolution was also based on a mesh of $(39 \times 129 \times 129)$ gridpoints in the radial, tangential, and axial directions. In contrast, the DNS spatial resolution was based on a mesh of $(129 \times 129 \times 257)$ gridpoints. The rise in temperature variations toward the core of the pipe as the pipe rotates showed a clear tendency to increase the turbulence intensity

of temperature fluctuations in the core flow zone. Additionally, as the spinning pipe diameter raised, the centrifugal force caused by the revolving pipe wall caused a noticeable decrease in the axial turbulent heat flow and an increase in the azimuthal heat flux. On the other hand, the flow and the scalar transport seemed to be almost independent of the revolving pipe wall with a larger rotation rate $(N > 3)$.

Materials exhibiting shear-thinning non-Newtonian behaviour include slurries, pastes, suspended solids in liquids, and emulsions. Shear-thinning materials are frequently encountered in industries dealing with composite materials, rubber, pharmaceuticals, biological fluids, plastics, petroleum, soap and detergents, cement, food products, paper pulp, paint, light and heavy chemicals, oil field operations, fermentation processes, plastic rocket propellants, electrorheological fluids, ore processing, printing, and radioactive waste. The characterisation of the turbulent flow of non-Newtonian fluids inside the circular pipe is of practical importance due to these fluids' wide range of industrial applications. There is only a relatively limited amount of research due to their distinctive viscosity characteristics, which vary from those of Newtonian fluids.

Rudman and Blackburn (2006) [38] reported a direct numerical simulation (DNS) of the turbulent flow of non-Newtonian fluids using the spectral element Fourier method (SEM). The procedure is applied to the case of turbulent pipe flow, where simulation results of a shear-thinning fluid are compared to those of a Herschel–Bulkley fluid at the same generalised Reynolds number of 7500 with a domain length of $5\pi D$. They have also studied the flow of blood using a Carreau–Yasuda rheology model, and the results were compared to those of the one-equation Spalart-Allmaras $RANS$ (Reynolds Averaged Navier–Stokes) model through a rectangular channel with a length of $5\pi D$ and a height of $2\pi D$ at the generalised Reynolds number of 3214.

Gavrilov and Rudyak (2016) [40] focused their studies on the development of a novel Reynolds-Averaged turbulence model for flows of Ostwald de Waele fluids. The fully developed turbulent pipe flows of power-law fluids were studied by Gavrilov and Rudyak (2016) [40] using direct numerical simulation at generalised Reynolds numbers of 10000 and 20000. Five different power-law indexes from 0.4 to 1 were considered. The adequate results from this investigation suggest that the fluid index decreases, the turbulent transfer of momentum and velocity fluctuations between the wall and the flow core decrease, while the turbulent energy flowing to the wall increases. Furthermore, the velocity of the power-law fluid shows an increase in the radial direction, resulting in the enhancement of apparent viscosity. The turbulence anisotropy becomes

more significant with the decreasing flow index.

New research and studies were carried out by Zheng et al. (2019) [43] to develop computational methods and DNS code better. According to Zheng et al. (2019) [43], the previous studies of shear-thinning fluids mainly use purpose-built codes and simple geometries. However, the geometries are more complex in the practical domain, and more flexible computational methods are required. Thus, a fully developed turbulent pipe flow of shear-thinning fluids was undertaken using direct numerical simulation to validate and verify the efficiency of the OpenFOAM library is assessed against a validated high-order spectral element-Fourier DNS code–Semtex. The emerging results of this investigation demonstrated that the predicted velocity and viscosity profiles are well resolved and predicted, while there was a notable difference in turbulence statistics. As it shall see, it was important to note that the different Reynolds turbulence intensities and stress profiles peak at 16% and 10%, corresponding to the Reynolds numbers 5000 and 7500, respectively.

Although non-Newtonian fluid flow is relevant in the engineering discussed above, there still needs to be more specifics in such a problem. To date, a relative need for studies treating DNS of turbulent flows of non-Newtonian fluid through cylindrical pipes. There has yet to be research the turbulent flow of Ostwald de Waele fluids through axially rotating pipes through DNS.

IV.2 Problem Description

The present work deals numerically with a fully developed turbulent flow of pseudoplastic ($n = 0.75$), dilatant ($n = 1.2$), and Newtonian ($n = 1$) fluids through a rotating cylindrical pipe over a rotation rate range of ($0 \leq N \leq 3$) at simulation Reynolds number of 5000 by using the DNS approach. The computational domain length was chosen to be in the streamwise direction (Figure IV.1).

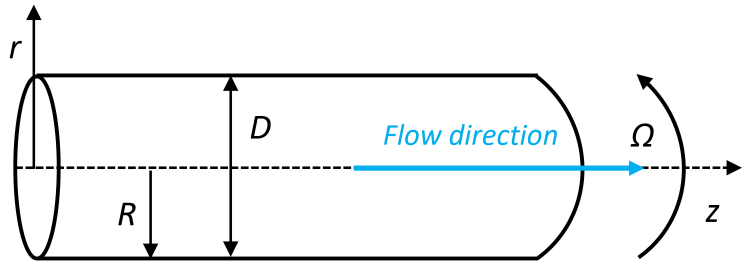

Figure IV.1 – Computational Domain.

IV.3 Mathematical Formulation

The conservation of mass and momentum equations govern the thermal flow of a non-Newtonian fluid are presented and written in dimension and dimensionless form as :

Continuity equation :

$$\frac{\partial {u_i}^*}{\partial x_j} = 0 \tag{IV.1}$$

Momentum equation :

$$\frac{\partial {u_j}^*}{\partial t^*} + \frac{\partial ({u_i}^* {u_j}^*)}{\partial {x_i}^*} + 2\varepsilon_{ijk}\Omega_j {u^*}_k = -\frac{1}{\rho}\frac{\partial p^*}{\partial {x_i}^*} + \frac{\partial}{\partial {x_i}^*}\left[\nu\left(\frac{\partial {u_i}^*}{\partial {x_j}^*} + \frac{\partial {u_j}^*}{\partial {x_i}^*}\right)\right] \tag{IV.2}$$

The filtered continuity and filtered momentum equations governing $3D$ incompressible non-Newtonian fluid are written in a cylindrical coordinate system and are made dimensionless. These equations are detailed in the mathematical formulations in CHAPTER 5.

IV.4 Results and Discussion

The present investigation tends to reveal the effects of the flow behaviour index and the swirl driven by the rotating pipe wall on the mean flow characteristics to shed further light on the laminarisation phenomenon and to provide an accurate, complete, and detailed description of the flow patterns and rheological behaviour of the Ostwald de Waele fluids along the radial coordinate, especially in the core region, where it is still difficult for experimental methods to get reliable data for certain variables, especially for rheological flows, despite improvements in experimental techniques. That is via analysing the effects of the rotation rate and the flow behaviour index of the Ostwald de Waele fluids on the streamwise velocity distribution along the radial coordinate and the generation and transport mechanism of the velocity fluctuations between the different turbulent layers. Moreover, the present investigation seeks also to ascertain the accuracy and reliability of the DNS laboratory code predicted results and to evaluate the reliability of the DNS approach to predict the main flow quantities and turbulence statistics of Ostwald de Waele fluid.

A Direct numerical simulation has been carried out to study the fully developed turbulent of pseudoplastic $(n = 0.75)$, Newtonian $(n = 1)$, and dilatant $(n = 1.2)$ through an isothermal axially rotation pipe at a simulation Reynolds number of 5000 and over a wide rotation rate range of $(0 \leq N \leq 3)$. The turbulent streamwise velocity and turbulence intensities of the streamwise velocity fluctuations are analysed and discussed in detail in the current chapter.

To ascertain the accuracy and reliability of the results, The emerged *DNS* predictions were validated by comparing the turbulent axial velocity of Newtonian fluid with those available in the literature in the following cases : The *LES* and *DNS* data of Ould-Rouiss et al. (2010) [30] and Abdi et al. (2019) [72] respectively. The Figure IV.2 compares the predicted profile of the turbulent axial velocity of a Newtonian fluid at simulation Reynolds number of 5000 with the *DNS* data performed by Ould-Rouiss et al. (2010) [30] and the *LES* of Abdi et al. (2019) [72] for generalised Reynolds and simulation Reynolds number of 5500 and 4500, respectively. As seen in Figure IV.2 no significant difference was observed between them, where the turbulent axial velocity collapsed very well with those of Ould-Rouiss et al. (2010) [30] and Abdi et al. (2019) [72] over the entire flow region. It should be noted that there is a little minor difference between numerical predictions (whether *LES* or *DNS*) and the difference in the Reynolds number and/or numerical methods.

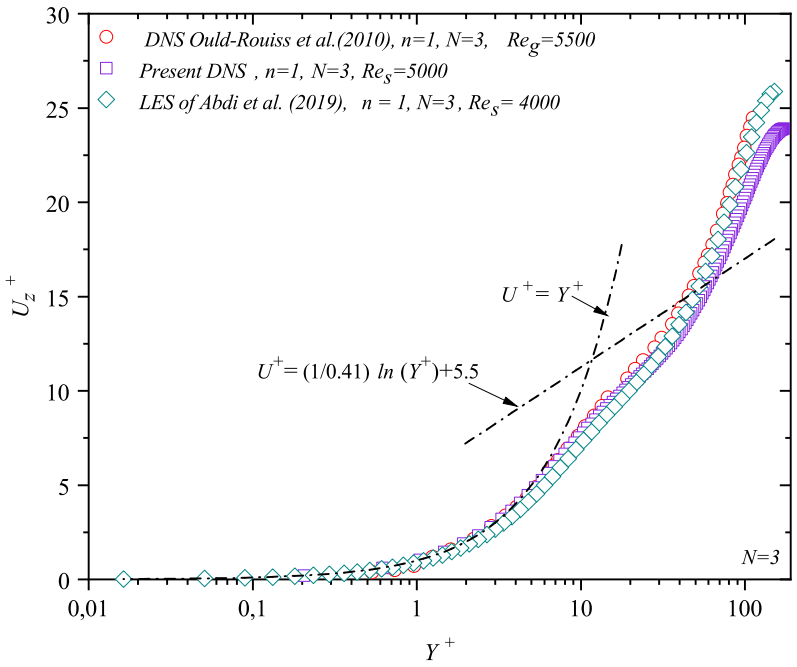

Figure IV.2 – Validation.

IV.4.1 Average velocity profiles

The current subsection tends to reveal the effects of the centrifugal force induced by the swirl driven by the rotating pipe wall on the mean flow pattern of the Ostwald de Waele fluids along the radial coordinate. As well as to critically evaluate the accuracy and effectiveness of the *DNS* technique to predict and provide more details of axial velocity distributions in the viscous sub-layer buffer region and logarithmic regions. Via critically analysing and discussing the turbulent streamwise velocity distributions of the pseudoplastic ($n = 0.75$), Newtonian ($n = 1$), and

dilatant ($n = 1.2$) fluids over a wide rotation rate range ($0 \leq N \leq 3$) at a simulation Reynolds number of 5000.

Figure IV.3 depicts the turbulent axial velocity profiles along the pipe radius (R), scaled by the friction velocity ($U_\tau = \sqrt{\tau_w/\rho}$) against the distance from the wall in wall units (Y^+). Furthermore, the dashed lines represent the universal velocity distributions in the viscous sub-layer ($0 \leq Y^+ \leq 5$) and the logarithmic layer ($30 \leq Y^+ \leq 200$).

As shown in Figure IV.3, the axial velocity profile is distributed linearly in the viscous sub-layer ; this velocity obeys the universal law ($U^+ = Y^+$) in the vicinity of the wall ($0 \leq Y^+ \leq 5$). The axial velocity of the pseudoplastic and dilatant increases gradually with the wall distance towards the core region.

It can be seen from Figure IV.3 that the hydrodynamic characteristics of the pseudoplastic and dilatant fluids are significantly affected by the rheological behaviour of the Ostwald de Waele fluids along the radial coordinate, especially outside the near-wall region. The flow behaviour index strongly influences the DNS streamwise velocity profiles of the power-law fluid over the viscous sub-layer buffer and logarithmic regions. As shown in Figure IV.3, the velocity profile of pseudoplastic fluid lies above the universal law in the logarithmic region. These notes align with those of previous studies Rudman (2004) [37], Gnambode et al. (2015) [47], and Gavrilov and Rudyak (2016) [40]. In contrast, the profile of the dilatant fluid lies down the universal law in the logarithmic region. It should be noted that the decreased flow behaviour index results in an enhancement in the turbulent axial velocity profile with the distance from the wall (Y^+) away from the wall towards the core flow region, where this trend is more pronounced in the logarithmic region for all rotation rates.

It is interesting to note that this discrepancy is due to the influence of the apparent viscosity and shear rate of the Ostwald de Waele fluid in this region, as pointed out by Abdi et al. (2019) [72] : the shear rate of shear-thinning fluid ($n = 0.75$) is higher than the dilatant one ($n = 1.2$) along the pipe radius, the increase in fluid's shear rate induces a noticeable increase in the movement of the fluid layers past each other away from the wall towards the core region with the wall distance, resulting a pronounced enhancement in the mean axial velocity along the pipe radius especially in the logarithmic layer and core region (Figure IV.3).

The predicted DNS profile of the streamwise velocity profile of the Newtonian fluid through stationary pipe collapses very well with the universal laws of $(U^+ = Y^+)$ and $(U^+ = 2.5 \ln Y^+ + 5.5)$ in the viscous sub-layer and logarithmic regions, respectively.

The streamwise velocity profiles of the pseudoplastic and dilatant seem independent of the rotation pipe wall effects in the vicinity of the pipe wall ; these profiles are almost identical in the near-wall region and are consistent with each other in the viscous sub-layer $(5 \leq Y^+)$ due to the limited effect of the centrifugal forces compared to the viscous force in the near-wall region.

The swirl driven by the rotating pipe wall considerably influences the hydrodynamic characteristics of the pseudoplastic and dilatant fluids outside the near-wall region. The streamwise velocity distributions depend strongly on the rotating pipe wall along the radial coordinate, especially at the pipe centre ; the swirl driven by the rotating pipe wall significantly influences the axial velocity distribution beyond the buffer region with the wall distance (Y^+). It should be noted that this discrepancy is due to the influence of the centrifugal force induced by the swirl driven by the rotating pipe wall on the shear rate of the pseudoplastic and dilatant fluids with the wall distance beyond the buffer region (transitional region). This discrepancy is attributed to radially growing centrifugal forces with the wall distance further away from the viscous sub-layer.

It can be seen from Figure IV.3 that the axial velocity profiles of the rotating pipe differ significantly from that of the stationary pipe outside the viscous sub-layer with the wall distance towards the logarithmic region ; the profiles of the rotating pipe lie down that of stationary pipe in the region $(10 \leq Y^+ \leq 100)$ for the pseudoplastic and dilatant. In contrast, the streamwise velocity profiles of the rotating pipe are somewhat higher than that of the stationary pipe beyond $(Y^+ = 100)$; the pipe wall rotation induces a pronounced decrease in the axial velocity of the pseudoplastic and dilatant fluids in the buffer region, resulting in a noticeable increase in the velocity in the core region, this trend is more pronounced as the rotation rate increases. As the pipe wall rotates, the apparent viscosity of the pseudoplastic and dilatant fluids reduces significantly in the logarithmic region, as pointed out by Abdi et al. (2019) [72], resulting in a marked increase in the streamwise velocity profile in the core region. This trend is more noticeable as the rotation rate increases, known as the laminarisation phenomenon.

It can be said that the radially growing centrifugal force induced by the swirl driven by the rotating pipe wall causes a supplemented force to the inertia force, which results in a noticeable reduction in the apparent fluid viscosity, resulting in a noticeable increase in the streamwise velocity of pseudoplastic and dilatant in the core region.

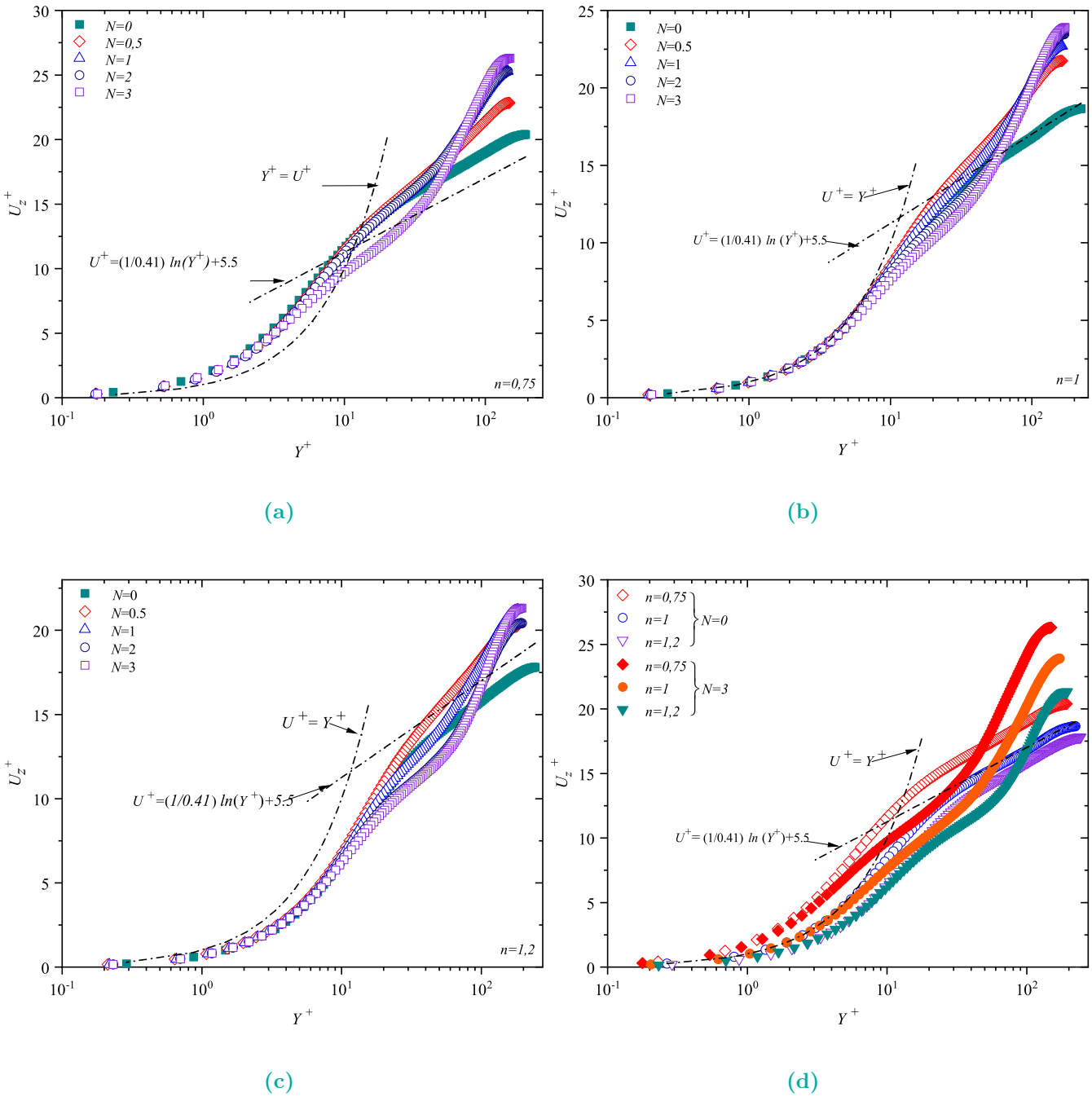

Figure IV.3 – Turbulent axial velocity profiles.

IV.4.2 Turbulent intensity

The current subsection seeks to highlight the effects of centrifugal force induced by the swirl driven by the rotating pipe wall and the flow behaviour index of Ostwald de Waele fluid on the turbulence feature and the generation and transport mechanism of turbulence intensities of the velocity fluctuation from the wall vicinity towards the core region.

Figure IV.4, Figure IV.5, and Figure IV.6 depict, respectively, the root mean square (RMS) distribution of the axial, radial and tangential velocity fluctuations of the pseudoplastic $(n = 0.75)$, Newtonian $(n = 1)$, and dilatant $(n = 0.1.2)$ fluids, scaled by the friction velocity $U_\tau = \sqrt{\tau_w/\rho}$ along the pipe radius (R), versus the distance from the wall in wall units (Y^+) at a simulation's Reynolds number of 5000 and over a rotation rate range of $(0 \leq N \leq 3)$.

Figure IV.4 shows that the turbulence intensities of the axial velocity fluctuations profiles exhibit the same trend along the pipe radius for all studied cases. In Figure IV.4, the RMS of the axial components of the pseudoplastic, Newtonian and dilatant fluids increase gradually with the wall distance in the viscous sub-layer. The axial turbulence intensities seem more affected by rotation rate, where these profiles differ significantly beyond the near-wall region. As shown in Figure IV.4, these profiles gradually increase and deviate from each other away from the near-wall towards the core region ; this deviation becomes more distinct with the distance from the wall (Y^+), especially in the buffer region. They drop rapidly and fall to lower values beyond approximately $(Y^+ = 35)$ for fluids all and rotation rates. This means that axial velocity fluctuations generated in the near-wall region and transported far away from the pipe wall to vanish near the pipe centre for all considered cases.

As shown in Figure IV.4 that the axial turbulence intensities profiles of the stationary pipe lie down those of the rotating pipe wall along the pipe radius for the pseudoplastic and dilatant fluids, especially in the buffer region ; this trend is evident as the pipe wall rotates. The RMS profiles reach their peak values, drop rapidly and fall to lower values in the logarithmic region. It can be said that the swirl caused by the rotating pipe wall results in a noticeable enhancement in the generation and transport mechanism of turbulence intensities of the axial velocity fluctuation from the wall vicinity towards the core region for the shear-thinning, Newtonian and shear-thickening fluids.

Figure IV.5 shows the turbulence intensities of the radial velocity fluctuations. These profiles are nearly linear and equal to zero value along the near-wall region $(Y^+ \leq 3)$ for the different

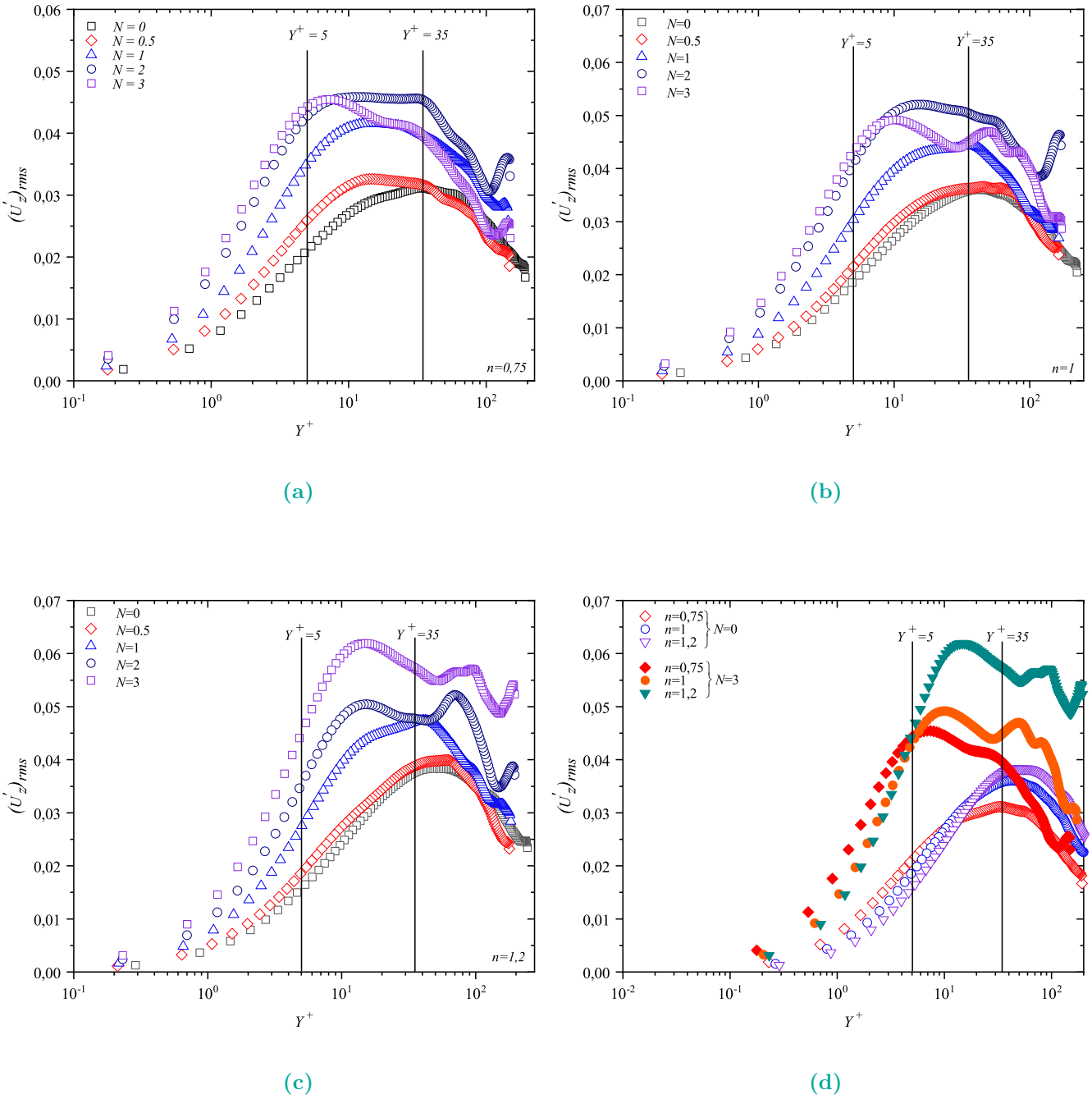

Figure IV.4 – Intensities of the axial velocity fluctuations.

fluids (0.75, 1 and 1.2) for all rotation rates ($0 \leq N \leq 3$). It can be said that the RMS of the radial component is almost independent of the rotation rate and flow behaviour index due to the absence of the generation of the axial velocity fluctuations in this near-wall region for all rotation rates.

The pseudoplastic, Newtonian, and dilatant profiles exhibit a significant enhancement further away from the wall towards the logarithmic region. In the buffer region $(5 \leq Y^+ \leq 35)$, these profiles increase significantly with wall distance for all rotation rates ; this increase is related to the increase in the turbulence generation of the axial velocity fluctuations in the buffer region for all rotation rates. Beyond $(Y^+ = 40)$, in the core region, the radial turbulence intensity profiles fell rapidly to lower values after reaching their maximum values due to the vanishing of axial velocity fluctuations.

Figure IV.5 shows that the radial turbulence intensities profiles of the stationary pipe lie down those of the rotating pipe wall in the viscous sub-layer for the three fluids. This trend is the same as in the buffer region of the shear-thinning and Newtonian fluids. Even though ; the rotation rate of dilatant fluid induces a decrease in peak value, the peak value in the stationary pipe is somewhat higher than the corresponding peak value in the rotating case. In the core region, they drop rapidly and fall to lower values beyond approximately $(Y^+ = 40)$ for all behaviour indices and rotation rates. It can be said that the increased rotation rate induces a pronounced enhancement in the transport mechanism of turbulence intensities of the radial velocity fluctuation from the axial velocity fluctuation.

Figure IV.6 illustrate the distribution of turbulence intensities of the tangential velocity fluctuations. These profiles had the same trend over the pipe radius for pseudoplastic, Newtonian and dilatant fluids and for all rotation rates. The RMS profiles of the tangential fluctuations are almost neglected in the near-wall region ; this is ascribed to the molecular shear stress being the dominant force compared to the turbulent one in the near-wall region. These profiles gradually increase and deviate from each other away from the near-wall region with the distance from the wall (Y^+). They drop rapidly and fall to lower values beyond approximately $(Y^+ = 35)$ for all flow behaviour indices and rotation rates.

The turbulence intensities of the tangential velocity fluctuations of the rotating pipe are consistent with those of the stationary pipe near the wall region. These profiles differ significantly from each other with the wall distance towards the buffer region for the shear-thinning, Newtonian and shear-thickening fluids, where the RMS profiles reach the peak, and the rotating pipe lies above those of the stationary pipe in the buffer region for all fluids. These profiles drop rapidly and fall to lower values in the core region. It can be said that the increased rotating pipe wall results in a pronounced reduction in the turbulence intensities of the tangential velocity fluctuations along the radial coordinates. This means that the increased rotation rate induces

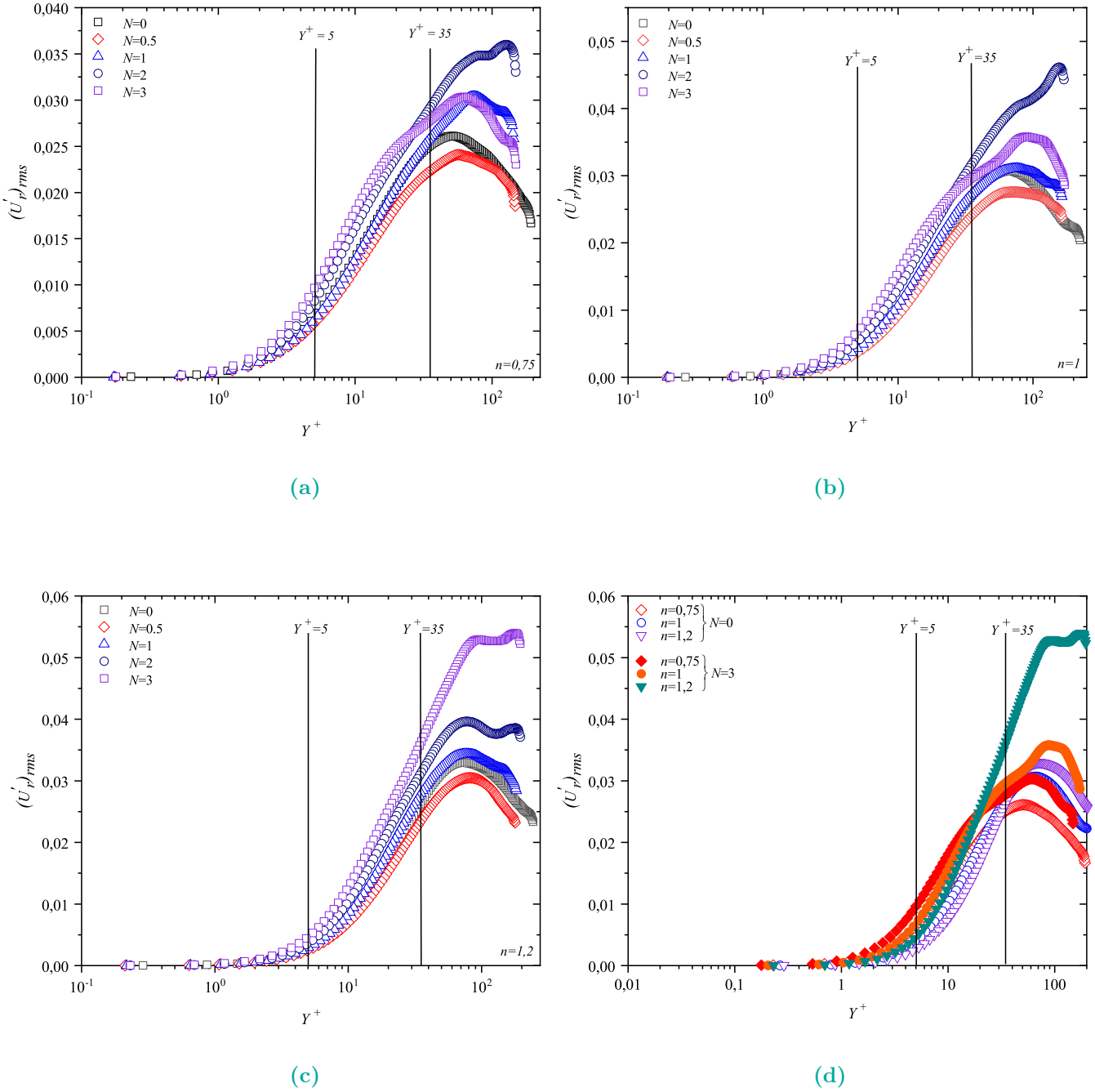

Figure IV.5 – Intensities of the radial velocity fluctuations.

a noticeable attenuation in the transport mechanism of turbulence intensities from the axial velocity fluctuation to the tangential ones of the pseudoplastic and dilatant fluids.

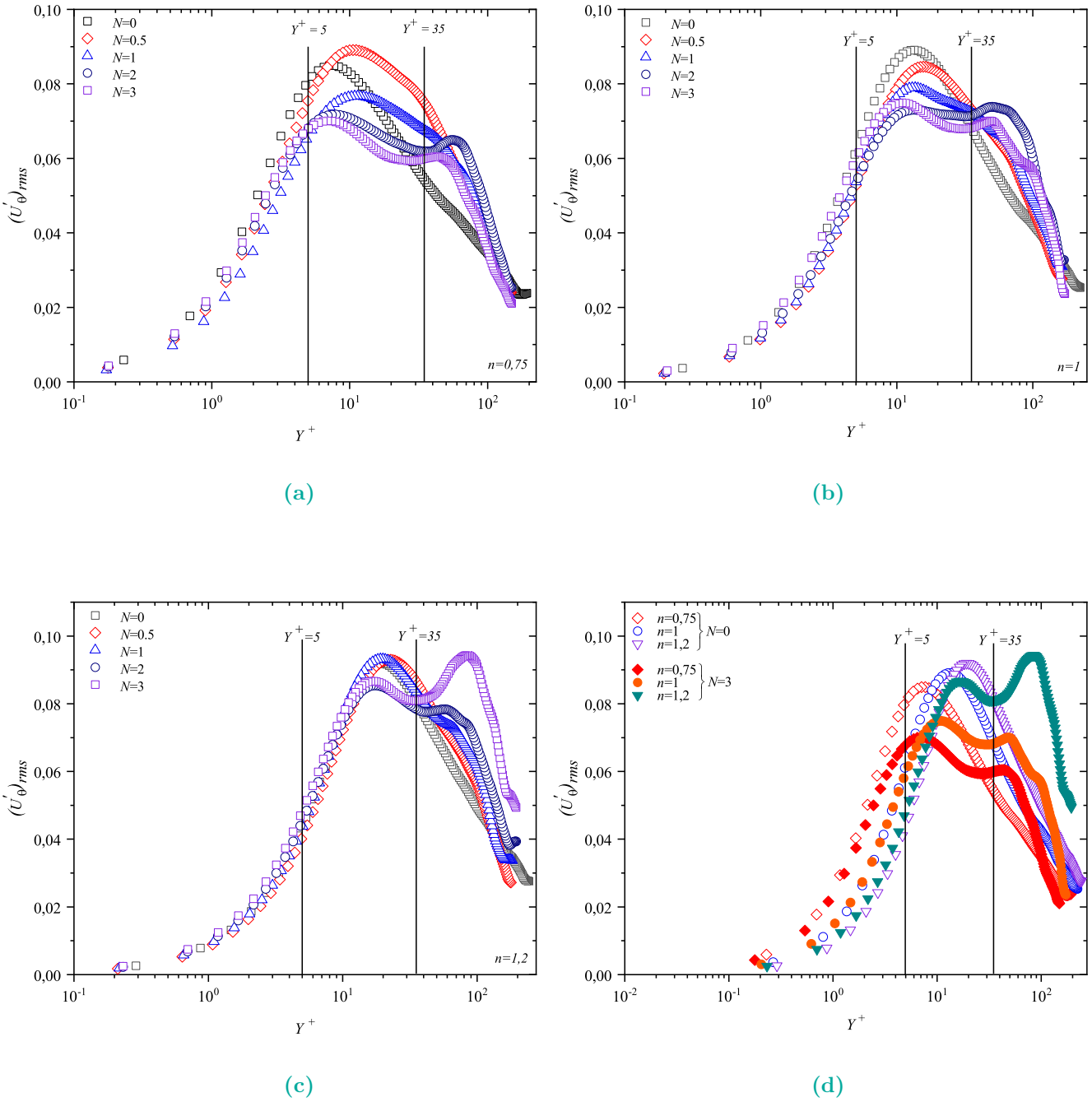

Figure IV.6 – Intensities of the tangential velocity fluctuations.

IV.5 Conclusion

The present investigation assessed to shed further light on the laminarisation phenomenon of Ostwald de Waele fluids by examining the effects of the centrifugal force induced by the swirl driven by the rotating pipe wall on the streamwise velocity distribution along the radial coordinate and the generation and transport mechanism of the velocity fluctuations between the different turbulent layers. Moreover, the present investigation seeks also to ascertain the

accuracy and reliability of the DNS laboratory code predicted results and to evaluate the reliability of the DNS approach to predict the main flow quantities and turbulence statistics of Ostwald de Waele fluid. The current study focused on the numerical analysis of a fully developed turbulent flow of pseudoplastic $(n = 0.75)$ and dilatant $(n = 1.2)$ fluids through an isothermal axially rotating pipe using the direct numerical simulation (DNS) at simulation Reynolds number $\mathrm{Re}_s = 5000$ over a rotation rate range of $(0 \leq N \leq 3)$. The finite difference scheme performed the numerical integration, second-order accuracy in space and time with a numerical resolution of $(129 \times 129 \times 193)$ gridpoints in axial, radial and circumferential directions. The governing equations were discretised on a staggered grid using cylindrical coordinates with a computational domain length of $20R$ in the axial direction.

The major conclusions of this research will be summarised :

- The swirl driven by the rotating pipe wall considerably influenced the hydrodynamic characteristics of the pseudoplastic and dilatant fluids outside the near-wall region. The streamwise velocity distributions depend strongly on the rotating pipe wall along the radial coordinate, especially at the pipe centre ; the swirl driven by the rotating pipe wall significantly influenced the axial velocity distribution beyond the buffer region with the wall distance (Y^+). The radially growing centrifugal force induced by the swirl driven by the rotating pipe wall caused a supplemented force to the inertia force, which resulted in a noticeable reduction in the apparent fluid viscosity and a noticeable increase in the streamwise velocity of pseudoplastic and dilatant in the core region.

- The radially growing centrifugal force resulted in a noticeable enhancement in the generation and transport mechanism of turbulence intensities of the axial velocity fluctuation from the wall vicinity towards the core region, and this trend was more pronounced as the rotation rate increased. The increased rotation rate also enhanced the transport mechanism of turbulence intensities of the radial velocity fluctuation from the axial velocity fluctuation. Moreover, the tangential turbulence intensities exhibited an obvious attenuation in the transport mechanism of turbulence intensities from the axial velocity fluctuation with increasing rotation rate for the pseudoplastic and dilatant fluids.

CHAPTER V

LES OF DILATANT FLUID

LES OF THERMALLY INDEPENDENT DILATANT FLUID

V

ABSTRACT

The present study aims to shed further light on the laminarisation phenomena of the Ostwald de Waele fluid by critically examining the effects of the centrifugal force induced by the swirl driven by the rotating pipe wall on rheological, hydrodynamic and thermal quantities, in addition to the turbulence characteristics. This study concerns a fully developed turbulent flow of thermally independent pseudoplastic $(n = 0.75)$ and dilatant $(n = 1.25)$ fluids through a heated axially cylindrical pipe, using a large eddy simulation (LES) approach with an extended Smagorinsky model. This investigation is conducted over a wide range of rotation rates $(0 \leq N \leq 3)$ at a simulation Reynolds number (Re_s) of 4500 and a simulation Prandtl number (Pr_s) of 1. Computations were based on a finite difference scheme, second-order accurate in space and time, with a numeric resolution of 65^3 gridpoints in axial, radial and circumferential directions, respectively, with a domain length of $20R$ in the axial direction. Uniform heat flux (q_w) was imposed on the wall as a thermal boundary condition. The emerging results suggest that the centrifugal force induced by the swirl driven by the rotating pipe wall causes a pronounced decrease in the shear rate profile of the pseudoplastic and dilatant fluids along the pipe radius, resulting in a marked increase in the axial velocity profile in the logarithmic region ; this trend is more pronounced as the rotation rate increases. The swirl driven by the rotating pipe wall results in an apparent attenuation in the generation and transport mechanism of turbulence intensities of the axial velocity fluctuation from the wall vicinity towards the core region for both flow behaviour indices, resulting in a pronounced attenuation in the turbulent kinetic energy further away from the pipe wall with the wall distance ; this trend is more pronounced as the rotation rate increases.

Keywords : LES, extended Smagorinsky, fully developed, turbulent flow, pseudoplastic, dilatant.

V.1 Introduction

The turbulence state of a fluid is one of the most challenging problems in fluid dynamics due to its importance in mechanical and engineering fields. It is often encountered in engineering applications such as heat exchangers, gas-cooled nuclear reactors and gas turbines, drilling hydraulics, sewage transport, nuclear reactors, and applications involving relatively high heat transfer rates. Swirl flow is crucial for many real-world mechanical and engineering applications and has a significant theoretical interest. The flow through rotating pipes is of great practical interest because of the various industrial applications and is often encountered in various furnaces and combustors, as well as in rotating machinery.

Several computational and experimental experiments have been carried out in recent years to understand the laminarisation phenomenon better and examine the impact of the rotating pipe wall on the mean flow characteristics and turbulence statistics. It is shown that the turbulent and hydrodynamic properties are influenced by the interaction between turbulence and the centrifugal force caused by the swirl. A body force that stabilises or destabilises the turbulence may also be inferred from the swirl produced by a rotating pipe wall's impact on the flow field and the practical significance of turbulent flows.

The effects of the swirl driven by a rotating pipe wall on flow characteristics and turbulent features for Newtonian fluids have been studied experimentally or numerically by [13], [14], [15], [16], [17]. The research Eggels et al. (1994) [16] performed one of the most important experimental and numerical analyses and discussions on turbulent pipe flow. Their findings suggest that the centrifugal force induced by the rotating pipe wall results in a pronounced attenuation of the normal wall and axial velocity fluctuation along the radial coordinates according to the Taylor-Proudman theorem because a rotating flow tends to become $2D$ in its plane of rotation. In addition, the attenuation of the shear stress also leads to a reduction of the friction factor.

Non-Newtonian fluids play a vital role in mechanical, technical applications and engineering fields nowadays, as well as in petroleum, cement, pharmaceutical, polymer and food processing, and an extensive range of applications. According to the last literature survey, non-Newtonian fluids through axial pipes have attracted much attention recently. These investigations focused on studying the rheological and hydrodynamic behaviours of this type of fluids either experimentally [32], [33], [34], [48], [49], [35], [23], [37], [39], [47], [40], [42].

The research of Metzner and co-workers (1955−1959) [32], [33], [34] remains to understand the rheological and hydrodynamic behaviour and flow of non-Newtonian fluids through a smooth pipe, they predicted the turbulent velocity profiles of non-Newtonian fluids, and they also derived a correlation for friction factor as a function of the generalised Reynolds number. On the other hand, Pinho and Whitelaw (1990) [35] carried out an experimental study of power-law (shear-thinning) fluids in a cylindrical pipe, measuring the axial velocity and the three normal stresses with four different concentrations chosen of a polymer (Sodium Carboxymethyl Cellulose) in an aqueous solution and with water in a range of Reynolds numbers from 240 to 111000.

Malin (1997) [23] employed a modified version of the Lam-Bremhorst $k-\varepsilon$ in his numerical investigation of Bingham, Ostwald de Waele, and Herschel-Bulkley fluids for different generalised Reynolds numbers, with various values of the power-law index (n).

Rudman et al. (2004) [37] applied a direct numerical simulation to pseudoplastic fluids over a wide range of flow behaviour indexes (n) 0.5, 0.69, 0.75, and Herschel-Bulkley $(n = 0.52)$ fluids has undertaken different generalised Reynolds number through a pipe using a spectral element-Fourier method. Rudman et al. (2004) [37] mentioned that the decrease of the flow behaviour index (n) induces a reduction in the friction factor, and their predicted friction factors are $10 - 15\%$ higher than the Dodge and Metzner correlations [34].

The convective heat transfer in swirling flows is often encountered in chemical and mechanical mixing and separation devices, electrical and turbo-machinery, combustion chambers, pollution control devices, swirl nozzles, rocketry, and fusion reactors. The utilisation of heat transfer with the turbulent swirling flow has often appeared in many mechanical and chemical engineering fields ; inlet part of fluid machinery, enhancement of mixing and chemical reaction in the combustion chamber. Some experimental and numerical literature works focused on the effects of the rotation rate on the fluid flowing inside the heated axially rotating pipe experimentally or numerically [21], [22], [36], [24], [26], [27], [28].

Satake and Kunugi [28] applied a direct numerical simulation for fully developed turbulent flow and heat transfer in axially rotating flow. The results show that the turbulent drag decreases with the rotating ratio increase ; the reason for this drag reduction can be considered as the additional rotational production terms that appear in the azimuthal turbulence component. The DNS and LES techniques of the fully developed forced convection heat transfer for airflow

through a heated axially rotating pipe were performed in 2010 by Ould-Rouiss et al. [30]. The rise in temperature variations toward the core of the pipe as the pipe rotates shows a clear tendency to increase the turbulence intensity of temperature fluctuations in the core flow zone. Additionally, as the spinning pipe diameter rises, the centrifugal force caused by the revolving pipe wall causes a noticeable decrease in the axial turbulent heat flow and an increase in the azimuthal heat flux.

The fully developed turbulent flow of non-Newtonian fluids through a smooth axial pipe is a problem of considerable significance and has received much attention in the past ; the literature contains several well-documented experimental and numerical investigations. These studies have given special consideration to describing this kind of fluid's rheological and hydrodynamic behaviour by revealing the effects of various rheological parameters on flow patterns and the turbulence features in such problems [35], [38], [39], [40].

Gnambode et al. (2015) [47] carried out a LES with an extended Smagorinsky model to study the turbulent flow of shear-thinning and thickening fluids through a pipe at various behaviour index $(0.5 \leq n \leq 1.4)$ and Reynolds numbers (4000, 8000 and 12000) and their effects on the rheological and turbulence characteristics. The results show that the decrease in the flow index results in a rise in axial and mean velocity profiles in the logarithmic region due to the higher viscosity in the pipe centre. Indeed, the same remark is noted for the apparent viscosity in this region and the importance of increasing the flow behaviour index. On the contrary, the apparent viscosity of the power-law fluids decreases along the centre region. Moreover, reducing the friction factor with the flow behaviour index leads to a noticeable enhancement in the Reynolds number for both shear-thinning and shear-thickening fluids.

Recently, Abdi et al. (2019) [50] studied the forced convection of a fully developed turbulent flow of the pseudoplastic $(n = 0.75)$ and Newtonian fluids through a heated axially rotating pipe using LES with an extended Smagorinsky model. The simulation Reynolds number and Prandtl number were assumed to be $\mathrm{Re}_s = 4000$ and $\mathrm{Pr}_s = 1$, respectively, with rotation rate (N) ranging from 0 to 3. This investigation aimed to explore the effects of the flow behaviour index of the shear-thinning fluids on the rheological properties, particularly the viscosity and shear rate of fluids. The results show that the decrease in the kinetic energy of turbulent fluctuations and the turbulent Reynolds shear stress of the axial-radial velocity fluctuations is due to the reduction in the RMS of the axial velocity fluctuations in the case of a rotating pipe. On the other hand, the turbulence intensities of the radial and tangential velocity fluctuations

marked enhancement in the rotating pipe wall. This trend is more evident as the rotation rate increases. In addition, the rotating pipe wall cause a significant decrease in the temperature distribution along the radial coordinates, and this trend is more pronounced when the rotation rate increases.

More recently, Abdi and co-workers (2023) [55] offered an extensive investigations of the turbulent flow of non-Newtonian fluids using the LES approach ; these investigations provided an important opportunity to advance the understanding of the rheological behaviour heat transfer mechanism on the non-Newtonian. Abdi and co-workers (2023) [55] employed the LES with an extended Smagorinsky model to investigate numerically the fully developed turbulent flow of Ostwald de Waele fluid through a straight cylindrical pipe with a length of the domain of $20R$ in the axial direction and a numerical resolution of 65^3gridpoints in the axial, radial, and circumferential directions. Their predicted findings results were in excellent agreement with those of experimental and DNS data available in the literature.

In recent decades, increasing attention and no study has been carried out on the turbulent flows of non-Newtonian fluids with related heat transfers through rotating cylindrical pipes. The current research aims to investigate the effects of turbulent and thermal properties. Toward this end, a large eddy simulation (LES) with a standard dynamic model was devoted to a fully developed turbulent flow of shear-thinning $(n = 0.75)$ and shear-thickening $(n = 1.25)$ fluids through a heated axially rotating pipe. This study was performed at a simulation's Reynolds and Prandtl numbers of 4500 and 1, respectively. The present investigation set out to reveal the effects of swirl driven by the rotating pipe wall on the turbulent and thermal statistics and to ascertain the accuracy and reliability of the LES predicted results of our code.

V.2 Problem Description

The present study focuses on the numerical investigation of a fully developed turbulent flow forced convection of non-thermo-dependent pseudoplastic $(n = 0.75)$, dilatant $(n = 1.25)$, and Newtonian $(n = 1)$ fluids through a heated axially rotating cylindrical pipe over a rotation rate range of $(0 \leq N \leq 3)$ at simulation's Reynolds and Prandtl numbers of 4500 and 1, respectively. The pipe wall is subjected to constant uniform heat flux (q_w) , where the computational domain length was chosen to be $20R$ in the streamwise direction.

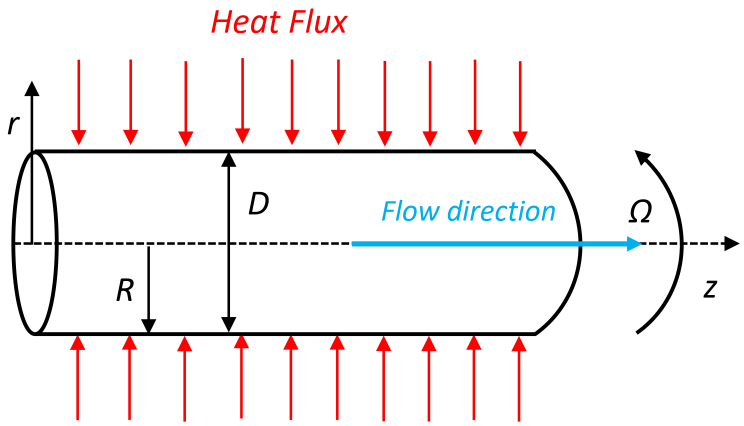

Figure V.1 – Computational Domain.

V.3 Mathematical Formulation

The conservation of mass and momentum equations govern the thermal flow of a non-Newtonian fluid are presented and written in dimension and dimensionless form as :

Continuity equation :

$$\frac{\partial u_i{}^*}{\partial x_j} = 0 \tag{V.1}$$

Momentum equation :

$$\frac{\partial u_j{}^*}{\partial t^*} + \frac{\partial (u_i{}^* u_j{}^*)}{\partial x_i{}^*} + 2\varepsilon_{ijk}\Omega_j u^*{}_k = -\frac{1}{\rho}\frac{\partial p^*}{\partial x_i{}^*} + \frac{\partial}{\partial x_i{}^*}\left[\nu\left(\frac{\partial u_i{}^*}{\partial x_j{}^*} + \frac{\partial u_j{}^*}{\partial x_i{}^*}\right)\right] \tag{V.2}$$

The notation with $(*)$ refers to dimensional quantities. The kinematic viscosity is determined from the Ostwald de Waele model defined by :

$$\eta = K\dot{\gamma}^{n-1} \text{ and } \nu = \eta/\rho \tag{V.3}$$

The filtered continuity V.1 and filtered momentum V.2 equations governing $3D$ incompressible Non-Newtonian fluid are written in a cylindrical coordinate system and are made dimensionless using the centreline axial velocity of the analytical fully developed laminar profile $(U_{CL} = (3n+1).U_b/(n+1))$ as a reference velocity where (U_b) is the average velocity, the pipe radius (R) as a reference length.

$$x = \frac{x^*}{R}\ y = \frac{y^*}{R} \text{ and } z = \frac{z^*}{R} \tag{V.4}$$

$$u = \frac{u^*}{U_{cL}} \tag{V.5}$$

$$p = \frac{p^*}{\rho U_{cL}} \tag{V.6}$$

$$t = \frac{t^*}{t_{ch}} \text{ where } t_{ch} = \frac{R}{U_{cL}},\ \dot{\gamma} = \frac{U_{cL}}{R}\dot{\gamma}^* \tag{V.7}$$

By introducing the dimensionless quantities defined above into equations V.1 and V.2, it becomes :

$$\frac{\partial u_i}{\partial x_i} = 0 \tag{V.8}$$

$$\frac{\partial u_j}{\partial t} + \frac{\partial (u_i u_j)}{\partial x_i} + 2\varepsilon_{ijk}\frac{\Omega_j R}{U_{CL}}u_k = \frac{\partial p}{\partial x_i} + \frac{1}{\mathrm{Re}_s}\frac{\partial}{\partial x_i}\left[\dot{\gamma}^{n-1}\left(\frac{\partial u_i}{\partial x_j} + \frac{\partial u_j}{\partial x_i}\right)\right] \tag{V.9}$$

Where $N_k = 2\Omega_j R/U_{CL}$ is defined as the rotation rate, and Ω_j is the rotational velocity of the pipe wall. Re_s is the Reynolds number of the simulations and is defined as :

$$\mathrm{Re}_s = \frac{\rho {U_{cL}}^{2-n} R^n}{K} \tag{V.10}$$

Where $\dot{\gamma}$, S_{ij} are the shear rate and the strain rate respectively,

$$\dot{\gamma} = \sqrt{2S_{ij}S_{ij}} \tag{V.11}$$

Equations V.8 and V.9 are filtered using a generic spatial average filter on a cylindrical control volume :

$$\overline{q}(r,\theta,z) = \frac{1}{r\Delta r\Delta\theta\Delta z}\iiint q(r',\theta',z')r'\Delta r'\Delta\theta'\Delta z' \tag{V.12}$$

The filtered equations are written as :

$$\frac{\partial \overline{u_i}}{\partial x_i} = 0 \tag{V.13}$$

$$\frac{\partial \bar{u}_j}{\partial t} + \frac{\partial \bar{u}_i\bar{u}_j}{\partial x_i} + 2\varepsilon_{ijk}\frac{\Omega_j R}{U_{CL}}u_k = -\frac{\partial \bar{p}}{\partial x_i} + \frac{1}{\mathrm{Re}_s}\frac{\partial}{\partial x_i}\left[\overline{\dot{\gamma}^{n-1}}\left(\frac{\partial \bar{u}_i}{\partial x_j} + \frac{\partial \bar{u}_j}{\partial x_i}\right) + \frac{\partial \bar{T}_{ij}}{\partial x_i}\right] - \frac{\partial \bar{\tau}_{ij}}{\partial x_i} \tag{V.14}$$

Where $\bar{\tau}_{ij} = \overline{q_i q_j} - \overline{q_i}\,\overline{q_j}$ is the sub-grid stress tensor and $\overline{T_{ij}} = \overline{\dot{\gamma}^{n-1}\frac{\partial q_i}{\partial x_j}} - \overline{\dot{\gamma}_{ij}^{n-1}\frac{\partial q_j}{\partial x_i}}$ is the additional sub-grid stress tensor for a non-Newtonian fluid. The above dimensionless equations V.10, V.11 and V.12 are written in cylindrical coordinate system are written with the following change of variables

$$q_r = rv_r,\ q_\theta = rv_\theta,\ q_z = v_z \tag{V.15}$$

This change of variables V.16, taken from the work of Verzicco and Orlandi (1996) [9], was chosen to avoid the singularity on the axis of the pipe $(r = 0)$. Explaining equations V.14 and V.15 in terms of the variables q_r, q_θ and q_z, it obtains :

$$\frac{\partial \bar{q}_r}{\partial r} + \frac{\partial \bar{q}_\theta}{\partial \theta} + r\frac{\partial \bar{q}_z}{\partial z} = 0 \tag{V.16}$$

$$\begin{aligned}\frac{D\bar{q}_z}{Dt} = \frac{\partial \bar{p}}{\partial z} + \frac{1}{\mathrm{Re}_s}\left[\frac{1}{r}\frac{\partial}{dr}\left(r\overline{\dot{\gamma}^{n-1}}\frac{\partial \bar{q}_z}{dr}\right) + \frac{1}{r^2}\frac{\partial}{d\theta}\left(r\overline{\dot{\gamma}^{n-1}}\frac{\partial \bar{q}_z}{d\theta}\right) + \frac{\partial}{\partial z}\left(r\overline{\dot{\gamma}^{n-1}}\frac{\partial \bar{q}_z}{dz}\right) + \right. \\ \left. \frac{1}{r}\frac{\partial}{\partial r}\left(r\overline{T_{rz}}\right) + \frac{1}{r^2}\frac{\partial \overline{T_{\theta z}}}{\partial \theta} + \frac{\partial \overline{T_{zz}}}{\partial z}\right] - \frac{1}{r}\frac{\partial \bar{\tau}_{rz}}{\partial r} - \frac{1}{r^2}\frac{\partial \bar{\tau}_{\theta z}}{\partial \theta} - \frac{\partial \bar{\tau}_{zz}}{\partial z}\end{aligned} \tag{V.17}$$

$$\begin{aligned}\frac{D\bar{q}_r}{Dt} = Nr\overline{q_\theta} - r\frac{\partial \bar{p}}{\partial r} + \frac{1}{\mathrm{Re}_s}\left[\frac{\partial}{dr}\left(r\overline{\dot{\gamma}^{n-1}}\frac{\partial \bar{q}_z/r}{dr} + \bar{T}_{rr}\right) - \left(\overline{\dot{\gamma}^{n-1}}\frac{\partial \bar{q}_r}{r^2} + \bar{T}_r\right) - \frac{2}{r^2}\left(\overline{\dot{\gamma}^{n-1}}\frac{\partial \bar{q}_\theta}{d\theta} + \bar{T}_{\theta\theta}\right)\right. \\ \left. + \frac{1}{r^2}\frac{\partial}{\partial \theta}\left(\overline{\dot{\gamma}^{n-1}}\frac{\partial \bar{q}_r}{d\theta} + \bar{T}_{\theta r}\right) + \frac{\partial}{\partial z}\left(\overline{\dot{\gamma}^{n-1}}\frac{\partial \bar{q}_r}{dr} + \bar{T}_{zr}\right)\right] - \frac{\partial}{\partial r}\left(\frac{\partial \bar{\tau}_{rr}}{r}\right) - \frac{\partial \bar{\tau}_{\theta r}}{\partial \theta} - \frac{\partial \bar{\tau}_{rz}}{\partial z} + \frac{\partial \bar{\tau}_{\theta\theta}}{r^2}\end{aligned} \tag{V.18}$$

$$\begin{aligned}\frac{D\bar{q}_\theta}{Dt} = -N\overline{q_r} - \frac{\partial \bar{p}}{\partial \theta} + \frac{1}{\mathrm{Re}_s}\left[\frac{\partial}{dr}\left(r\overline{\dot{\gamma}^{n-1}}\frac{\partial \bar{q}_\theta/r}{dr} + \bar{T}_{r\theta}\right) - \left(\overline{\dot{\gamma}^{n-1}}\frac{\partial \bar{q}_\theta}{r^2} + \bar{T}_\theta\right) + \right. \\ \left. \frac{1}{r^2}\frac{\partial}{\partial \theta}\left(\overline{\dot{\gamma}^{n-1}}\frac{\partial \bar{q}_\theta}{d\theta} + \bar{T}_{\theta\theta}\right) + \frac{\partial}{\partial z}\left(\overline{\dot{\gamma}^{n-1}}\frac{\partial \bar{q}_\theta}{dz} + \bar{T}_{z\theta}\right) + \frac{2}{r^2}\left(\overline{\dot{\gamma}^{n-1}}\frac{\partial \bar{q}_r}{d\theta} + \bar{T}_{\theta r}\right)\right] \\ - \frac{\partial}{\partial r}\left(\frac{\partial \bar{\tau}_{r\theta}}{r}\right) - \frac{1}{r^2}\frac{\partial \bar{\tau}_{\theta\theta}}{\partial \theta} - \frac{\partial \bar{\tau}_{\theta z}}{\partial z} - \frac{\partial \bar{\tau}_{\theta r}}{r}\end{aligned} \tag{V.19}$$

The energy equation as well as the thermal boundary conditions of the non-Newtonian fluid flow with heat transfer, this energy equation in tensor form in cylindrical coordinates, is written :

$$\frac{\partial T}{\partial t} + v_r\frac{\partial T}{\partial r} + \frac{v_\theta}{r}\frac{\partial T}{\partial \theta} + v_z\frac{\partial T}{\partial z} = \alpha\left[\frac{\partial^2 T}{\partial r^2} + \frac{1}{r}\frac{\partial T}{\partial r} + \frac{1}{r^2}\frac{\partial^2 T}{\partial \theta^2} + \frac{\partial^2 T}{\partial z^2}\right] \tag{V.20}$$

Where α is the thermal diffusivity of the fluid is considered constant and independent of shear and temperature. This is because variations in thermal diffusivity with temperature or shear rate are small compared to those of viscosity.

A heat flux density is imposed on the wall. This heat flux density condition requires that the wall temperature averaged in the azimuthal direction (θ) increases linearly in the flow direction (z).

The energy Equation V.20 of the non-Newtonian fluid is made dimensionless using the reference temperature, $T_{ref} = q_w/\rho C_p U_{CL}$. The dimensionless temperature is defined as :

$$\Theta = \left(\langle T_p\left(z\right)\rangle - T\left(\theta, r, z, t\right)\right)/T_{ref} \tag{V.21}$$

T_{ref} presents the reference temperature and is defined as $T_{ref} = q_w/\rho C_p U_{CL}$, where T_p is the pipe wall temperature and $\langle T_p\,(z)\rangle$ is an average in time and periodic directions. U_{CL} is the centreline axial velocity of the analytical fully developed laminar profile and defined as $U_{CL} = (3n+1)\,.U_b/(n+1)$.

Using the definition of temperature (given by Equation V.21), the dimensionless form of the energy equation is as follows :

$$\frac{\partial\Theta}{\partial t} + \frac{1}{r}\frac{\partial}{\partial r}\left(q_r\Theta\right) + \frac{1}{r}\frac{\partial}{\partial\theta}\left(q_\theta\Theta\right) + \frac{\partial}{\partial z}\left(q_z\Theta\right) - q_z\frac{\partial}{\partial z}\left(\frac{T_P}{T_{ref}}\right) = \frac{1}{\mathrm{Re_s Pr_s}} \left[\frac{1}{r}\frac{\partial}{\partial r}\left(r\frac{\partial\Theta}{\partial r}\right) + \frac{1}{r^2}\frac{\partial^2\Theta}{\partial\theta^2} + \frac{\partial^2\Theta}{\partial z^2}\right] \tag{V.22}$$

By filtering Equation V.22, the filtered energy equation is written :

$$\frac{\partial\bar{\Theta}}{\partial t} + \frac{1}{r}\frac{\partial}{\partial r}\left(\bar{q}_r\bar{\Theta}\right) + \frac{1}{r}\frac{\partial}{\partial\theta}\left(\bar{q}_\theta\bar{\Theta}\right) + \frac{\partial}{\partial z}\left(\bar{q}_z\bar{\Theta}\right) - \bar{q}_z\frac{\partial}{\partial z}\left(\frac{T_P}{T_{ref}}\right) = \frac{1}{\mathrm{Re_s Pr_s}} \left[\frac{1}{r}\frac{\partial}{\partial r}\left(r\frac{\partial\bar{\Theta}}{\partial r}\right) + \frac{1}{r^2}\frac{\partial^2\bar{\Theta}}{\partial\theta^2} + \frac{\partial^2\bar{\Theta}}{\partial z^2}\right] - \frac{1}{r}\frac{\partial\bar{\tau}_{\Theta r}}{\partial r} - \frac{1}{r}\frac{\partial\bar{\tau}_{\Theta\theta}}{\partial r} - \frac{1}{r}\frac{\partial\bar{\tau}_{\Theta z}}{\partial r} \tag{V.23}$$

Where the sub-grid terms or sub-grid heat fluxes are defined by :

$$\bar{\tau}_{r\Theta} = \overline{q_r\Theta} - \bar{q}_r\bar{\Theta}, \bar{\tau}_{\theta\Theta} = \overline{q_\theta\Theta} - \bar{q}_\theta\bar{\Theta}, \bar{\tau}_{z\Theta} = \overline{q_z\Theta} - \bar{q}_z\bar{\Theta} \tag{V.24}$$

The simulation Prandtl number is given by :

$$\mathrm{Pr}_s = \frac{K}{\alpha\rho R^{n-1}{U_{CL}}^{1-n}} \tag{V.25}$$

With K the consistency at temperature $\langle T_P\rangle$. In Equation V.23, the tensors $\bar{\tau}_{r\Theta}$, $\bar{\tau}_{\theta\,\Theta}$ and $\bar{\tau}_{z\Theta}$ are the sub-grid heat flux tensors.

The details of equations is mentioned in [72] and [73].

V.4 Results and Discussion

V.4.1 Rheological and Hydrodynamic Behaviours of Ostwald De Waele Fluid

The accuracy and reliability of the predicted results and the reliability and accuracy of the *LES* code laboratory have been ascertained and confirmed decisively by comparing the current prediction findings to those found in the literature. The results of the fully developed turbulent flow of shear-thinning and Newtonian fluid across stationary and rotating pipes have been compared reasonably well with those of the experimental and *DNS* data available in the literature Figure V.2 and Figure V.3.

Figure V.2a compares the turbulent axial velocity profiles of the shear-thinning ($n = 0.75$) fluid through a stationary ($N = 0$) with *LES* of Abdi et al. (2019) [50] at the simulation Reynolds number of 4000, *DNS* and experimental data of Rudman et al. (2004) [37] for a generalised Reynolds number and Reynolds of Metzner and Reed of 7027 and 3935, respectively. As shown in Figure V.2a , the predicted turbulent axial velocity profiles are in excellent agreement with those of Abdi et al. (2019) [50] and Rudman et al. (2004) [37] over the pipe radius. It can be seen from Figure V.2a that no significant differences were found between the predicted profile and those of Abdi et al. (2019) [50] and Rudman et al. (2004) [37] ; these profiles are consistent very well with the compared results over the three layers.

Figure V.2b reasonably compares the turbulent axial velocity profiles of the Newtonian ($n = 1$) fluid through an axially rotating pipe ($N = 1$ and $N = 3$) with the *LES* of Abdi et al. (2019) [50] at the simulation Reynolds number of 4000, experimental of Eggels (1994) [16], *DNS* of Redjem et al. (2007) [29] and *DNS* of Ould-Rouiss et al. (2010) [30] at Reynolds number equals to 5500. It can be seen in Figure V.2b that there is no noteworthy discrepancy between the present streamwise velocity profile and those of the literature. The predicted velocity distribution of the Newtonian profiles is in excellent agreement with the universal linear law ($U^+ = Y^+$) and universal logarithmic law ($U^+ = 2.5 \ln Y^+ + 5.5$) over the viscous sub-layer and logarithmic layer, respectively. It should be noted that there is a little minor difference between numerical predictions (whether *LES* or *DNS*) and the difference in the Reynolds number and/or numerical methods.

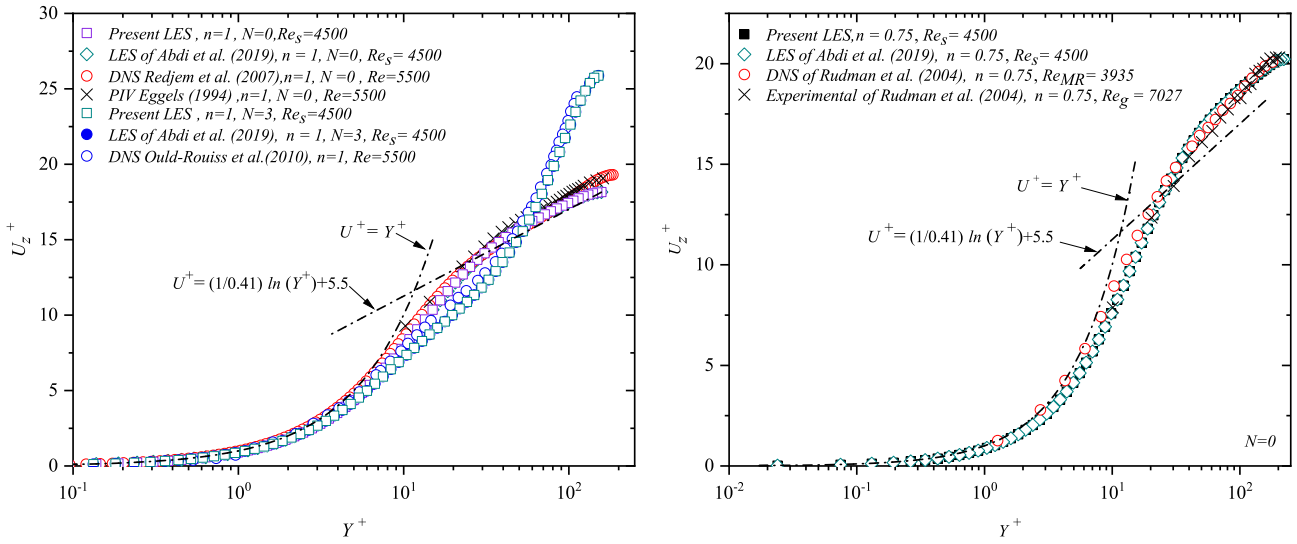

Figure V.2 – Validation of turbulent Axial velocity profiles.

Figure V.3 compares the mean axial velocity distribution of the Newtonian fluid with the rotation rate of 0, 1 and 3, with those of Abdi et al. (2019) [50] at the simulation Reynolds number of 4000, experimental data of Reich and Beer (1988) [20] at Reynolds number of 5000, and *DNS* data of Ould-Rouiss et al. (2010) [30] at a Reynolds number of 5500. As shown in Figure V.3, there is a good agreement between the predicted velocity profiles and those of the literature over the entire pipe radius with a little difference. It should be noted here that this marked discrepancy may be due to the difference in the Reynolds number value and the numerical solution procedure.

Figure V.4 compares the normalised root mean square (*RMS*) of the axial, radial and tangential velocity fluctuations of the shear-thinning ($n = 0.75$) and Newtonian fluids along the pipe radius for the stationary pipe. These profiles have been compared reasonably with the *LES* of Abdi et al. (2019) [50] at the simulation Reynolds number of 4000 and the *DNS* of Redjem et al. (2007) [29] at a Reynolds number equal to 5500.

As shown in Figure V.4a, the predicted *RMS* profiles of the shear-thinning are in excellent agreement with those of Abdi et al. (2019) [50] along the pipe radius. It can be seen from Figure V.4b that a reasonable agreement between the Newtonian predicted axial, tangential velocity fluctuations and those of Abdi et al. (2019) [50] and the *DNS* of Redjem et al. (2007) [29]

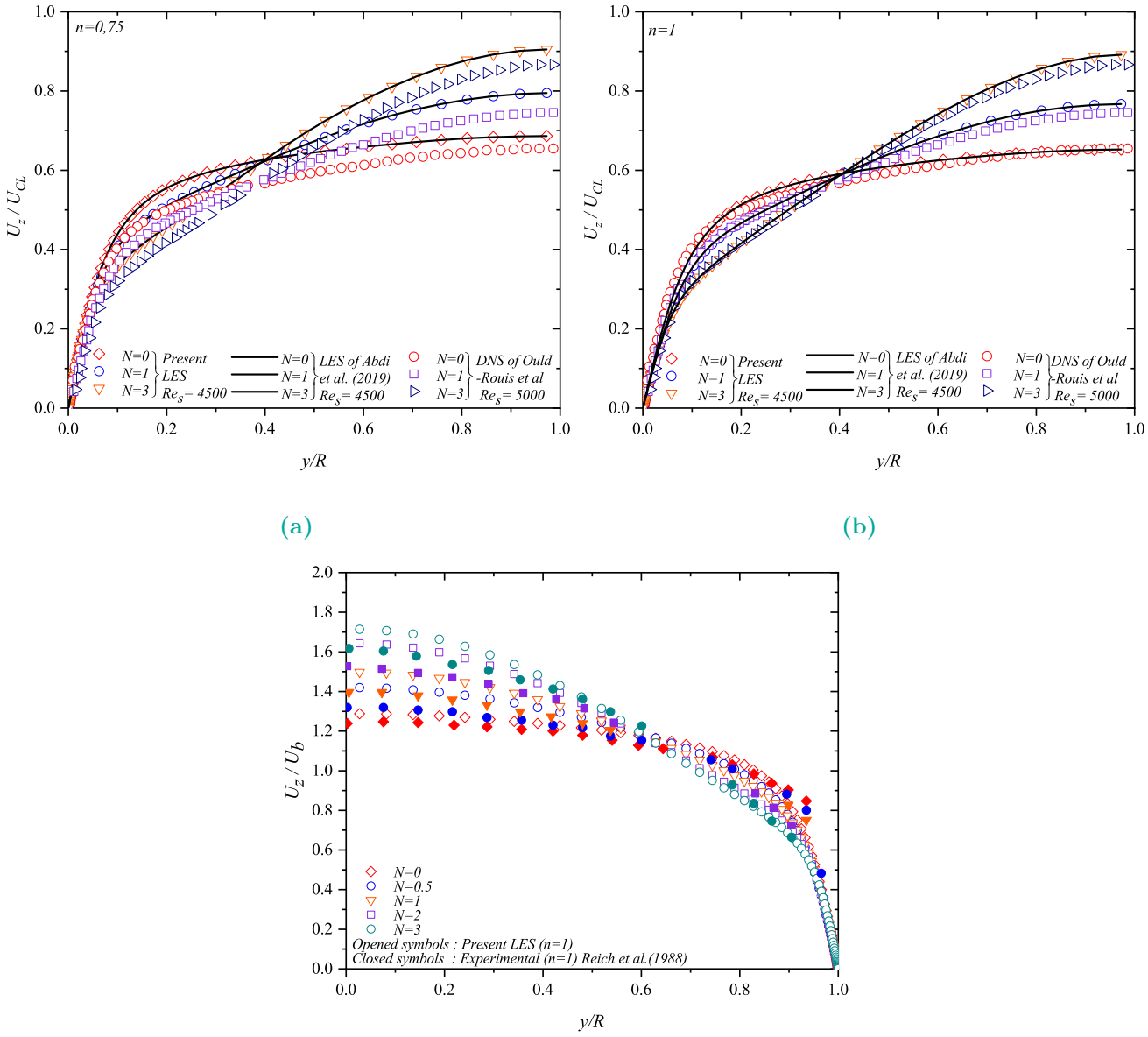

Figure V.3 – Validation of mean axial velocity profiles.

along the pipe radius. As shown in V.4b, a little difference is observed between the predicted profiles of the radial and tangential velocity fluctuations and those of the *DNS* of Redjem et al. (2007) [29] in the core flow region ; this marked discrepancy may be due to the difference in the Reynolds number value and the numerical solution procedure.

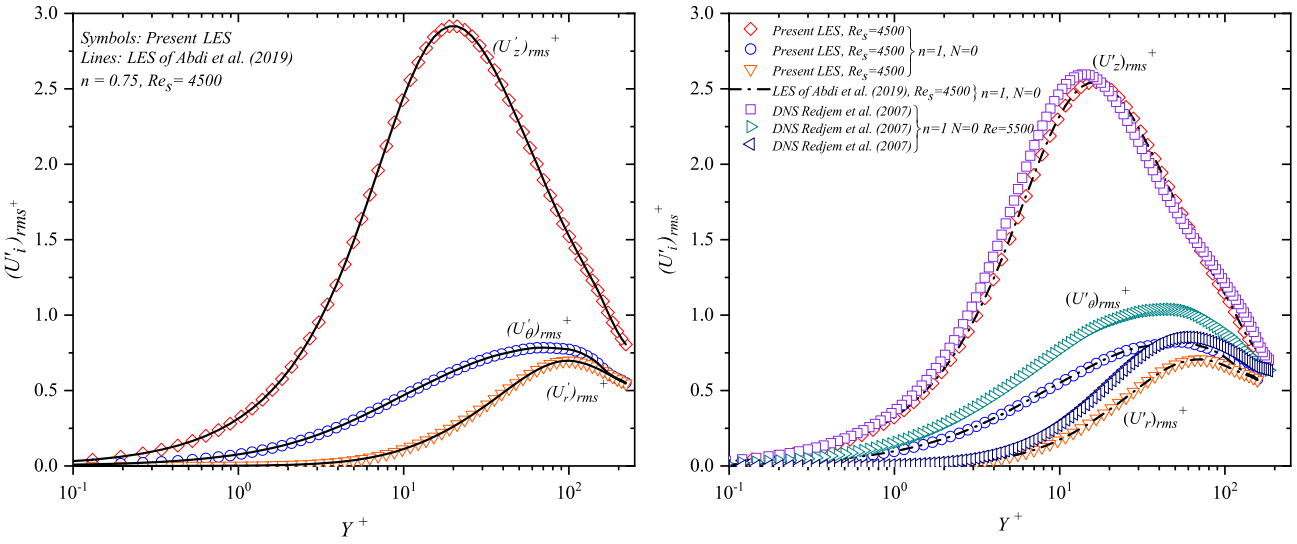

(a) (b)

Figure V.4 – Validation of Root mean square.

V.4.1.1 Shear rate and apparent viscosity

The present subsection aims to shed light on the effects of the swirl driven by a rotating pipe wall and the flow behaviour index on the rheological behaviour of the pseudoplastic and dilatant fluids. The following paragraphs analyse and discuss various rheological properties, such as apparent fluid viscosity and shear rate.

Figure V.5 illustrates the normalised shear rate and apparent viscosity distributions of the pseudoplastic $(n = 0.75)$, Newtonian $(n = 1)$, and dilatant $(n = 1.25)$ fluids along the pipe radius (R) at a simulation Reynolds (Re_s) number equals to 4500 and over a rotation rate range of $(0 \leq N \leq 3)$. It can be seen from Figure V.5 that the shear rate is nearly linear and remains constant along the viscous sub-layer $(0 \leq Y^+ \leq 5)$, for all rotation rates and flow behaviour indices. The shear rate profiles begin to decrease gradually with the distance from the wall far away from the near-wall region towards the logarithmic region, where this reduction is sharped in the buffer region $(5 \leq Y^+ \leq 30)$, for all cases. As shown in Figure V.5, the rotating pipe wall affects significantly the shear rate distributions of both fluids in the viscous sub-layer $(0 \leq Y^+ \leq 5)$, the shear rate profiles of non-rotating pipe lie above those of rotating one along the pipe radius. It can be said that the increased rotation rate (N) induces a pronounced increase in the shear rate for dilatant fluids. As shown in Figure V.5, the effect of the flow behaviour index on the shear rate is more significant in the near-wall region, where the shear-thinning

profiles lie above those of the shear-thickening along the near-wall region, for all rotation rates. It can be said that the decreased flow behaviour index results in a marked increase in the shear rate distributions over the vicinity of the pipe wall.

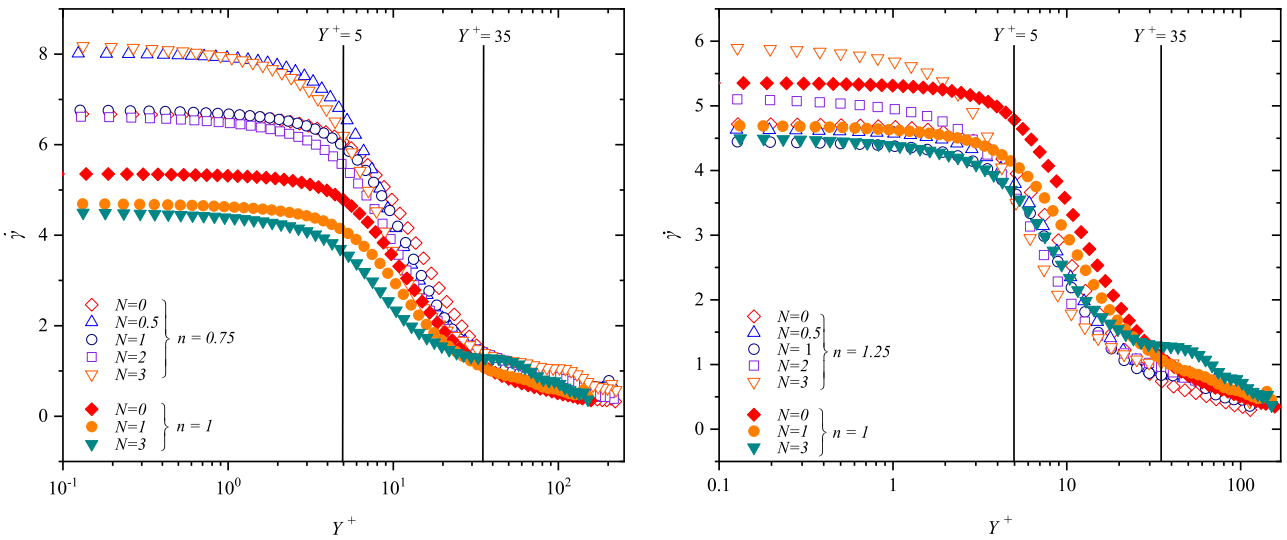

Figure V.5 – Shear rate profiles.

Figure V.6 presents the distribution of the apparent viscosity of the shear-thinning $(n = 0.75)$, Newtonian $(n = 1)$ and shear-thickening $(n = 1.25)$ fluids. It is apparent that in Figure V.6 the apparent viscosity profiles of the shear-thinning, shear-thickening, and Newtonian fluids are linear and equal to the apparent viscosity in the near-wall region for all rotation rates. Beyond the buffer region $(Y^+ > 5)$,the apparent viscosity profiles begin to increase gradually far away from the pipe wall towards the core flow region with the distance from the wall (Y^+), where the shear-thinning fluid becomes more viscous in the buffer $(5 \leq Y^+ \leq 30)$ and logarithmic $(30 \leq Y^+ \leq 200)$ regions.

The apparent viscosity of the shear-thickening fluid lies above the Newtonian fluid near the pipe wall. For the dilatant fluid, the apparent viscosity drops gradually with the distance from the wall far away from the near-wall region towards the logarithmic region for all rotation rates. As shown in Figure V.6, the rotation rate significantly affects the apparent viscosity over the three regions (sub-layer, buffer, and logarithmic), where this effect is more pronounced near the pipe wall. The apparent viscosity profiles of the rotating pipe lie down that of the stationary one

along the pipe radius. The apparent viscosity of shear-thickening reduces significantly when the pipe wall rotates. This decrease in the viscosity is more obvious as the rotation rate increases, especially in the sub-layer.

For the pseudoplastic fluid, the apparent viscosity seems independent of the rotation rate in the near-wall region. The viscosity profiles are identical and equal to the apparent viscosity at the pipe wall (η_w) over the viscous sub-layer $(0 \leq Y^+ \leq 5)$, for all rotation rates. The apparent viscosity profiles are consistent with each other in the vicinity of the pipe wall, where it is apparent that no significant noteworthy differences were found between them over the sub-layer and buffer regions. As shown in Figure V.6, the apparent viscosity profiles begin to deviate from each other only beyond $(Y^+ = 35)$ towards the core region ; this deviation becomes more distinct with the distance from the wall (Y^+), especially in the logarithmic region. As shown in Figure V.6, the shear rate decreases gradually with the wall distance far away from the pipe wall towards the core region ; this reduction results in a gradual increase in the apparent viscosity of the pseudoplastic fluid beyond the sub-layer region where the pseudoplastic fluid tends to behave like a solid when approaching to the pipe centre. On the contrary, the decreased shear rate far away from the vicinity of the wall induces a marked decrease in the apparent viscosity of the dilatant fluid with the wall distance towards the logarithmic region.

The apparent viscosity profiles of the rotating pipe lie down that of the stationary one along the logarithmic region, where this trend is more pronounced as the rotation rate increases. The increased rotation rate results in a marked reduction in the apparent fluid viscosity of the pseudoplastic in the logarithmic region.

The Figure V.7 presents the distribution of apparent fluid viscosity normalised by viscosity at the wall (η_w), against the shear rate scaled by the shear rate at the pipe wall $(\dot{\gamma}_w)$. As seen in Figure V.7, the apparent viscosity of the Newtonian fluid is constant linear and equal to the apparent viscosity along the pipe radius, which means the Newtonian apparent viscosity is independent of the shear flow rate.

The apparent viscosity of the shear-thinning and shear-thickening fluids is not constant, which is a function of the shear rate, where the apparent viscosity varies with the shear rate along the pipe radius. As shown in Figure V.7, the apparent viscosity of the pseudoplastic fluid decreases gradually with the shear rate ; the apparent viscosity of the pseudoplastic fluid is inversely proportional to the shear rate : as the shear rate increases as the apparent viscosity decreases considerably for all rotation rates. It should also be noted that this finding confirms the

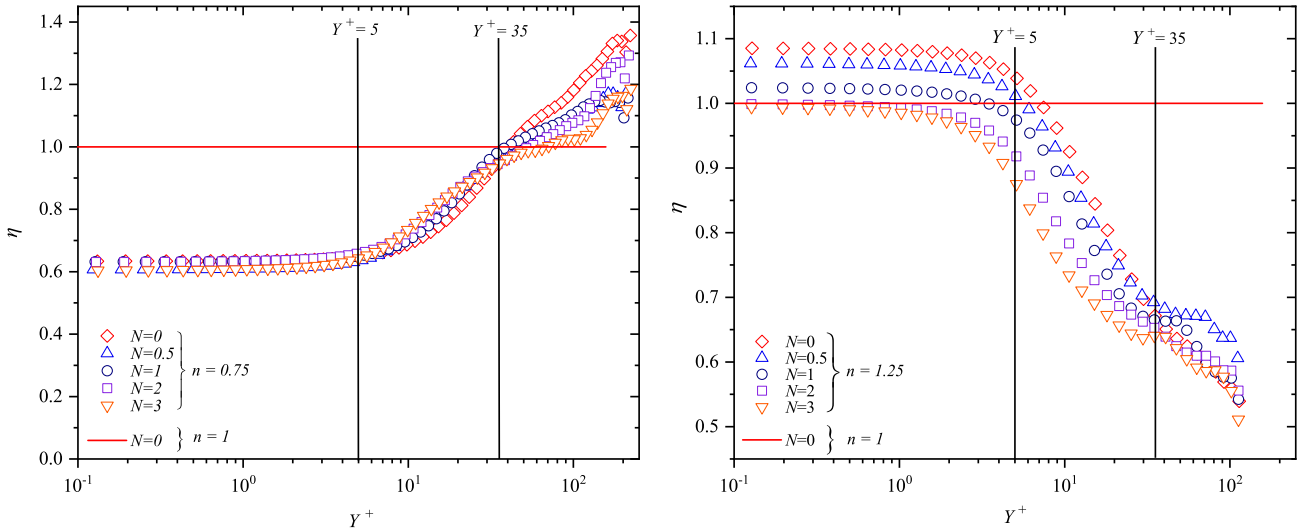

(a) (b)

Figure V.6 – Apparent viscosity profiles.

association between the apparent fluid viscosity and the shear rate of the power-law fluids where $\eta = K\dot{\gamma}^{n-1}$. On the contrary, the apparent viscosity of the dilatant fluid increases gradually with the shear rate, and the apparent viscosity of the dilatant fluid is directly proportional to the shear rate : as the shear rate increases the apparent viscosity increases significantly for all rotation rates. It should also be noted that this finding confirms the association between the apparent fluid viscosity and the shear rate of the pseudoplastic and dilatant fluids where $\eta = K\dot{\gamma}^{n-1}$.

V.4.1.2 Average velocity profiles

The present subsection aims to shed further light on the laminarisation phenomena of the power-law fluid, that by critically examining the effects of the centrifugal force induced by the swirl driven by the rotating pipe wall in addition to the effects of flow behaviour index on hydrodynamic and the turbulence characteristics, especially in the vicinity of the wall. Via analysing and discussing the effects of the rotation rate (N) and flow behaviour index (n) on the distribution of the turbulent axial velocity, mean axial velocity, and tangential velocity of the pseudoplastic $(n = 0.75)$, Newtonian $(n = 1)$, and dilatant $(n = 1.25)$ fluids at a simulation Reynolds number of over a rotation rate range of $(0 \leq N \leq 3)$.

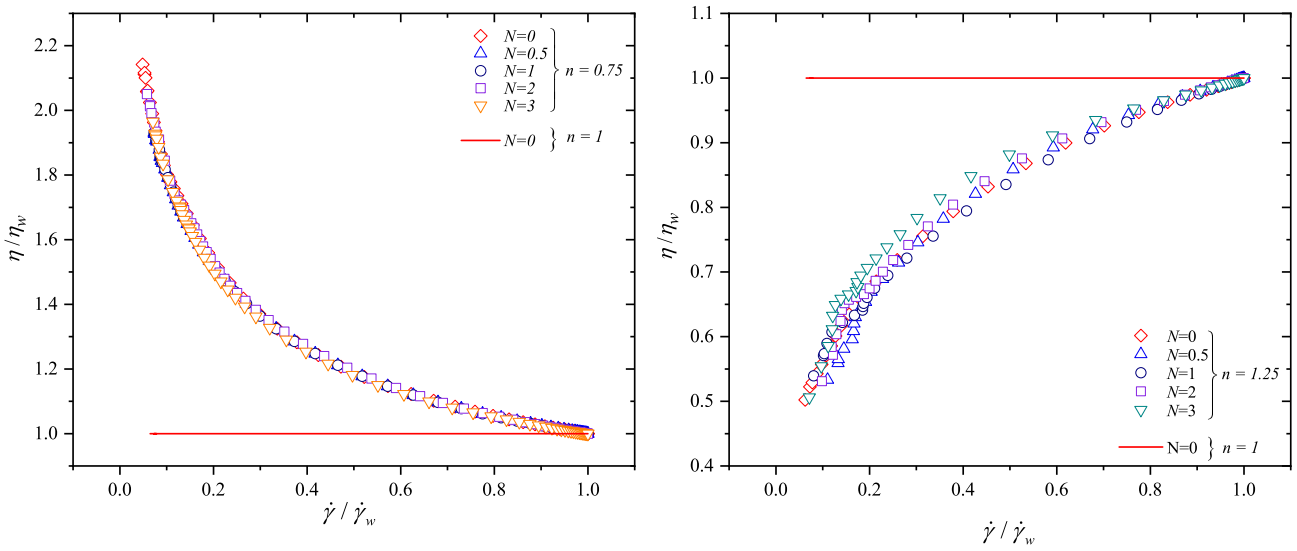

(a) **(b)**

Figure V.7 – Apparent viscosity against the shear rate profiles.

Figure V.8, illustrates the turbulent axial velocity profiles along the pipe radius , scaled by the friction velocity $(U_\tau = \sqrt{\tau_w/\rho})$ against the distance from the wall in wall units (Y^+). The dashed lines represent the universal velocity distributions in the viscous sub-layer $(0 \leq Y^+ \leq 5)$ and the logarithmic layer $(30 \leq Y^+ \leq 200)$.

The turbulent axial velocity strongly depends on the flow behaviour index and the rotation rate along the pipe radius. The velocity profile of the pseudoplastic and dilatant fluids exhibits a gradual increase with the wall distance far away from the pipe wall towards the core region. This increase is more evident in the logarithmic region for all rotation rates.

As illustrated in Figure V.8, the turbulent streamwise velocity seems independent of the flow behaviour index and rotation rate in the near-wall region ; the velocity profiles of the pseudoplastic, Newtonian, and dilatant fluids are consistent with each other in the viscous sub-layer $(0 \leq Y^+ \leq 5)$. Moreover, these profiles collapse very well with the universal law $(U^+ = Y^+)$ in the vicinity of the wall $(0 \leq Y^+ \leq 5)$, denoting a linear axial velocity distribution over the viscous sub-layer.

Beyond $(Y^+ = 10)$, the velocity profiles begin to deviate from others with the wall distance (Y^+) far away from the near-wall region towards the core region. This deviation becomes more obvious in the logarithmic region for all rotation rates. The turbulent mean axial velocity profile of the Newtonian fluid collapses totally with the universal logarithmic law $U^+ = 2.5lnY^+ +$

5.5 in the logarithmic layer. In contrast, the turbulent axial velocity profiles of pseudoplastic and dilatant fluids are somewhat larger than the Newtonian fluid and lie above the universal logarithmic law.

As shown in Figure V.8, the effects of the centrifugal force induced by the swirl driven by the rotating pipe wall on the axial velocity distributions of pseudoplastic and dilatant fluids become more significant with the wall distance outer the buffer region, the profiles of the rotating pipe begin to deviate slightly from those of the stationary pipe, and this trend is more pronounced in the logarithmic region.

When the pipe rotates, the axial velocity profile of the dilatant fluid increases gradually in the logarithmic region, which is more noticeable as the rotation rate (N) increases. It can be said that the centrifugal force induced by the swirl-driven results in a marked increase in the axial velocity profile in the core region, where which is known as the laminarisation phenomenon.

It should be mentioned that the centrifugal force induced by the swirl driven by the rotating pipe wall induces a pronounced decrease in the shear rate profile of the pseudoplastic and dilatant fluids along the pipe radius, resulting in a marked increase in the axial velocity profile in the logarithmic region, this trend is more pronounced as the rotation rate increases.

Figure V.9, presents the streamwise velocity profiles along the pipe radius of the pseudoplastic and dilatant fluids, in addition to the analytical velocity profile in the laminar regime for both fluids scaled by the analytical laminar centreline velocity $(U_{CL} = (3n+1)\,U_b/\,(n+1))$, against the distance from the wall, normalised by the pipe radius (R). It is evident that the predicted velocity profiles of the pseudoplastic and dilatant fluids are similar to the laminar profile, where a parabolic shape characterises these profiles ; the velocity profile in the laminar flow is pronouncedly higher than the others in the turbulent flow.

As shown in Figure V.9, the effects of the flow behaviour index on the mean axial velocity distributions are more marked along the pipe radius. The profiles of pseudoplastic lie above those of Newtonian and dilatant fluids over the three regions (sub-layer, buffer, and logarithmic), especially in the core region. The decreased flow behaviour index results in a pronounced increase in the axial velocity profile for all rotation rates. It should be noted that the increased flow behaviour index induces an apparent decrease in the shear rate along the pipe radius, resulting in a marked increase in the mean axial velocity profile in the core region.

As discussed above, the effects of the rotating pipe wall on the velocity distribution are pronounced along the pipe radius ; the velocity profiles of the rotating pipe are located above

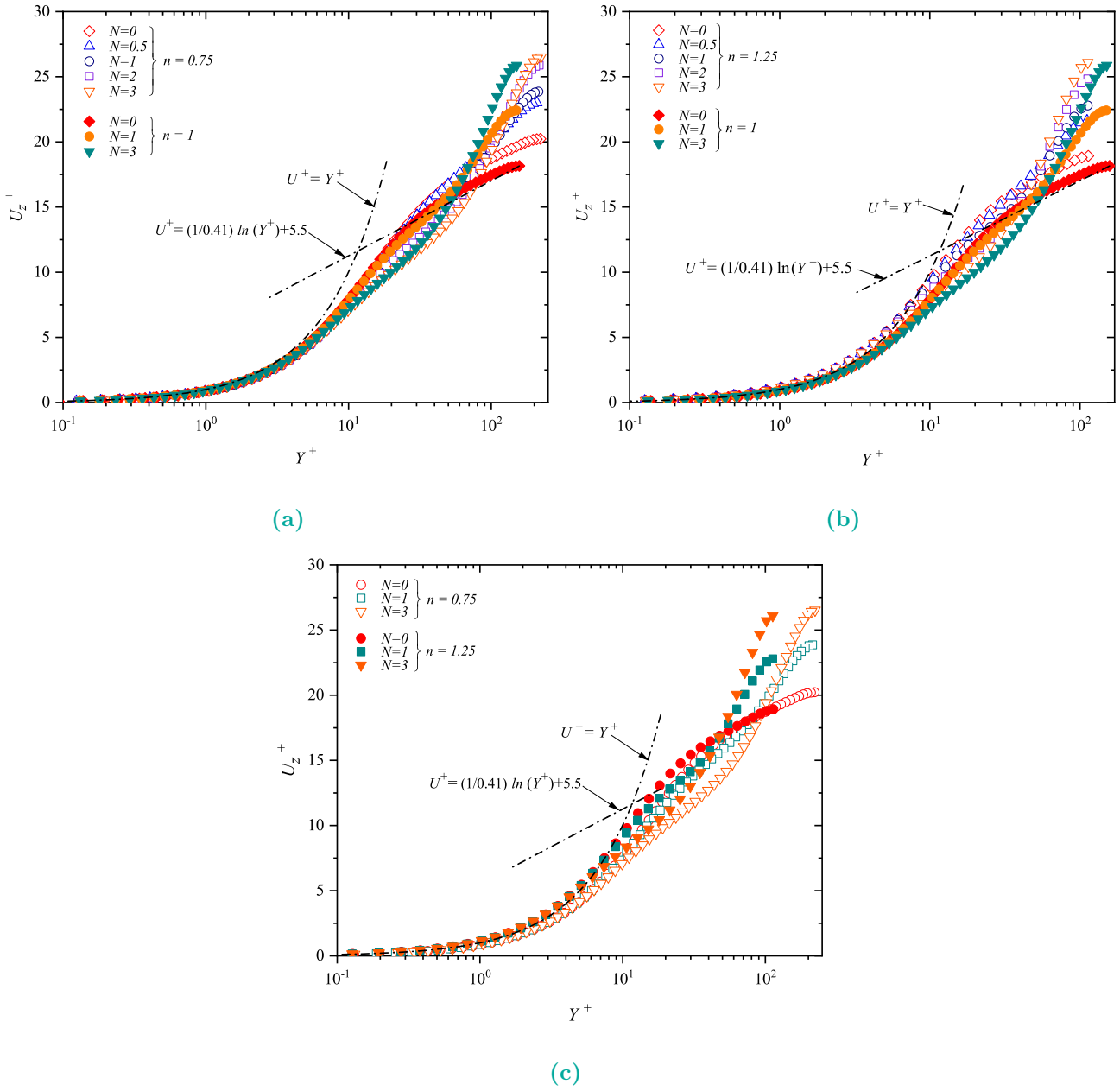

Figure V.8 – Turbulent axial velocity profiles.

the corresponding stationary pipe, where this trend is more pronounced as the rotating pipe wall rotates. The axial velocity profile of the pseudoplastic and dilatant fluids increases significantly as the pipe wall rotates for all flow behaviour indices. The increased axial velocity is due to the decrease in the shear rate caused by the swirl driven by the rotating pipe wall.

Figure V.10, shows the tangential velocity distribution scaled by the rotation velocity at the wall, against the distance from the wall, normalised by the pipe radius (R). It can be seen from

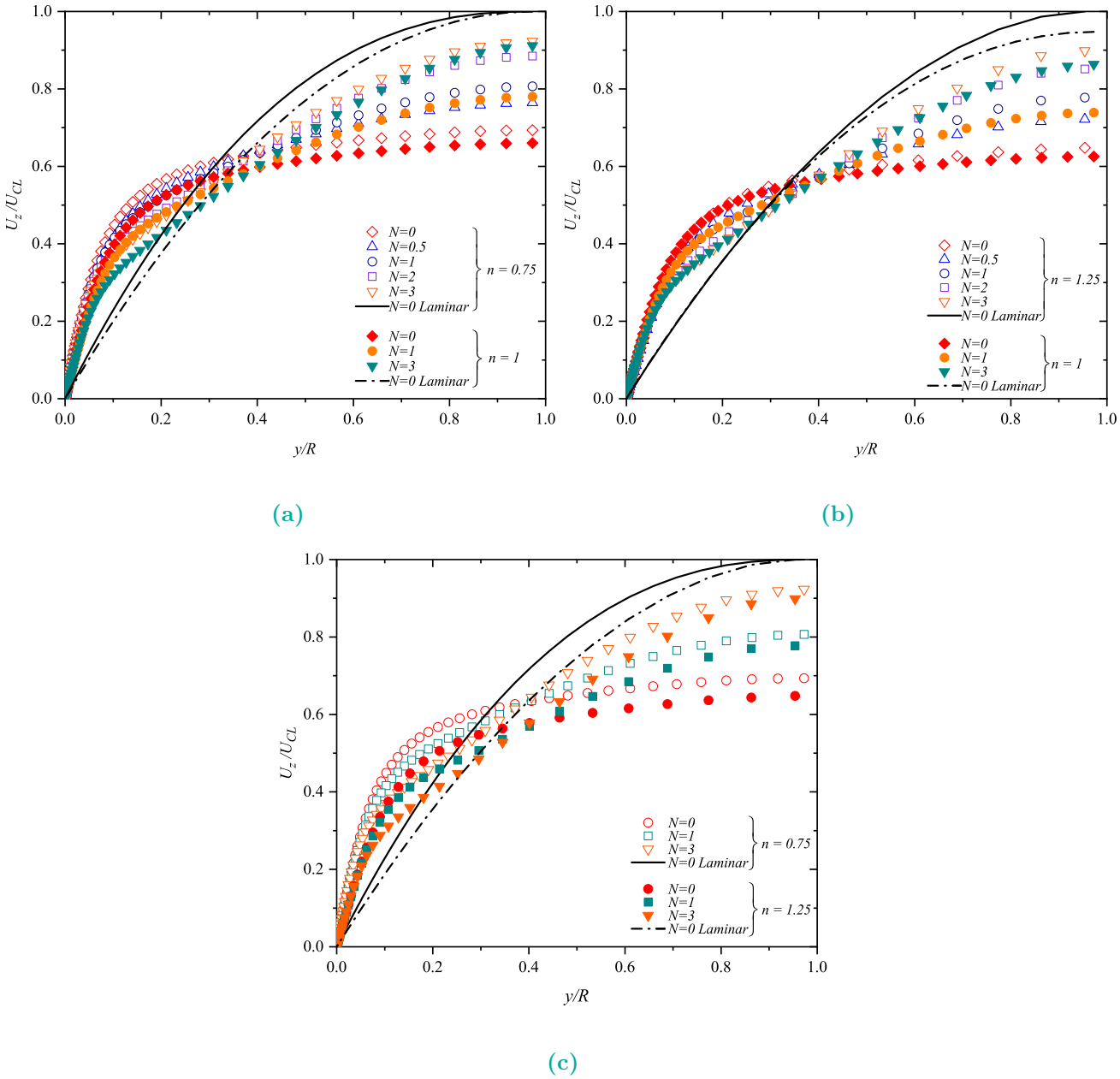

Figure V.9 – Mean axial velocity profiles.

Figure V.10, that the mean circumferential velocity has a parabolic profile shape, the profiles of the pseudoplastic and Newtonian fluids are almost identical along the radial coordinate for all rotation rates, with a little discrepancy between them. As shown in Figure V.10, the tangential velocity distributions of the dilatant fluid seem more affected by the rotation rate along the pipe radius, and these profiles appear more curved as the rotation rate increases. It can be said that the centrifugal force induced by the swirl driven by the rotating pipe wall leads to a curve of the tangential velocity distributions along the pipe radius. This trend is more noticeable as

the rotation rate increases.

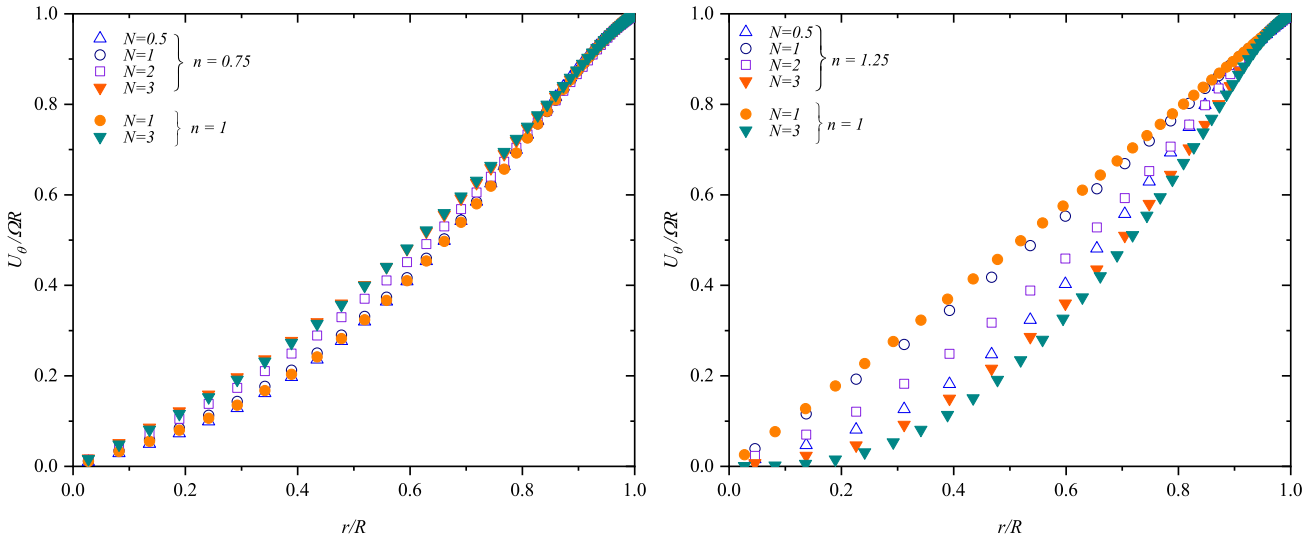

(a) (b)

Figure V.10 – Tangential velocity profiles.

V.4.1.3 Turbulent intensity

The present subsection aims to explore the effects of the centrifugal force induced by the swirl driven by the rotating pipe wall in addition to the effects of the flow behaviour index of pseudoplastic and dilatant fluids on the turbulence feature and the generation and transport mechanism of turbulence intensities of the velocity fluctuation from the wall vicinity towards the core region. The current subsection analyses and discusses the effects of the rotation rate and flow behaviour index on the main turbulence statistics, such as turbulence intensities of the velocity fluctuations, turbulent kinetic energy and the Reynolds stress.

The Figure V.11, Figure V.12 and Figure V.13 depict the root mean square (RMS) distribution of the axial, radial and tangential velocity fluctuations, respectively, of pseudoplastic $(n = 0.75)$ and dilatant $(n = 1.25)$ fluids, scaled by the friction velocity $U_\tau = \sqrt{\tau_w/\rho}$ along the pipe radius (R), versus the distance from the wall in wall units (Y^+) at a simulation's Reynolds number of and over a rotation rate range of $(0 \leq N \leq 3)$.

As shown in Figure V.11, the distribution of turbulence intensities of the axial velocity fluctuations of the pseudoplastic and dilatant fluids exhibit a similar trend along the pipe radius ; a clear oscillating trend is observed over the radial direction of these profiles. The RMS profiles

increase gradually with the wall distance (Y^+) far from the pipe wall towards the core region for all considered cases. This means the axial velocity fluctuations are generated in the near wall region and transported from the viscous sub-layer towards the core region. At a large wall distance, RMS of the axial velocity fluctuations of the pseudoplastic and dilatant fluids begin to drop rapidly and fall off to lower values in the buffer $(5 \leq Y^+ \leq 30)$ region for all rotation rates ; this means that the axial fluctuations become to vanish gradually in this flow region.

It can be said here that the RMS of the axial component is almost independent of the flow behaviour index and the rotation rate (N) in the near-wall region. The RMS of the axial components of the pseudoplastic and dilatant fluids are almost identical in the vicinity of the wall ; they are consistent up to approximately $(Y^+ = 7)$ for all rotation rates. As seen in Figure V.11, the turbulence intensities profiles of the axial velocity fluctuations begin to deviate from each other further away from the wall towards the core region ; this deviation becomes more distinct with the distance from the wall (Y^+), especially in the buffer region. The RMS profiles of the pseudoplastic fluid are larger than the dilatant one along the pipe radius for all rotation rates. It can be said that the decreased flow behaviour index results in a pronounced decrease in the RMS of the axial velocity fluctuations beyond the buffer region $(5 \leq Y^+ \leq 30)$.

On the other hand, the RMS profiles of the axial velocity fluctuations seem strongly affected by the rotation rate along the pipe radius for the pseudoplastic and dilatant fluids. The RMS profiles of the rotating pipe are consistent with those of the stationary pipe near the wall region. These profiles differ significantly from each other with the wall distance towards the buffer region for the pseudoplastic and dilatant fluids, where the RMS profiles of the stationary lie above those of the rotating pipe and where this discrepancy becomes more distinct with increasing rotation rate (N). Looking at Figure V.11, it is apparent that the RMS of the axial velocity profiles flattens in the peak region with an increase in the rotation rate. Moreover, the predicted peak location shifts away from the wall when the pipe rotates. For pseudoplastic and dilatant fluids, the rotation rate induces a decrease in peak value, with the peak value in the stationary pipe being somewhat higher than the corresponding peak value in the rotating case. It can be said that the swirl caused by the rotating pipe wall results in a noticeable attenuation in the generation and transport mechanism of turbulence intensities of the axial velocity fluctuation from the wall vicinity towards the core region for the pseudoplastic and dilatant fluids.

The (RMS) profiles of the dilatant fluids begin to deviate from each other out of the viscous sub-layer, where this deviation becomes more distinct far away from the wall towards the core

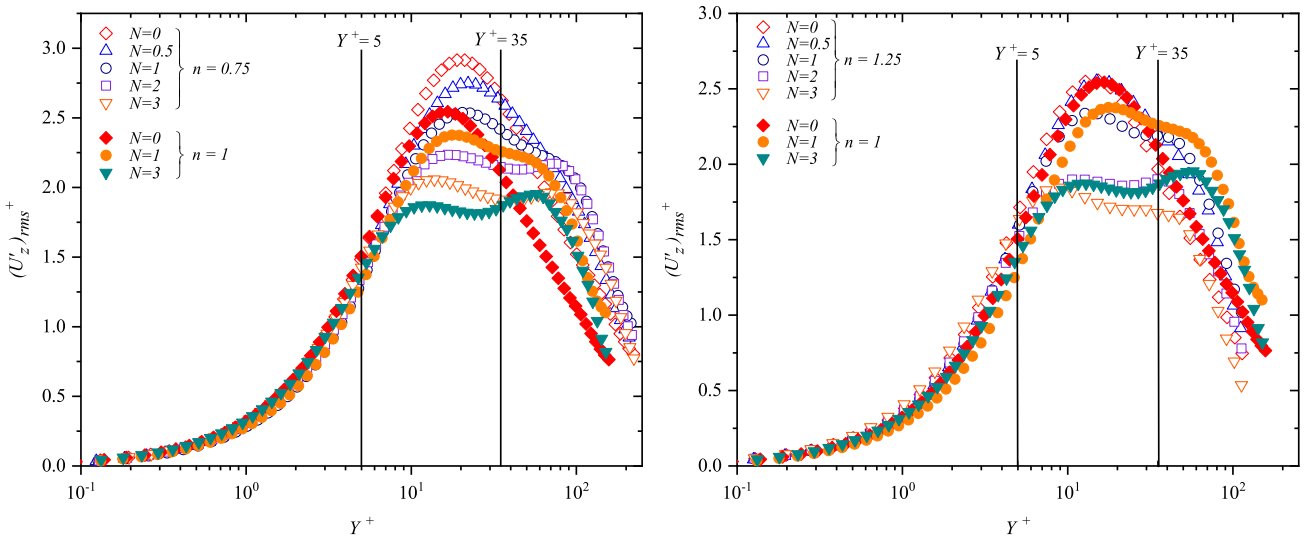

(a) **(b)**

Figure V.11 – Root mean square of the fluctuating axial velocity profiles.

region with wall distance, where beyond $(Y^+ = 2)$ the profiles of the radial turbulence intensities exhibit a significant increase further away from the wall towards the core region. This increase is related to the increase in the turbulence generation of the axial velocity fluctuations in the buffer region for all rotation rates, as shown in Figure V.12. At the large wall distance; the radial turbulence intensity profiles decrease noticeably after reaching their peak values in the logarithmic region $(30 \leq Y^+ \leq 200)$, for all rotation rates. As a result of vanish of axial velocity fluctuations. As shown in Figure V.12 that the radial turbulence intensities profiles of the stationary pipe lie down those of the rotating pipe wall along the pipe radius for both fluids, where this trend is evident as the pipe wall rotates, where the increased rotating pipe wall results in an enhancement in the radial turbulence intensities. It can be said that the increased rotation rate induces a pronounced enhancement in the transport mechanism of turbulence intensities of the radial velocity fluctuation from the vicinity of the wall towards the core flow region.

As shown in Figure V.13, the turbulence intensities of the tangential velocity profiles exhibit the same trend along the pipe radius for the pseudoplastic and dilatant fluids for all rotation rates. The *RMS* profiles of the tangential fluctuations are almost neglected in the near-wall region; this is ascribed to the molecular shear stress being the dominant force compared to the turbulent one in the near-wall region. The tangential turbulence intensities seem more affected

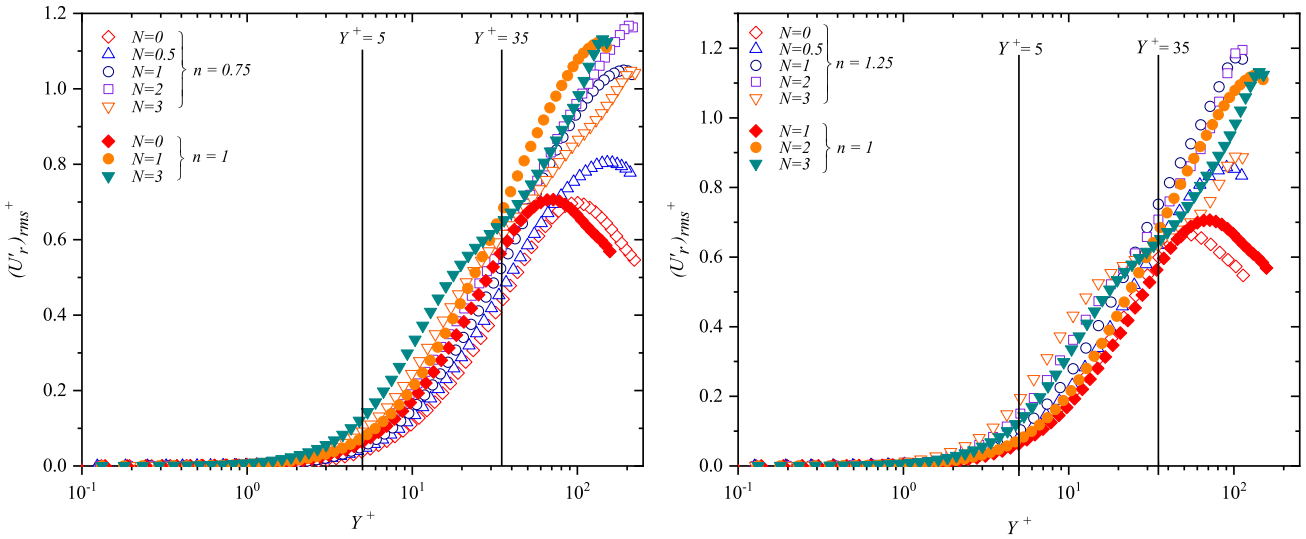

(a) **(b)**

Figure V.12 – Root mean square of the fluctuating radial velocity profiles.

by rotation rate, where these profiles differ significantly beyond the near-wall region. As shown in Figure V.13, these profiles gradually increase and deviate from each other away from the near-wall region with the distance from the wall (Y^+). They drop rapidly and fall to lower values beyond approximately $(Y^+ = 20)$, for all rotation rates.

As shown in Figure V.13, the turbulence intensities of the tangential velocity fluctuations of the rotating pipe are significantly higher than the RMS profile of the stationary pipe along the pipe radius, especially in the buffer region ; this trend is evident as the pipe wall rotates. It can be said that the increased rotating pipe wall results in a pronounced enhancement in the turbulence intensities of the tangential velocity fluctuations along the radial coordinates. This means that the increased rotation rate induces a pronounced enhancement in the transport mechanism of turbulence intensities from the axial velocity fluctuation to the tangential ones of the pseudoplastic and dilatant fluids.

V.4.1.4 Turbulent kinetic energy

Figure V.14 presents the turbulent kinetic energy of the pseudoplastic $(n = 0.75)$, Newtonian $(n = 1)$, and dilatant $(n = 1.25)$ fluids along the pipe radius (R), versus the distance from the wall in wall units (Y^+), at a simulation's Reynolds number of 4500 and over a rotation rate range of $(0 \leq N \leq 3)$.

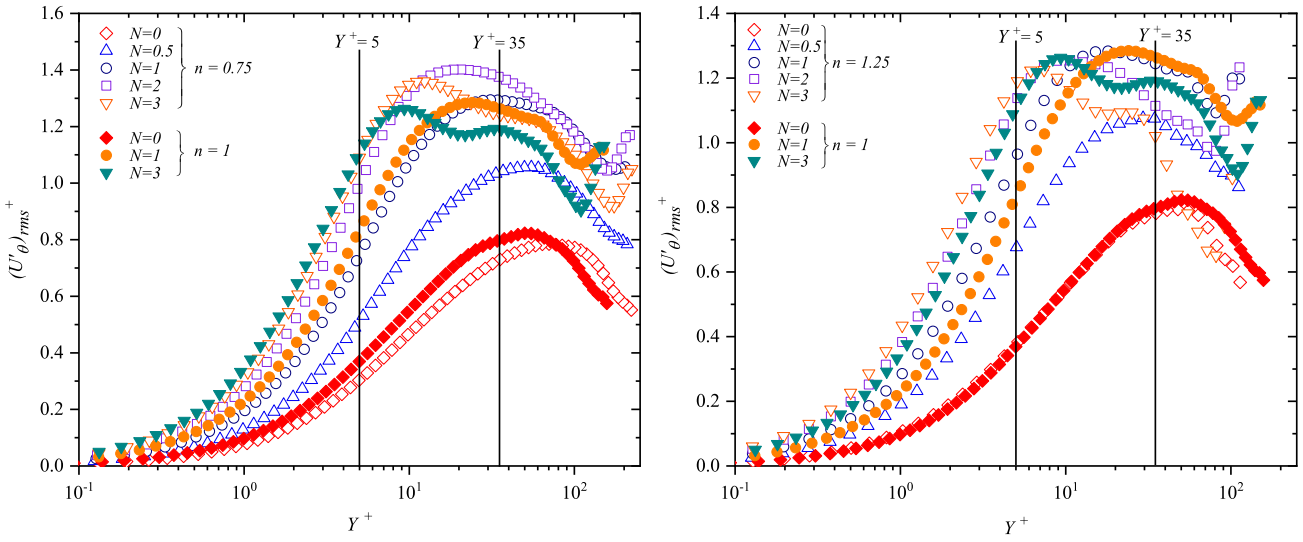

(a) (b)

Figure V.13 – Root mean square of the fluctuating tangential velocity profiles.

As shown in Figure V.14, the kinetic energy of turbulent fluctuations exhibits almost the same trend of the turbulence intensities of the axial velocity fluctuations Figure V.11. The kinetic energy is almost independent of the rotation rate and equal to zero in the near-wall region, there is no difference between the kinetic energy profiles, and they are consistent with each other in the viscous sub-layer for all rotation rates. This trend is attributed to the absence of axial, radial and tangential velocity fluctuations in the vicinity of the pipe wall, where the molecular shear stress is the dominant force in this region.

Far away from the pipe wall, the turbulent kinetic energy gradually increases with the wall distance (Y^+) ; this increase is due to the enhancement in the turbulence generation turbulence intensities of the axial, radial and tangential velocity fluctuations in the buffer region. The turbulent kinetic energy profiles reach their peak values, beyond approximately $(Y^+ = 20)$, these profiles drop and fall off rapidly to the zero value in the core region ; this reduction is due to the vanish of the axial, radial and tangential turbulence intensities in the buffer region for all rotation rates.

It is evident that the turbulent kinetic energy profiles of the stationary pipe are higher than those of the rotating pipe over the pipe radius, especially in the buffer region ; this trend is pronounced as the rotation rate increases. It can be said that the increased rotation rota results in a pronounced suppression in the turbulent kinetic energy along the pipe radius ; this

attenuation is due to the reduction in the generation of the turbulence intensities of the axial velocity fluctuations far away from the wall with increasing rotation rate. It is interesting to note that the swirl driven by the rotating pipe wall results in an apparent attenuation in the generation and transport mechanism of turbulence intensities of the axial velocity fluctuation from the wall vicinity towards the core region for both flow behaviour indices Figure V.11, resulting a pronounced attenuation in the turbulent kinetic energy further away from the pipe wall with the wall distance. It should be noted that this trend is more pronounced as the rotation rate increases Figure V.14.

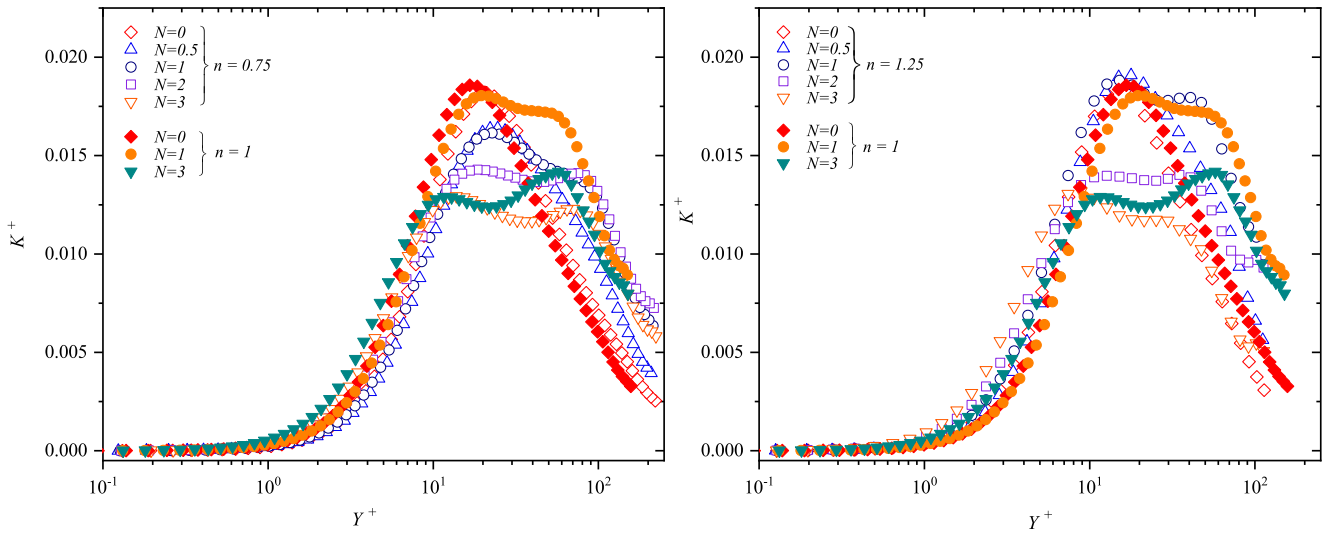

(a) **(b)**

Figure V.14 – Turbulent kinetic energy profiles.

V.4.1.5 Reynolds tensor

Figure V.15 depicts the turbulent Reynolds shear stress distributions of the axial and radial velocity fluctuations along the pipe radius scaled by the friction velocity $U_\tau = \sqrt{\tau_w/\rho}$, against the distance from the wall in wall units (Y^+), for pseudoplastic $(n = 0.75)$, Newtonian $(n = 1)$, and dilatant $(n = 1.25)$ fluids at simulation's Reynolds number of 4500 and rotation rate range of $(0 \leq N \leq 3)$.

It can be seen from Figure V.15 that the Reynolds shear stress profiles of the axial and radial velocity fluctuations are identical and equal to zero in the viscous sub-layer; this is due to the absence of the velocity fluctuations near-wall region. Beyond the buffer layer, the Reynolds stress profiles differ from each other and increase sharply to reach their peak value in the buffer

region ; this increase is related to the generation of the axial fluctuations further away from the wall Figure V.11, as well as to the ameliorate the turbulence transport of the radial velocity fluctuation from the axial velocity fluctuation in the buffer region Figure V.11. As shown in Figure V.15, the Reynolds shear stress profiles of the axial and radial velocity fluctuations fall off rapidly to zero value in the core region, where this is attributed to vanish of the axial and radial velocity fluctuation in this region Figure V.11 and Figure V.12. It is worth noting that when the flow behaviour index decreases the Reynolds shear stress of the axial, radial velocity fluctuations reduce considerably along the pipe radius.

As seen in Figure V.15, the axial and radial velocity fluctuations' Reynolds shear stress profiles seem affected by the pipe wall's rotation rate for dilatant along the pipe radius. These profiles decrease with an increase in wall pipe rotation due to the stabilising effect of the centrifugal force. It is worth noting that this attenuation in the Reynolds stress profile is also due to the reduction in the generation and transport mechanism of turbulence intensities of the axial velocity fluctuation from the wall vicinity towards the core region for both flow behaviour indices, caused by swirl driven by the rotating pipe wall Figure V.11.

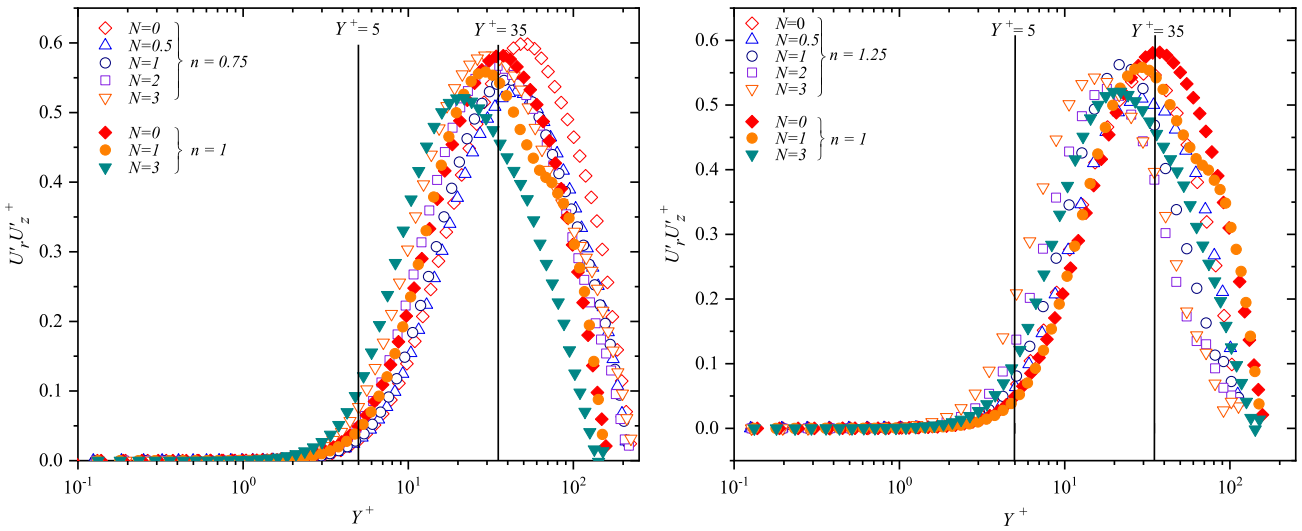

(a) **(b)**

Figure V.15 – Reynolds stress $\langle U'_r U'_z \rangle$ profiles.

Figure V.16 depicts the turbulent Reynolds shear stress distributions along the pipe radius scaled by the friction velocity $U_\tau = \sqrt{\tau_w/\rho}$, against the distance from the wall in wall units

(Y^+) for pseudoplastic $(n = 0.75)$, Newtonian $(n = 1)$, and dilatant $(n = 1.25)$ fluids at simulation's Reynolds number of 4500 and rotation rate range of $(0 \leq N \leq 3)$.

Figure V.16 presents the turbulent Reynolds shear stress of the tangential and radial velocity fluctuations along the pipe. The predicted profiles of Reynolds shear stress are equal to zero value along the viscous sub-layer $(0 \leq Y^+ \leq 5)$ in the near-wall region; the molecular shear stress is the dominant force. At larger distances from the wall, turbulent Reynolds shear stress profiles deviate significantly from each other and exhibit a gradual enhancement with the wall distance far away from the wall for all rotation rates; this enhancement is due to the generation of the axial velocity fluctuations Figure V.11 in the wall vicinity in addition to the transport of these fluctuations to the radial and tangential components from the wall towards the core region.

As observed in Figure Figure V.16, the Reynolds stress of the tangential and radial velocity fluctuations of the stationary pipe are lower than those of the rotating pipe along the pipe radius for both fluids, where the profiles of the rotating pipe lie above that of the stationary this trend is more pronounced as the rotation rate increases. It is worth noting that the increased rotation rate induces in a marked enhancement in the profile of the Reynolds stress of the tangential and radial velocity fluctuations, where as shown in Figure V.12 and Figure V.13, the increased rotating pipe wall results in an enhancement in the radial and tangential turbulence intensities, this increase results in a pronounced enhancement in the transport mechanism of turbulence intensities of the radial and tangential velocity fluctuation from the vicinity of the wall towards the core flow region. It is clearly apparent in Figure V.16 that beyond the logarithmic region $(30 \leq Y^+ \leq 200)$, the Reynolds stress of the tangential and radial velocity fluctuations profiles drop and fall off to zero values in the core region. It can also be seen that the turbulent Reynolds shear stress profile decreases after reaching the peak value in the core region; these profiles fall off rapidly to zero value in the core region, which indicates the fluctuations of the tangential and radial velocity vanish in this region.

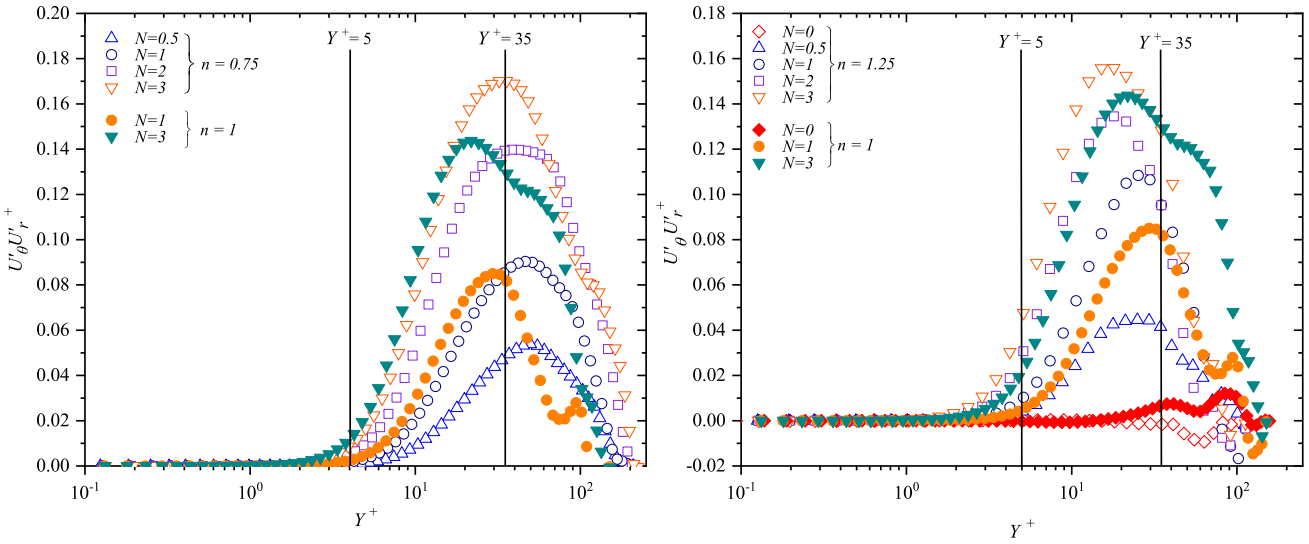

(a) (b)

Figure V.16 – Reynolds stress $\langle U'_\theta U'_r \rangle$ profiles.

V.4.2 LES of Forced Convection of Dilatant Fluid

To validate the present study, the predicted results of the current study have been compared reasonably well with those of *LES* of Abdi et al. (2019) [50] available in the literature Figure V.17 and Figure V.18 in order to ascertain the reliability and accuracy of the *LES* code laboratory.

Figure V.17 compares the dimensionless temperature distributions of the shear-thinning and the Newtonian fluids through a rotating pipe wall with the *LES* of Abdi et al. (2019) [50] at the simulation Reynolds number of 4000 . As shown in Figure V.17, dimensionless temperature profiles are in excellent agreement with those of Abdi et al. (2019) [50] ; these profiles are consistent very well with the compared results over the pipe radius.

Figure V.18 reasonably compares the predicted root mean square (*RMS*) distributions of the temperature fluctuations of the shear-thinning ($n = 0.75$) and Newtonian fluids along the pipe radius for the rotating pipe. These profiles have been compared reasonably with the *LES* of Abdi et al. (2019) [50] at the simulation Reynolds number of 4000. As shown in Figure V.18, the predicted *RMS* of the temperature fluctuations of the shear-thinning turns out to be in excellent agreement with those of Abdi et al. (2019) [50] along the pipe radius.

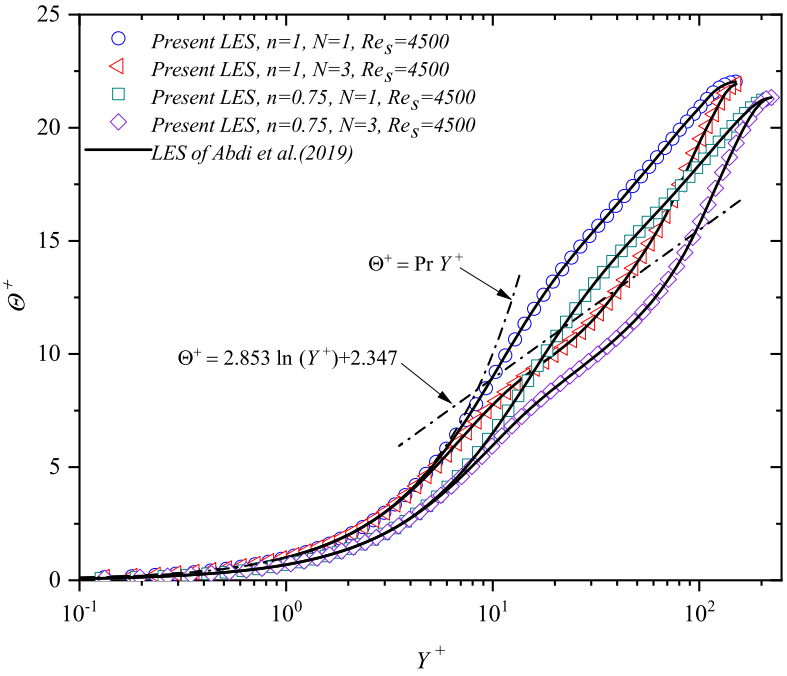

Figure V.17 – Validation of temperature distributions.

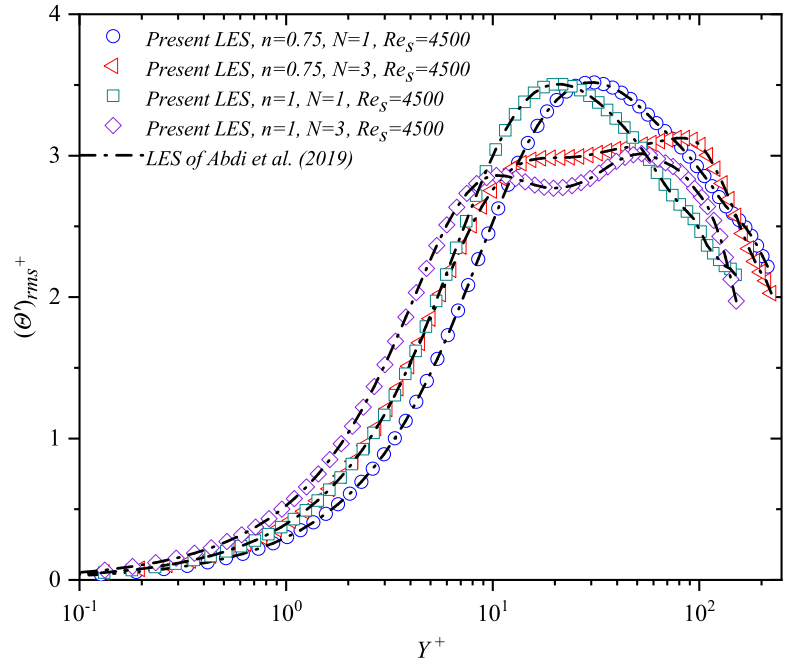

Figure V.18 – Validation of root mean square of temperature.

V.4.2.1 Temperature profiles

The present subsection aims to shed light on the influence of the centrifugal force induced by the swirl driven by the rotating pipe wall on the fluid temperature by analysing and discussing the effect of the rotation rates.

Figure V.19 illustrates the dimensionless temperature distributions (Θ^+) of the dilatant $(n = 1.25)$ fluid through an axially rotating heated pipe over various rotation rates $(0 \leq N \leq 3)$ at a simulation Reynolds (Re_s) number and Prandtl number (Pr) equal to 4500 and 1 respectively. It should be noted that the dimensionless temperature is the mean temperature $(\Theta = (\langle T_W(z) \rangle - T(\theta, r, z, t)) / T_{ref})$ scaled by the friction temperature (T_τ).

Apparently, there is a clear trend of increase in the temperature profile $(\Theta')^+$ along the radial direction, where the temperature profile $(\Theta')^+$ begins to enhance gradually wall with the wall distance far away from the pipe wall, for all cases. It can be seen from Figure V.19 that the profiles of the dilatant fluid begin to deviate slightly from each other with the wall distance (Y^+) further away from the pipe wall towards the core region. As for the flow behaviour index effect, Abdi et al. (2019) [50] argued that the decreased flow behaviour index results in a pronounced reduction in the temperature profile over the radial coordinate. In other words, the decreased flow behaviour index induces an obvious attenuation in the heat transfer between the pipe wall and the fluid, this trend is more pronounced as the flow behaviour index is decreased.

On the other hand, Figure V.19 provides a minor dependence of temperature profile on the rotation rate (N) over the near-wall region; indeed, the temperature profiles of dilatant fluid are very close to each other for all rotation rates over the conductive sub-layer $(0 \leq Y^+ \leq 5)$. The centrifugal force induced by the rotating pipe wall considerably affects the temperature distributions for the dilatant fluid with the wall distance further away from the pipe wall as the rotation rate (N) increases. As shown in Figure V.19, the temperature profiles begin to deviate significantly from each other beyond approximately $Y^+ \approx 10$; the temperature profiles of the stationary pipe lie above those of the rotating pipe ones. It can be seen that the increased rotation rate induces a noticeable reduction in the temperature profile along the radial coordinates, especially in the logarithmic region for the dilatant fluid. One could infer that the temperature attenuation results from the lower fluid apparent viscosity further away from the pipe wall, where the fluid becomes less rigid in the core region when the rotation rate increases. It is interesting to note that this reduction is due to the smaller residence time of the fluid particles away from the pipe wall. The fluid flow is more accelerated due to the centrifugal force induced by the pipe wall rotation; this trend is more pronounced as the rotation rate increases.

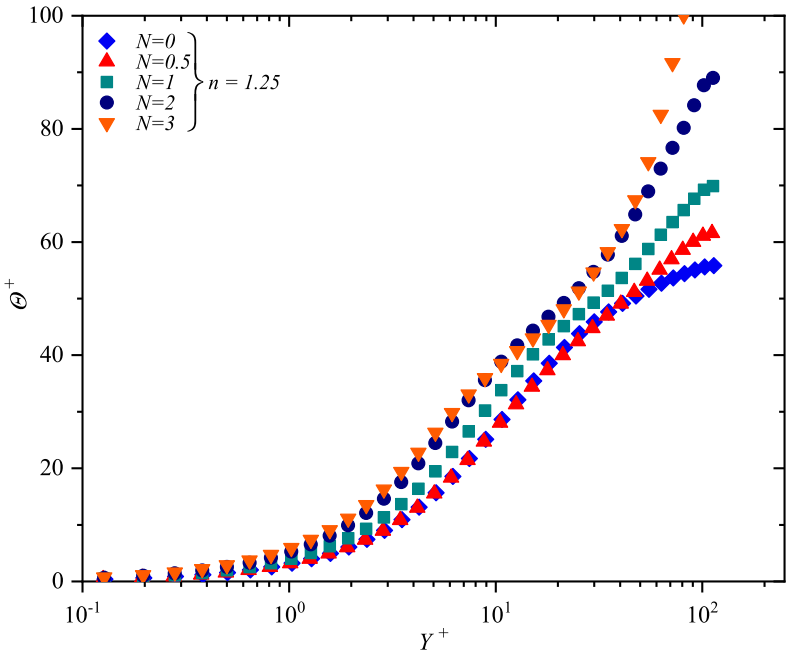

Figure V.19 – Temperature profiles.

V.4.2.2 Root mean square of temperature and turbulent heat flux

The purpose of the current subsection is to explore the effects of the centrifugal force induced by the swirl driven by the rotating pipe wall in addition to the effects of the rotation rate on the turbulence intensities of the temperature fluctuations from the wall vicinity towards the core region.

It can be seen from Figure V.20 that the effect of the flow behaviour index (n) is almost limited in the vicinity of the pipe wall where the RMS profiles have the same tendency along the pipe radius; these profiles coincide with each other near the wall region $(Y^+ < 1)$. At around $(Y^+ = 1)$, these profiles differ considerably in the buffer and logarithmic regions with the distance from the pipe wall (Y^+). As shown in Figure V.20, the RMS profiles are enhanced gradually further away from the wall towards the core region with the distance from the wall (Y^+); these profiles drop rapidly after reaching the peak locations, indicating that the temperature fluctuations are generated in the vicinity of the wall and propagated progressively towards the core region. It should be noted that beyond $(Y^+ \approx 7)$, the temperature fluctuations intensities ultimately fall off to lower values, indicating that the temperature fluctuations vanish gradually far away from the wall for all rotation rates.

As for the flow behaviour index effect, Abdi et al. (2019) [50] argued that the decreased flow behaviour index induces an apparent attenuation of the generation and the transport mechanism of the temperature fluctuations between the flow regions due to the difference in the apparent fluid viscosity. As shown in Figure V.20 reveals that the RMS profiles of the temperature fluctuations become higher further away from the wall with increasing rotation rate (N). It can be noted that the centrifugal force induced by the rotating pipe wall results in a noticeable amelioration of the temperature fluctuations out of the viscous sub-layer $(0 \leq Y^{+} \leq 5)$. In other words, the increased rotation rate results in a pronounced increase in the turbulent transfer mechanism of the temperature fluctuations between the flow layers ; this deviation is related to the smaller relative apparent fluid viscosity towards the pipe centre with an increasing rotation rate.

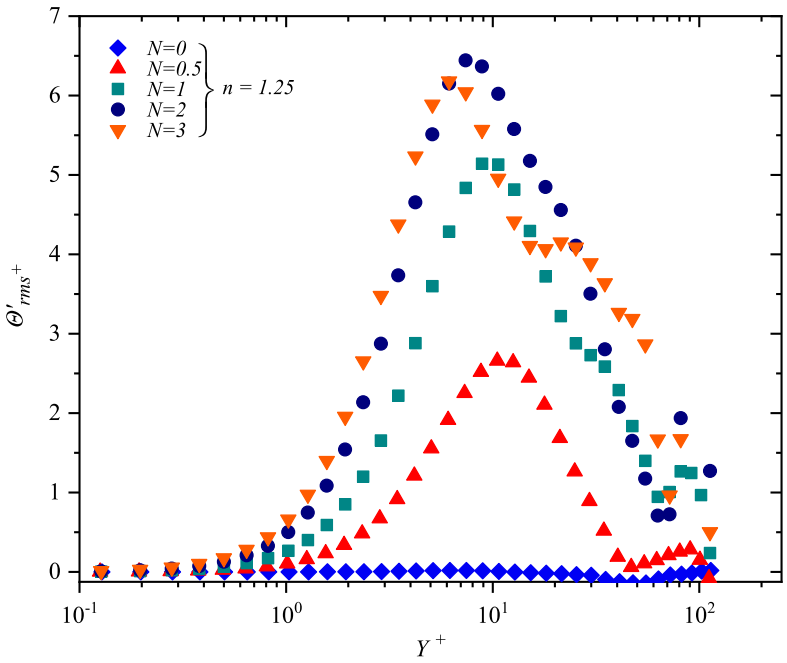

Figure V.20 – Root mean square of temperature profiles.

Figure V.21 and Figure V.22 show the turbulent axial and radial heat fluxes distributions of the dilatant $(n = 1.25)$ fluid against the distance from the wall (Y^{+}) in wall units, over a various rotation rate $(0 \leq N \leq 3)$ at $\mathrm{Re}_s = 4500$ and $\mathrm{Pr}_s = 1$.

It can be noted that the axial, radial and tangential heat fluxes profiles of the dilatant fluid are identical and equal to the zero in the viscous sub-layer $(Y^{+} < 1)$, which indicates that the absence of the fluctuation in this region, where the molecular shear stress is the is the dominant

force in this region. In turn, these heat flux profiles enhance gradually further away from the wall towards the central region before reaching the peak location. The heat flux components start to damp progressively in the logarithmic region. The axial, radial and tangential velocity fluctuations and the temperature fluctuations begin to decrease gradually until they fall off to zero value in the core region. It can be said that the axial velocity and temperature fluctuations generated at the vicinity of the wall exactly in the viscous sub-layer and propagated to the logarithmic layer, these fluctuations begin to vanish in the remaining region after reaching their maximum values.

As shown in Figure V.21, the turbulent axial heat flux profiles of the rotating pipe lie obviously down those of the stationary pipe for both fluids ; the turbulent axial heat flux profiles decrease and become more flattened beyond the buffer region as the rotation rate increases for dilatant fluid. Indeed, the increased rotation rate induces a noticeable reduction in the turbulent axial heat flux, especially in the logarithmic region ; this trend is more pronounced as the pipe wall rotates. It can be said that this reduction is related to the considerable suppression of both axial velocity and temperature fluctuations further away from the wall with increasing the rotation rate. It can be said here that the swirl driven by the rotating pipe wall results in a pronounced attenuation in the generation and transport mechanism of turbulence intensities of the axial velocity and temperature fluctuation from the wall vicinity towards the core region for the dilatant fluids ; this trend is more pronounced as the rotation rate is increased.

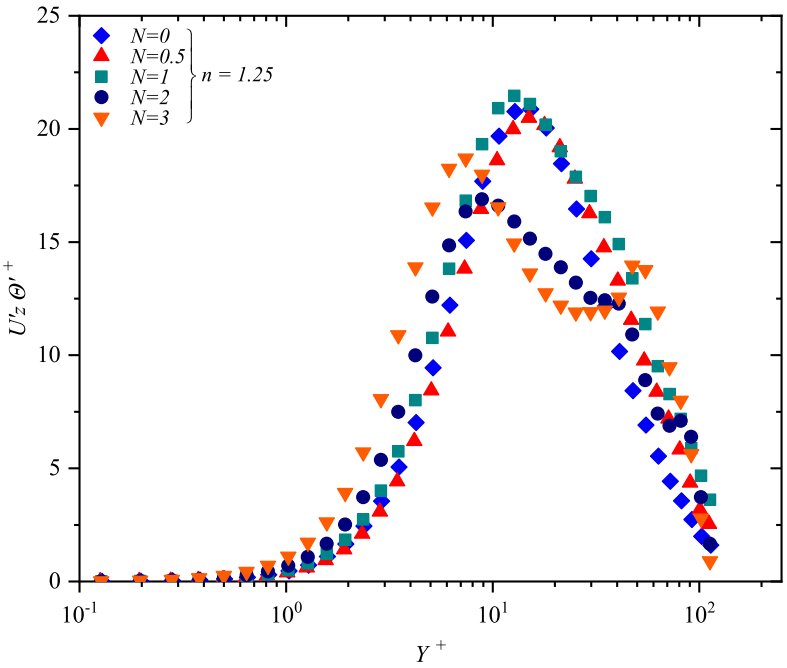

Figure V.21 – Axial turbulent heat flux profiles.

As shown in Figure V.22, the radial heat flux profiles of the dilatant fluid are almost identical in the vicinity of the wall, indicating that the rotation rate's effects in this region are limited. On the contrary, away from the wall toward the core region of the pipe, the predicted profiles begin to deviate remarkably from each other with increasing (N) ; the rotation rate (N) affects the heat flux beyond this region, indicating that the effect of the rotation becomes to be critical towards the core region with the wall distance. The radial heat flux profiles of the rotating pipe exhibit larger values in the logarithmic region ; the stationary profiles lie down those of the rotating pipe for dilatant fluid, where this trend is more pronounced as the rotation rate increases.

It can be said that the increased rotation rate results in a marked enhancement in the radial velocity fluctuations, consequently, in the radial heat flux for dilatant fluid. In other words, the swirl driven by the rotating pipe wall results in a pronounced enhancement in the generation and transport of radial velocity fluctuations ; consequently, in the radial heat flux profiles for dilatant fluid, this trend is more pronounced as the rotation rate is increased.

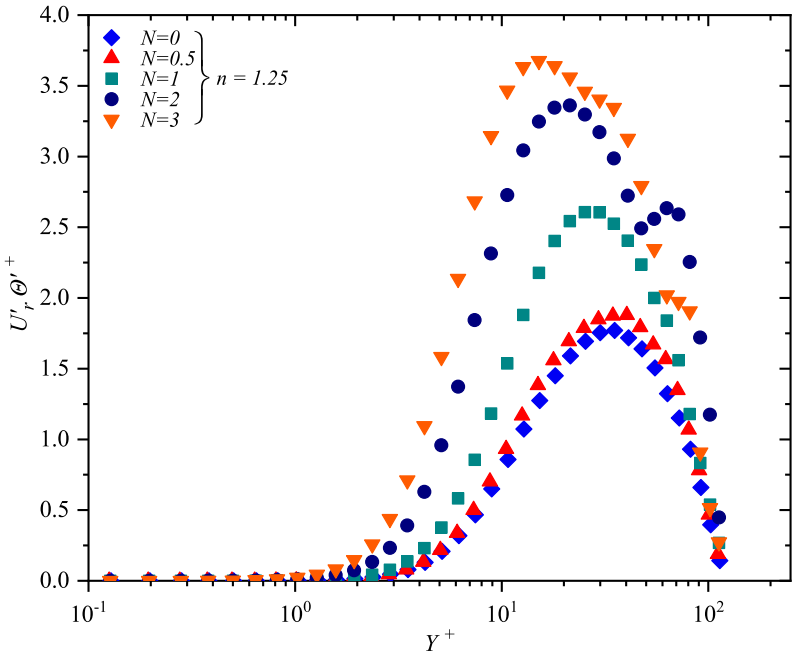

Figure V.22 – Radial turbulent heat flux profiles.

V.5 Conclusion

A critical examination of the effects of the centrifugal force induced by the swirl driven by the rotating pipe wall on rheological, hydrodynamic, and thermal quantities, as well as turbulence characteristics, especially near the wall, was the goal of the present study to shed further light on the laminarisation phenomenon of power-law fluids. The present study was also intended to provide detailed information on mean and turbulence statistics in the vicinity of walls and the hydrodynamic and rheological behaviour of power-law fluids.

The present investigation study assessed to ascertain the accuracy and reliability of the laboratory code predicted findings and to examine the large eddy simulation approach with the extended Smagorinsky effectiveness for predicting the turbulent flow of this kind of fluids. In addition to knowing to what extent the extended Smagorinsky model can characterise the scale's motions, especially in the wall vicinity.

The present investigations were devoted numerically to a large eddy simulation (LES) with an extended Smagorinsky model of the fully developed turbulent pipe flow of pseudoplastic $(n = 0.75)$ and dilatant $(n = 1.25)$ fluids through a heated axially rotating pipe, over a rotation rate range of $(0 \leq N \leq 3)$, at a simulation Reynolds number of and a simulation Prandtl number of . With an adequate grid resolution of 65^3 gridpoints in r, θ and z direction, respectively, and a domain length of $20R$ in the streamwise direction. Uniform heat flux (q_w) was imposed on the wall as a thermal boundary condition.

The mathematical model was implemented in the laboratory code ; the computational procedure is based on the finite difference scheme, second-order accurate in space and time. The time-advancement employs a fractional-step method. A third-order Runge-Kutta explicit scheme and a Crank-Nicholson implicit scheme were used to evaluate the convective and diffusive terms, respectively.

The major conclusions of this research will be summarised :

- The pseudoplastic fluids behaved more like solids when approaching the pipe centre as the shear rate increased beyond the sub-layer region. On the contrary, the decreased shear rate far away from the vicinity of the wall induces a marked decrease in the apparent viscosity of the dilatant fluid with the wall distance towards the logarithmic region.

- The streamwise velocity profiles of the pseudoplastic and dilatant were affected strongly by the centrifugal force induced by the swirl driven by the rotating pipe wall ; the increased rotation rate resulted in a pronounced decrease in the shear rate profile of the pseudoplastic and dilatant fluids along the pipe radius, resulting in a marked increase in the axial velocity profile in the logarithmic region.

- In pseudoplastic and dilatant fluids, swirl generated by rotating pipe walls attenuated the generation and transport mechanism of turbulence intensities of the velocity fluctuations from the wall vicinity to the core region. This increased rotation rate also induced a pronounced enhancement in the transport mechanism of turbulence intensities from the axial velocity fluctuation to the tangential and radial ones of the pseudoplastic and dilatant fluids. This resulted in a pronounced attenuation in the turbulent kinetic energy further away from the pipe wall with the wall distance. This trend was more pronounced as the rotation rate increased.

GENERAL CONCLUSION

GENERAL CONCLUSION

The present study aimed to shed further light on the laminarisation phenomena of the Ostwald de Waele fluids by critically examining the effects of the centrifugal force induced by the swirl driven by the rotating pipe wall on the rheological quantities (shear rate and the apparent viscosity), the mean flow and thermal quantities such as the streamwise velocity profiles, the tangential velocity distribution and the fluid temperature profiles. In addition to, the flow and thermal statistical turbulence quantities such as the turbulent kinetic energy, root mean square (RMS) of the axial, radial and tangential velocity fluctuations, turbulent Reynolds shear stress, turbulent heat flux.

The present investigation also tended to reveal the effects of the flow behaviour index on the mean flow characteristics to provide an accurate, complete, and detailed description of the flow patterns and rheological behaviour of the Ostwald de Waele fluids along the radial coordinate, especially in the core region, where it is still difficult for experimental methods to get reliable data for certain variables, especially for rheological flows, despite improvements in experimental techniques.That is via analysing the flow behaviour index effects of the Ostwald de Waele fluids on the streamwise velocity distribution along the radial coordinate and the generation and transport mechanism of the velocity fluctuations between the different turbulent layers.

The present investigation aimed to ascertain the accuracy and reliability of the DNS laboratory code predicted results and to evaluate the reliability of the DNS approach to predict the main flow quantities and turbulence statistics of the Ostwald de Waele fluid. On the other hand, the present study objected to ascertaining the accuracy and reliability of the laboratory code predicted findings and examining the LES approach with the extended Smagorinsky effectiveness for predicting the turbulent flow of this kind of fluids. In addition, to know to what

extent the extended Smagorinsky model can characterise the scales motions, especially in the wall vicinity.

The computational procedure was based on a finite difference scheme, second-order accurate in space and time. The time-advancement employs a fractional-step method. A third-order Runge-Kutta explicit scheme and a Crank-Nicholson implicit scheme were used to evaluate the convective and diffusive terms.

The first study investigation has been devoted numerically to a Direct Numerical Simulation (DNS) of a fully developed turbulent flow of pseudoplastic $(n = 0.75)$ and dilatant $(n = 1.2)$ fluids through an isothermal axially rotating pipe over a rotation rate range $(0 \leq N \leq 3)$, where the simulation Reynolds number was assumed to be 5000 with a computational domain length of $20R$ in the streamwise direction. The finite difference scheme has performed the computational procedure, second-order accurate in space and time with a numerical resolution of $(129 \times 129 \times 193)$ gridpoints in axial, radial and circumferential directions, respectively.

The second study investigates numerically a fully developed turbulent flow of forced convection of non-thermo-dependent pseudoplastic and dilatant fluids through a heated axially rotating cylindrical pipe using the LES approach with an extended Smagorinsky model at simulation Reynolds and Prandtl numbers of $\mathrm{Re}_s = 4500$ and $\mathrm{Pr}_s = 1$, respectively. The numerical resolution was chosen to be 65^3 gridpoints in axial, radial and circumferential directions, respectively, with a domain length of $20R$ in the axial direction. A uniform heat flux (q_w) was imposed on the wall as a thermal boundary condition. The present predicted results were to be in excellent agreement with the experimental and DNS data available in the literature.

The major conclusions of this research will be summarised as follow :

- The predicted results of the DNS and LES approaches suggested that the flow pattern and hydrodynamic characteristics of the Ostwald de Waele fluids were significantly affected by the centrifugal force induced by the swirl driven by the rotating pipe wall. The rotation rate of the pipe wall strongly influenced the DNS and LES streamwise velocity profiles of the pseudoplastic and dilatant fluids over the viscous sub-layer, buffer and logarithmic regions. The radially growing centrifugal force induced by the swirl driven by the rotating pipe wall caused a supplemented force to the inertia force, which resulted

in a noticeable reduction in the apparent fluid viscosity and a noticeable increase in the streamwise velocity of pseudoplastic and dilatant in the core region.

- The predicted results of the *DNS* approach indicated that the increased rotation rate resulted in a noticeable enhancement in the generation and transport mechanism of turbulence intensities of the axial velocity fluctuation from the wall vicinity towards the core region. This increased rotation rate also enhances the transport mechanism of turbulence intensities of the radial velocity fluctuation from the axial velocity fluctuation. On the contrary, in *LES* results, the swirl driven by the rotating pipe wall resulted in an apparent attenuation in the generation and transport mechanism of turbulence intensities of the axial velocity fluctuation from the wall vicinity towards the core region, resulting in a pronounced attenuation in the turbulent kinetic energy further away from the pipe wall with the wall distance. It should be noted that the discrepancy between *DNS* and *LES* approaches may be due to the difference in the Reynolds number value and the numerical solution procedure.

- The predicted results of the *DNS* and *LES* approaches suggested that the increased rotation rate induced a pronounced enhancement in the transport mechanism of turbulence intensities of the radial velocity fluctuation from the axial velocity fluctuation resulting in the radial heat flux for dilatant fluid.

- The increased rotation rate induced a noticeable reduction in the temperature profile along the radial coordinates, especially in the logarithmic region for the dilatant fluid.

Further research could also be conducted to determine the rotation rate's effect on another non-Newtonian fluids model. As for the thermal behaviour, it would be interesting to assess the thermo-dependence influence of the pseudoplastic and dilatant properties on the turbulence statistics and rheological behaviour.

STATISTICAL ANALYSIS OF TURBULENCE

A

Turbulent flows exhibit random structures with variable behaviour in time and space, which makes it difficult to study turbulence exhaustively. These behaviours can be described from theories based on one-point statistics. The first statistics that provide information about turbulent flow are the moments related to the random variable. These are the mean or first-order moment (the time average and the ensemble mean) and the high-order moments that provide more information about the vortex structures [72].

A.1 Variability

It is interested in systems whose statistical variables depend only on space. These systems are said to be statistically stationary. For any random variable $b(x_i, t)$, the Reynolds decomposition for this variable is the sum of its mean value and a fluctuating quantity as shown in the following equation [72] :

$$b(x_i, t) = \overline{b(x_i)} + b'(x_i, t) \tag{A.1}$$

With $\overline{b(x_i)}$ the mean value of the variable $b(x_i, t)$ and $b'(x_i, t)$ its fluctuation. The variance σ^2 or standard deviation σ for this variable is given by :

$$\sigma^2 = \overline{b'^2(x_i, t)} \tag{A.2}$$

In turbulence, the standard deviation represents the RMS (root mean square). It provides information on the dispersion of the values of the variable around the mean. It describes the evolution of the intensity of the turbulence [72].

A.2 Skewness coefficient

The Skewness coefficient or third order moment is calculated by :

$$S(b') = \frac{\overline{b'^4}}{\left[\overline{b'^2}(x_i)^{3/2}\right]} = \frac{b'^3}{\sigma^3} \tag{A.3}$$

It provides information on the relative magnitude of positive and negative fluctuations in relation to the mean value. Positive fluctuations are predominant if $S(b')$ is positive. If it is negative, negative fluctuations predominate [72].

A.3 Flatness coefficient

The flatness coefficient or fourth order moment is calculated by :

$$F(b') = \frac{\overline{b'^4}}{\left[\overline{b'^2}(x_i)\right]^2} = \frac{b'^4}{\sigma^4} \tag{A.4}$$

It provides information on the relative flatness of the distribution of fluctuations compared to the normal distribution [72].

A.4 Correlation coefficient

If it considers two variables $a'(x_i, t)$ and $b'(x_i, t)$, the correlation coefficient is defined by :

$$R_{a'b'} = \frac{\overline{a'b'(x_i)}}{\left[\overline{a'^2}(x_i)\overline{b'^2}(x_i)\right]^{1/2}} \tag{A.5}$$

This coefficient varies between (-1) and $(+1)$. It is $(+1)$ if the two variables are perfectly correlated, (-1) if they are perfectly uncorrelated and 0 if there is no statistical link between the two variables for normal laws [72].

BIBLIOGRAPHY

BIBLIOGRAPHY

[1] Thomas Mezger. *The rheology handbook : for users of rotational and oscillatory rheometers*. European Coatings, 2020.

[2] Fridtjov Irgens. *Rheology and non-newtonian fluids*, volume 1. Springer, 2014.

[3] Howard A Barnes, John Fletcher Hutton, and Kenneth Walters. *An introduction to rheology*, volume 3. Elsevier, 1989.

[4] Raj P Chhabra and John Francis Richardson. *Non-Newtonian flow and applied rheology : engineering applications*. Butterworth-Heinemann, 2011.

[5] NJ Alderman. Non-newtonian fluids : guide to classification and characteristics. *London : ESDU*, 1997.

[6] Taha Sochi. Non-newtonian flow in porous media. *Polymer*, 51(22) :5007–5023, 2010.

[7] Aroon Shenoy. *Heat Transfer to Non-Newtonian Fluids : Fundamentals and Analytical Expressions*. John Wiley & Sons, 2018.

[8] Eden Reid and RheoSense Senior Sales. Viscosity of battery mixtures.

[9] Paolo Orlandi and M Fatica. Direct simulations of turbulent flow in a pipe rotating about its axis. *Journal of Fluid Mechanics*, 343 :43–72, 1997.

[10] JMJ Den Toonder and FTM Nieuwstadt. Reynolds number effects in a turbulent pipe flow for low to moderate re. *Physics of Fluids*, 9(11) :3398–3409, 1997.

[11] Murray Rudman and Hugh M Blackburn. Large eddy simulation of turbulent pipe flow. In *Second International Conference o CFD in the Minerals and Process Industries CSIRO, Melbourne, Australia*, pages 6–8, 1999.

[12] Marzio Piller. Direct numerical simulation of turbulent forced convection in a pipe. *International journal for numerical methods in fluids*, 49(6) :583–602, 2005.

[13] Mitsukiyo Murakami and Kouji Kikuyama. Turbulent flow in axially rotating pipes. 1980.

[14] Kenji Nishibori, Koji Kikuyama, and Mitsukiyo Murakami. Laminarization of turbulent flow in the inlet region of an axially rotating pipe : fluids engineering. *JSME International journal*, 30 (260) :255–262, 1987.

[15] Shuichiro Hirai, Toshimi Takagi, and Masaharu Matsumoto. Predictions of the laminarization phenomena in an axially rotating pipe flow. 1988.

[16] Jack GM Eggels, Friedemann Unger, MH Weiss, Jerry Westerweel, Ronald J Adrian, Rainer Friedrich, and Frans TM Nieuwstadt. Fully developed turbulent pipe flow : a comparison between direct numerical simulation and experiment. *Journal of Fluid Mechanics*, 268 :175–210, 1994.

[17] Shigeki Imao, Motoyuki Itoh, and Takeyoshi Harada. Turbulent characteristics of the flow in an axially rotating pipe. *International journal of heat and fluid flow*, 17(5) :444–451, 1996.

[18] Zhiyin Yang. Large eddy simulation of fully developed turbulent flow in a rotating pipe. *International journal for numerical methods in fluids*, 33(5) :681–694, 2000.

[19] AA Feiz, M Ould-Rouis, and Guy Lauriat. Large eddy simulation of turbulent flow in a rotating pipe. *International journal of heat and fluid flow*, 24(3) :412–420, 2003.

[20] G Reich and H Beer. Fluid flow and heat transfer in an axially rotating pipe—i. effect of rotation on turbulent pipe flow. *International Journal of heat and mass transfer*, 32(3) :551–562, 1989.

[21] Gerhard Reich, Bernhard Weigand, and Hans Beer. Fluid flow and heat transfer in an axially rotating pipe—ii. effect of rotation on laminar pipe flow. *International Journal of heat and mass transfer*, 32(3) :563–574, 1989.

[22] JN Cannon and WM Kays. Heat transfer to a fluid flowing inside a pipe rotating about its longitudinal axis. 1969.

[23] MR Malin and BA Younis. The prediction of turbulent transport in an axially rotating pipe. *International communications in heat and mass transfer*, 24(1) :89–98, 1997.

[24] Brian Edward Launder, G Jr Reece, and W Rodi. Progress in the development of a reynolds-stress turbulence closure. *Journal of fluid mechanics*, 68(3) :537–566, 1975.

[25] MR Malin and BA Younis. Calculation of turbulent buoyant plumes with a reynolds stress and heat flux transport closure. *International journal of heat and mass transfer*, 33(10) :2247–2264, 1990.

[26] MM Gibson and BA Younis. Calculation of swirling jets with a reynolds stress closure. *The Physics of fluids*, 29(1) :38–48, 1986.

[27] Charles G Speziale, Sutanu Sarkar, and Thomas B Gatski. Modelling the pressure–strain correlation of turbulence : an invariant dynamical systems approach. *Journal of fluid mechanics*, 227 : 245–272, 1991.

[28] Shin-ichi Satake and Tomoaki Kunugi. Direct numerical simulation of turbulent heat transfer in an axially rotating pipe flow : Reynolds shear stress and scalar flux budgets. *International Journal of Numerical Methods for Heat & Fluid Flow*, 2002.

[29] L Redjem-Saad, Meryem Ould-Rouiss, and Guy Lauriat. Direct numerical simulation of turbulent heat transfer in pipe flows : Effect of prandtl number. *International Journal of Heat and Fluid Flow*, 28(5) :847–861, 2007.

[30] Meryem Ould-Rouiss, A Dries, and A Mazouz. Numerical predictions of turbulent heat transfer for air flow in rotating pipe. *International journal of heat and fluid flow*, 31(4) :507–517, 2010.

[31] M Bousbai, Meryem Ould-Rouiss, A Mazouz, and A Mataoui. Turbulent heat transfer characteristics of water flow in a rotating pipe. *Heat and Mass Transfer*, 49(4) :469–484, 2013.

[32] AB Metzner and JC Reed. Flow of non-newtonian fluids—correlation of the laminar, transition, and turbulent-flow regions. *Aiche journal*, 1(4) :434–440, 1955.

[33] AB Metzner. Non-newtonian fluid flow. relationships between recent pressure-drop correlations. *Industrial & Engineering Chemistry*, 49(9) :1429–1432, 1957.

[34] DW Dodge and AB Metzner. Turbulent flow of non-newtonian systems. *AIChE journal*, 5(2) : 189–204, 1959.

[35] FT Pinho and JH Whitelaw. Flow of non-newtonian fluids in a pipe. *Journal of non-newtonian fluid mechanics*, 34(2) :129–144, 1990.

[36] MR Malin. Turbulent pipe flow of power-law fluids. *International communications in heat and mass transfer*, 24(7) :977–988, 1997.

[37] Murray Rudman, Hugh Maurice Blackburn, Lachlan JW Graham, and L Pullum. Turbulent pipe flow of shear-thinning fluids. *Journal of non-newtonian fluid mechanics*, 118(1) :33–48, 2004.

[38] Murray Rudman and Hugh M Blackburn. Direct numerical simulation of turbulent non-newtonian flow using a spectral element method. *Applied mathematical modelling*, 30(11) :1229–1248, 2006.

[39] Takashi Ohta and Masahito Miyashita. Dns and les with an extended smagorinsky model for wall turbulence in non-newtonian viscous fluids. *Journal of Non-Newtonian Fluid Mechanics*, 206 : 29–39, 2014.

[40] Andrey A Gavrilov and Valeriy Ya Rudyak. Reynolds-averaged modeling of turbulent flows of power-law fluids. *Journal of Non-Newtonian Fluid Mechanics*, 227 :45–55, 2016.

[41] AA Gavrilov and V Ya Rudyak. Direct numerical simulation of the turbulent energy balance and the shear stresses in power-law fluid flows in pipes. *Fluid Dynamics*, 52 :363–374, 2017.

[42] J Singh, M Rudman, and HM Blackburn. The influence of shear-dependent rheology on turbulent pipe flow. *Journal of Fluid Mechanics*, 822 :848–879, 2017.

[43] EZ Zheng, M Rudman, J Singh, and SB Kuang. Direct numerical simulation of turbulent non-newtonian flow using openfoam. *Applied Mathematical Modelling*, 72 :50–67, 2019.

[44] Massimo Germano, Ugo Piomelli, Parviz Moin, and William H Cabot. A dynamic subgrid-scale eddy viscosity model. *Physics of Fluids A : Fluid Dynamics*, 3(7) :1760–1765, 1991.

[45] John Kim and Parviz Moin. Application of a fractional-step method to incompressible navier-stokes equations. *Journal of computational physics*, 59(2) :308–323, 1985.

[46] Thomas A Zang. Numerical simulation of the dynamics of turbulent boundary layers : Perspectives of a transition simulator. *Philosophical Transactions of the Royal Society of London. Series A : Physical and Engineering Sciences*, 336(1641) :95–102, 1991.

[47] PS Gnambode, P Orlandi, Meryem Ould-Rouiss, and Xavier Nicolas. Large-eddy simulation of turbulent pipe flow of power-law fluids. *International Journal of Heat and Fluid Flow*, 54 : 196–210, 2015.

[48] V Vidyanidhi and A Sithapathi. Non-newtonian flow in a rotating straight pipe. *Journal of the Physical Society of Japan*, 29(1) :215–219, 1970.

[49] RW Gunn, B Mena, and K Walters. On newtonian and non-newtonian flow in a rotating pipe. *Zeitschrift für angewandte Mathematic and Physic ZAMP*, 25 :591–606, 1974.

[50] Mohamed Abdi, Abdelkader Noureddine, and Meryem Ould-Rouiss. Numerical simulation of turbulent forced convection of a power law fluid flow in an axially rotating pipe. *Journal of the Brazilian Society of Mechanical Sciences and Engineering*, 42(1) :17, 2020.

[51] Mohamed Abdi, Khaled Chaib, Meryem Ould-Rouiss, and Slimane Benferhat. Large eddy simulation of turbulent flow of pseudoplastic and dilatant fluids : rheological and hydrodynamic behaviour. *DESALINATION AND WATER TREATMENT*, 279 :85–89, 2022.

[52] Mohamed Abdi, Meryem Ould-Rouiss, Fatima Zohra Nedjda Bouhenni, and Abdelfettah Menouer. Large eddy simulation of turbulent flow of pseudoplastic and dilatant fluids : turbulence characteristics. *DESALINATION AND WATER TREATMENT*, 279 :109–114, 2022.

[53] Mohamed Abdi, Meryem Ould-Rouiss, Manel Ait Yahia, and Amina Ould-Mohamed. Large eddy simulation investigation of reynolds number effects on rheological behavior of ostwald-de waele fluids. *DESALINATION AND WATER TREATMENT*, 279 :168–172, 2022.

[54] Mohamed Abdi, Meryem Ould-Rouiss, Lalia Abir Bouhenni, Nour Elhouda Beladjine, and Belhouari Abdelkarim Bekhtaoui. Effect of reynolds number on turbulence characteristics of turbulent ostwald-de waele fluids. *DESALINATION AND WATER TREATMENT*, 279 :173–177, 2022.

[55] Mohamed Abdi, Meryem Ould-Rouiss, and Abdelkader Noureddine. Hydrodynamic and rheological characteristics of a pseudoplastic fluid through a rotating cylinder. *Numerical Heat Transfer, Part A : Applications*, pages 1–20, 2023.

[56] Jacobus Gerardus Maria Eggels. Direct and large eddy simulation of turbulent flow in a cylindrical pipe geometry. 1995.

[57] Hendrik Tennekes, John Leask Lumley, Jonh L Lumley, et al. *A first course in turbulence*. MIT press, 1972.

[58] Eugene De Villiers. The potential of large eddy simulation for the modeling of wall bounded flows. *Imperial College of Science, Technology and Medicine*, 2006.

[59] Stephen B Pope and Stephen B Pope. *Turbulent flows*. Cambridge university press, 2000.

[60] Ulka Gaitonde, Y Gong, and FX Tanner. Quality criteria for large eddy simulation. *First Year Transfer Report, School of MACE, University of Manchester*, 2008.

[61] Pierre Sagaut, Marc Terracol, and Sebastien Deck. *Multiscale and multiresolution approaches in turbulence-LES, DES and Hybrid RANS/LES Methods : Applications and Guidelines*. World Scientific, 2013.

[62] Václav Uruba. Turbulence handbook for experimental fluid mechanics professionals. *Skovlunde : Dantec Dynamic*, 2012.

[63] Tor Holan Marstein. Direct numerical simulation of turbulent flow in a channel with transverse ribs. Master's thesis, NTNU, 2015.

[64] Marcel Lesieur. *Turbulence in fluids*, volume 593. Springer, 2008.

[65] Francois Cadieux. *Large eddy simulations of laminar separation bubble.* PhD thesis, University of Southern California, 2015.

[66] Joseph Smagorinsky. General circulation experiments with the primitive equations : I. the basic experiment. *Monthly weather review*, 91(3) :99–164, 1963.

[67] Javad Taghinia et al. Sub-grid scale modeling in large eddy simulation with variable eddy-viscosity coefficient. 2015.

[68] Kursad Melih Guleren. *Large-eddy simulation of wall-bounded flows subjected to curvature and rotation.* PhD thesis, University of Manchester, 2007.

[69] Florian R Menter. Best practice : scale-resolving simulations in ansys cfd. *ANSYS Germany GmbH*, 1, 2012.

[70] Kemal Hanjalić and Brian Launder. *Modelling turbulence in engineering and the environment : second-moment routes to closure.* Cambridge university press, 2011.

[71] Günther Grötzbach. Spatial resolution requirements for direct numerical simulation of the rayleigh-bénard convection. *Journal of computational physics*, 49(2) :241–264, 1983.

[72] Mohamed Abdi. *Simulation numérique à grande échelle (LES) de l'écoulement turbulent pleinement développé d'un fluide non newtonien dans une conduite cylindrique en rotation.* PhD thesis, University of Science and Technology of Oran Mohamed Boudiaf, 2020.

[73] Sourou Gnambode. *Simulation des grandes échelles des transferts thermo-convectifs dans les écoulements turbulents d'un fluide non-newtonien en conduite cylindrique.* PhD thesis, Paris Est, 2015.